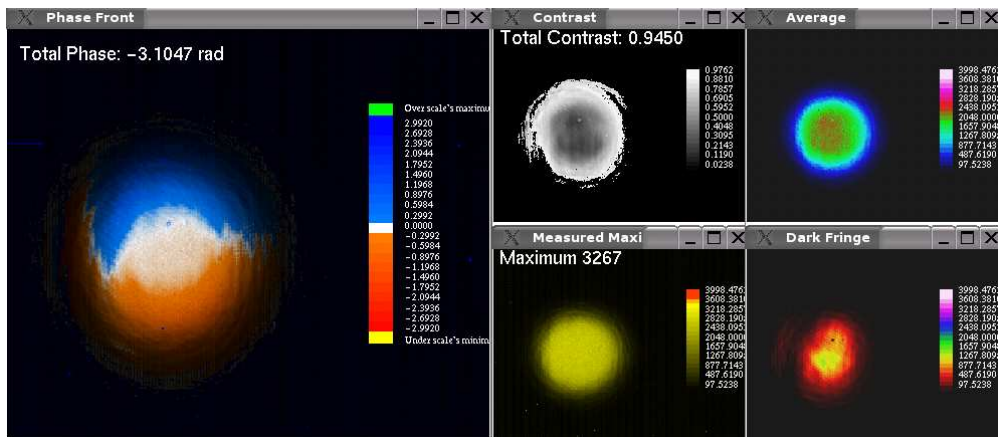


Real-Time Spatially Resolving Phasemeter for LISA Pathfinder



Master of Science Degree Thesis
by
Felipe Guzmán Cervantes

Max Planck Institute for Gravitational Physics
Albert Einstein Institute, Hanover

First Examiner: Prof. Dr. Karsten Danzmann (Albert Einstein Institute)
Second Examiner: Dr. habil. Rainer Reuter (C.v.O. University of Oldenburg)
Supervisor: Dr. Gerhard Heinzl (Albert Einstein Institute)

Submitted to the Carl von Ossietzky University of Oldenburg on December 15th 2004

A Dios ...

no hay palabras.

Abstract

LISA Pathfinder is a mission planned by the European Space Agency (ESA) with contributions from the American National Aeronautics and Space Administration (NASA). The main purpose of the LISA Technology Package (LTP) on board LISA Pathfinder is to test the current technology developed for the laser-interferometric gravitational-wave detector in space LISA. A heterodyne interferometer is utilized to measure the distance between two test masses with an accuracy of pm at mHz frequencies. Moreover, the interference pattern has to be monitored by quadrant photodiodes to enable the detection of tilting of the test masses with nrad precision.

Performance tests on interferometer prototypes have shown that phase measurements conducted with quadrant photodiodes are affected by a higher noise level in comparison to results obtained with single-element photodiodes. This could be explained by the combination of beam pointing jitter over the quadrants and an inhomogeneous spatial distribution of the phase. This inhomogeneity is given by the discrepancy between the parameters of the interfering beams, whose phase fronts differ at the recombination. A direct measurement of the spatial distribution of the resulting phase front was impossible until now.

The development of a state-of-the-art measuring apparatus, which allows a real-time measurement and display of the phase front in a heterodyne Mach-Zender interferometer, is presented in this thesis.

This device enables the analysis and direct measurement of the influences of optical components on the phase front.

The information displayed in real-time on the graphical user interface (GUI) developed for this application provides a convenient support for an optimal alignment of the beams. Adjustment of the optical components in the interferometer can thus be conducted on-line to optimize the parameters of the interfering beams in order to achieve a homogenization of the spatial distribution of the phase.

Due to the advantages provided by this instrument, its application will be helpful in the production of the flight model of the optical bench in LISA Pathfinder.

Zusammenfassung

LISA Pathfinder ist ein Weltraumprojekt der europäischen Weltraum Agentur ESA mit Beiträgen der amerikanischen NASA. Das LISA Technologie Demonstration Package (LTP) an Bord von LISA Pathfinder soll die bisher entwickelten Technologien für LISA, den laser-interferometrischen Gravitationswellendetektor im Weltraum, erproben. Das LTP benutzt ein heterodyn-Interferometer, um den Abstand zweier Testmassen mit einer Genauigkeit im Pikometerbereich in einem mHz Frequenzbereich zu messen. Um zusätzlich die Verkippungen der Testmassen (mit nrad-Genauigkeiten) zu beobachten, werden Quadrantenphotodioden für die Abtastung des Interferenzmusters verwendet.

Untersuchungen an Interferometerprototypen zeigten, dass Phasenmessungen, in denen Quadrantendioden verwendet worden sind, stets mehr Rauschen zeigen als bei der Verwendung von single-element Dioden. Eine mögliche Erklärung dafür sind Strahlgefunktuationen auf den Quadranten der Photodiode in Verbindung mit einer räumlich inhomogenen Struktur der Phase. Diese Inhomogenität wird durch den Unterschied zwischen den Parametern der beiden interferierenden Strahlen bestimmt, aufgrund dessen ihre Phasenfronten bei der Rekombination abweichen. Es war bisher nicht möglich, die räumliche Struktur dieser resultierenden Phasenfront direkt zu vermessen.

In dieser Arbeit wird eine neue Messapparatur vorgestellt, die dazu fähig ist, die aus der Interferenz zweier Laserstrahlen resultierende Phasenfront an einem Heterodyn-Mach-Zender Interferometer in Echtzeit zu vermessen und darzustellen.

Dadurch wird es möglich, die Auswirkung verschiedener optischer Komponenten auf die Phasenfront direkt zu vermessen und genauer zu untersuchen. Ausserdem bietet die Echtzeitdarstellung der Messergebnisse auf einer graphischen Benutzeroberfläche eine direkte Kontrolle für die optimale Ausrichtung der Strahlen. Dadurch wird z.B. eine online Justage der optischen Komponenten zur Homogenisierung der räumlichen Struktur der resultierenden Phasenfront ermöglicht.

Diese Messapparatur wird daher ein wichtiges Hilfsmittel bei der Herstellung des Flugmodells der optischen Bank für LISA Pathfinder sein.

Resumen

LISA Pathfinder es un proyecto desarrollado por la Agencia Espacial Europea (ESA) con contribuciones de la agencia estadounidense NASA. El Paquete Tecnológico para LISA (LTP), a bordo de LISA Pathfinder, tiene como objetivo principal poner a prueba las tecnologías desarrolladas para el detector espacial de ondas gravitacionales LISA, que no pueden ser examinadas en tierra. En esta misión se utiliza un interferómetro heterodino para medir fluctuaciones en la distancia entre dos masas de prueba con alta precisión (picómetros) a frecuencias en el rango de milihertzios. Para detectar inclinaciones y rotaciones que pudiesen presentar las masas de prueba con una precisión de nanoradianes, el patrón de interferencia es muestreado por fotodiodos de cuadrante.

Investigaciones llevadas a cabo en prototipos del interferómetro mostraron un mayor nivel de ruido al medir la fase con fotodiodos de cuadrante en comparación con los resultados obtenidos por fotodiodos simples. El deterioro de la sensibilidad alcanzada con los diodos de cuadrante puede ser explicado mediante una combinación de fluctuaciones de la posición de los rayos junto con una distribución espacialmente inhomogénea de la fase. Dicha inhomogeneidad se debe a la diferencia entre los frentes de fase de los rayos, cuyos parámetros son distintos. Hasta el momento no era posible medir directamente la estructura del frente de fase resultante.

Esta tesis de grado presenta el desarrollo de un instrumento capaz de medir la estructura espacial del frente de fase en un interferómetro heterodino de topología Mach-Zender y mostrarla en tiempo real.

La interfaz gráfica desarrollada para esta aplicación ofrece la información necesaria para un alineamiento adecuado del interferómetro.

De este modo es posible medir y analizar la influencia de diversos componentes ópticos, lo que permite el ajuste requerido para una homogenización de la distribución espacial del frente de fase.

Las ventajas que ofrece este dispositivo lo convierten en un herramienta muy eficaz que será utilizada en la construcción del interferómetro a bordo de LISA Pathfinder.

Contents

Abstract	iii
Zusammenfassung	v
Resumen	vii
Contents	viii
List of Figures	xi
1 Introduction	1
1.1 LISA	2
1.2 LISA Pathfinder	3
2 Interferometer on board LISA Pathfinder	5
2.1 Requirements on the Interferometry	5
2.2 Interferometer Configuration	6
2.2.1 Frequency shift by using Acousto-Optic Modulators	7
2.2.2 Interference and Optical Heterodyne Detection	9
2.2.3 Contrast and Interference Pattern	12
2.3 LISA Pathfinder Interferometer Setup	13
2.3.1 Modulation Bench	14
2.3.2 Optical Bench	16
2.4 Electronic System	19
2.4.1 Driver for the Acousto-Optic Modulators	19
2.4.2 Phase-Locked Loop (PLL)	19
2.4.3 Real-Time Digital Phasemeter	20
2.5 Motivation	22
3 Phase Estimation Method	25
3.1 Theoretical Approach	25
3.1.1 Miscalibrations	28
3.2 Application of the Algorithms	29
3.3 Measurement Outlook	33
4 Experimental Approach	35
4.1 Requirements	35
4.2 Spatially Resolving Photodetectors	35
4.2.1 Silicon Charge-Coupled Device (CCD) Camera	35

4.2.2	Silicon Complementary Metal Oxide Semiconductor (CMOS) Camera	38
4.2.3	Indium-Gallium-Arsenide (InGaAs) CCD Camera	40
4.3	Measurement Procedure	41
5	Phase Front Measurement	45
5.1	Phase Front Measurement with the WinCamD	45
5.1.1	Experimental Setup	45
5.1.2	Results	49
5.2	Phase Front Measurement with the XEVA USB	53
5.2.1	Experimental Setup	53
5.2.2	Graphical User Interface	55
6	Results	63
6.1	Alignment Procedure	63
6.2	Misaligned Interferometer	65
6.3	Different Beam Parameters	67
6.4	Engineering Model of the LTP Interferometer	68
6.5	Homogeneous Phase Front	69
A	Frequency Analysis of a Bandpass Filter	71
A.1	Block Algebra	71
A.1.1	Cascade Blocks	71
A.1.2	Parallel Blocks	72
A.1.3	Feedback	72
A.1.4	Displacement of Bifurcation Points	73
A.1.5	Displacement of Summation Points	73
A.2	Bandpass Filter	73
B	Features programmed for the GUI	81
B.1	Functional Features	81
B.2	Display Features	81
C	Code Developed for the FPGA	83
	Bibliography	91
	Acknowledgment	93
	Verwendete Hilfsmittel	95
	Selbstständigkeitserklärung	97

List of Figures

1.1	Heliocentric orbit of the spacecrafts constituting LISA	2
1.2	CAD model of the LISA Technology Package on board LISA Pathfinder.	4
1.3	Force and displacement noise budgets for LISA and LISA Pathfinder	4
2.1	Measurement of the distance between the test masses	5
2.2	Requirements on the accuracy of the LTP interferometer	6
2.3	Heterodyne Mach-Zender Interferometer	7
2.4	Diffraction of a light beam by acoustic waves in an acousto-optic modulator	8
2.5	Amplitudes of the light fields at the beamsplitter	9
2.6	Recombination of the light fields at a beamsplitter in a Mach-Zender Interferometer	10
2.7	Phase difference between 2 heterodyne signals	12
2.8	Heterodyne signal measured by a photodetector	13
2.9	Schematic of the modules conforming the LPF interferometry system	13
2.10	Schematic of the Modulation Bench on LPF	14
2.11	Space-qualified NPRO-laser developed by TESAT	15
2.12	Prototype for a space qualifiable modulation bench developed by Contraves	15
2.13	Opto-CAD model of the reference interferometer on the optical bench of the LTP	16
2.14	Opto-CAD model of the frequency interferometer on the optical bench	16
2.15	Opto-CAD model of the X1 interferometer on the optical bench .	17
2.16	Opto-CAD model of the X1-X2 interferometer on the optical bench	17
2.17	Engineering Model of the LPF Optical Bench built by the Rutherford Appelton Laboratory and EADS Astrium	18
2.18	Block-diagram of the AOM-Drivers	19
2.19	Block-diagram of the PLL	20
2.20	Block diagram of the data acquisition system	21
2.21	Graphical User Interface of the phasemeter	21
2.22	Noise level measured on a bonded prototype for the optical bench	22
2.23	Single-element photodiodes and quadrant photodiodes	23
2.24	Overlapped wave fronts of interfering beams whose parameters are different. Inhomogeneous phase front	23

2.25	Phase front measured by using a pin hole over a single-element photodiode	24
3.1	Representation of the sampling procedure by a phase shift of $\frac{\pi}{2}$ starting at a bright fringe	30
4.1	Diagram of the functional procedure of a CCD camera	37
4.2	Quantum Efficiency for a typical CCD photodetector	37
4.3	Diagram of a pixel of a CMOS imaging sensor	38
4.4	Diagram of the functional procedure of a CMOS camera	39
4.5	Quantum Efficiency for the Micron MT9M413 CMOS photodetector distributed with the pco.1200hs camera from PCO Imaging	39
4.6	Quantum Efficiency for the InGaAs CCD photodetector FPA distributed by XenICs	40
4.7	Electrical signal produced by a photodiode exposed to the interference beam	41
4.8	Topology used for the electronic circuit of the band-pass filter	42
4.9	Block diagram of the electronics for digitizing the heterodyne signal	43
4.10	Interferometer configuration for the measurement of the phase front with a spatially resolving photodetector	43
5.1	Frame captured by the WinCamD under the effects of blooming	45
5.2	Diagram of the signals processed and sent by the FPGA	46
5.3	Flow diagram of the program loaded onto the FPGA for the phase front measurement with the WinCamD	47
5.4	Illustration of the experimental setup used for the measurement of the phase front with the WinCamD	48
5.5	Phase front measured by the silicon CCD camera WinCamD at a well-adjusted interferometer	49
5.6	Phase front measured with a pin hole covering a single element photodiode using the phasemeter presented in section 2.4.3	50
5.7	Setup for the measurement of the phase front with a lens of 500mm focal length on one arm of the interferometer using the WinCamD camera	50
5.8	Measurement of the phase front with the XEVA USB camera for very different beam parameters	51
5.9	Phase front obtained by the simulation of the interference between beams using the beam parameters measured for the case in figure 5.8	52
5.10	Interference pattern for the measurement of the phase front presented in figure 5.8	52
5.11	Flow diagram of the program of the FPGA for the new application	54
5.12	Setup for the real-time measurement of the phase front with the InGaAs camera	54
5.13	Graphical User Interface (GUI) developed for the display of the data	55
5.14	Window to display the phase front	57

5.15	Palette chosen for the display of the phase front	58
5.16	Window that displays the maximum intensity on every pixel	59
5.17	Window to display the average of the intensity	60
5.18	Display of the contrast on every pixel	61
5.19	Window to display a frame of the dark fringe	62
6.1	Step 1: Alignment procedure of an interferometer	63
6.2	Step 2: Alignment procedure of an interferometer	63
6.3	Step 3: Alignment procedure of an interferometer	64
6.4	Step 4: Alignment procedure of an interferometer	64
6.5	Step 5: Alignment procedure of an interferometer	64
6.6	Step 6: Alignment procedure of an interferometer	65
6.7	Interference between two slightly tilted beams. Phase front measured with the XEVA USB camera	65
6.8	Phase front measured with the XEVA USB camera between two slight tilted beams	66
6.9	Phase front measured with the XEVA USB camera for a misaligned lens of a fiber injector. Different beam parameters	67
6.10	Frequency interferometer of the engineering model of the optical bench for the LTP	68
6.11	Phase front measured at the engineering model of the optical bench for the LTP with the XEVA USB camera	68
6.12	Homogeneous phase front obtained by the adjustment of the lenses in the fiber injectors on a tabletop interferometer	69
A.1	Diagram of n-blocks in cascade	71
A.2	Diagram of blocks connected in parallel	72
A.3	Representation of feedback in a block diagram	72
A.4	Displacement of bifurcation points in a block diagram	73
A.5	Displacement of summation points in a block diagram	73
A.6	Circuit of the bandpass filter used in the experimental setup	74
A.7	Block diagram of the bandpass filter shown in figure A.6	75
A.8	First simplification of the block diagram shown in figure A.7	76
A.9	Second simplification of the block diagram shown in figure A.7	76
A.10	Reduced block diagram of the bandpass filter shown in figure A.6	76
A.11	Large-signal differential voltage amplification of the OP27	77
A.12	Transfer function calculated for the bandpass filter in figure A.6 at a center frequency of 1600 Hz	78
A.13	Transfer function obtained by LISO for the bandpass filter in figure A.6 at a center frequency of 1600 Hz	78
A.14	Transfer function measured for the bandpass filter in figure A.6 at a center frequency of 1600 Hz	79
A.15	Transfer function calculated for the bandpass filter in figure A.6 at a center frequency of 290 Hz	79
A.16	Transfer function measured for the bandpass filter in figure A.6 at a center frequency of 290 Hz	80

List of Figures

1 Introduction

In his General Theory of Relativity, Albert Einstein introduced in 1916 a new model to describe Gravitation.

The General Theory of Relativity predicts that accelerated masses emit a part of their energy in the form of gravitational waves.

This prediction was studied on the pulsar PSR 1913+16, a binary system discovered in 1974 by Hulse and Taylor. The system was investigated for years and the results of the observations revealed a decrement of the oscillation period of this binary system over time. The analysis of the acquired data showed a strong accordance with the energy losses predicted by the emission of gravitational waves. For this indirect evidence of the existence of gravitational waves, Hulse and Taylor were awarded in 1993 the Nobel Prize in Physics.

Since the early 1960s, several scientific groups have been committed to obtaining direct verification of the existence of gravitational waves. To this end, a number of experimental configurations have been developed since then with the main purpose of accomplishing their detection.

Due to their minimal coupling interaction, the detection of gravitational waves is one of the most complex issues for experimental physicists. However, because of this small interaction gravitational waves are expected to be one of the most important sources to obtain information about the universe.

The current technology has been developed to a point where gravitational wave detectors can reach the necessary sensitivity to achieve their measurement. Hence, the detection of an actual gravitational wave can be expected soon.

Different configurations of gravitational wave detectors have been implemented such as resonant-bar detectors and laser-interferometric detectors. The scientific community has recently concentrated its efforts in the development of laser-interferometric gravitational wave detectors due to the high sensitivity that can be reached at wider bandwidths. The resonance bandwidth of resonant-bar detectors is very narrow.

At the moment, 5 main laser-interferometric detectors are operating in close cooperation: 2 American detectors LIGO, the Italian-French detector VIRGO, the Japanese detector TAMA300, and the German-British detector GEO600 close to Hanover.

The development of a gravitational wave detector in space has already started within the frame of a cooperation between the European Space Agency (ESA) and the American National Aeronautics and Space Administration (NASA).

This new detector LISA will complement the observations obtained by the ground-based detectors, since it is planned to observe gravitational waves in a low-frequency bandwidth which is inaccessible for a detector on Earth due to the seismic noise predominance at low frequencies.

Gravitational wave detectors provide means to study a variety of characteristics

of cosmological events, which are directly unmeasurable by conventional techniques.

LISA, together with the ground-based detector network, will be the equivalent of a huge gravitational wave observatory, which enables the detection and study of celestial phenomena unexplored and perhaps even unknown until now.

1.1 LISA

The Laser Interferometer Space Antenna (LISA) is a laser-interferometric gravitational wave detector in space. Its launch is expected for 2013. The main target of this mission is the detection of gravitational waves in a frequency range between 10^{-4} and 10^{-1} Hz [1]. It is expected that events such as massive black holes, binary coalescences at cosmological distances and enormous celestial catastrophes emit gravitational waves within this frequency range.

LISA is a constellation of 3 spacecraft positioned at the vertices of an equilateral triangle with an armlength of 5×10^6 km. The baricenter of this triangle rotates heliocentrically at a distance of 1 AU from the Sun and 20° behind the Earth. The plane of this assembly is 60° tilted with respect to the ecliptic as shown in figure 1.1.

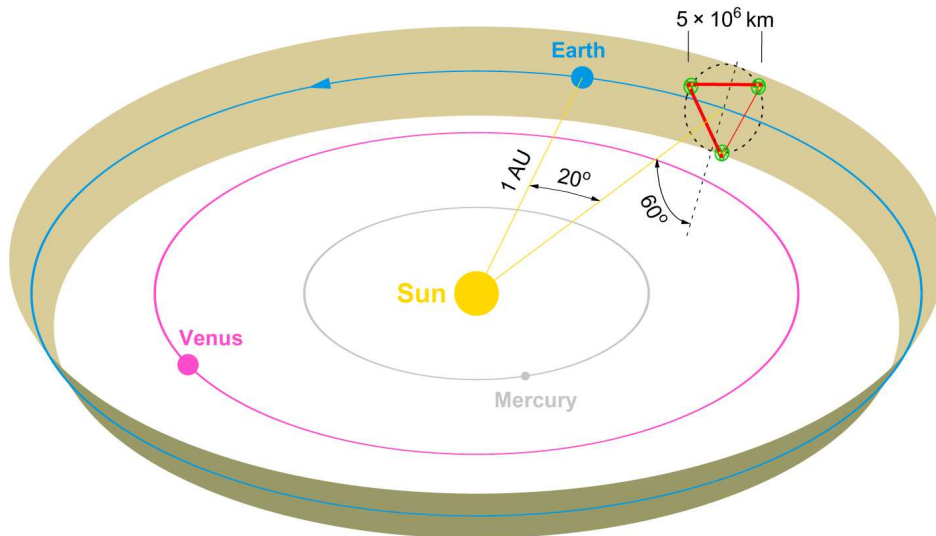


Figure 1.1: Heliocentric orbit of the spacecrafts constituting LISA

In analogy to the laser-interferometric ground-based detectors, the measuring principle of LISA is the detection of elongation in spacetime due to the influence of gravitational waves with a laser interferometer. LISA will perform heterodyne interferometry to measure the distance between the spacecraft with a strain sensitivity of $\frac{\delta L}{L} = 4 \times 10^{-21}/\sqrt{\text{Hz}}$. To achieve this sensitivity the influence of non-gravitational forces has to be suppressed to 3×10^{-15} N/ $\sqrt{\text{Hz}}$ at 3 mHz.

LISA could also be operated as a Michelson heterodyne interferometer with 3

arms to detect the elongation in the spacetime generated by gravitational waves. LISA might be also operated as a Sagnac interferometer, which strongly attenuates the gravitational wave signal, but allows the estimation of instrumental noise sources [2].

Before the actual construction of LISA can begin, the technologies must be tested to ensure a successful mission. To this end, LISA Pathfinder is being developed.

1.2 LISA Pathfinder

The task of LISA Pathfinder, previously called SMART-2, is to test the technologies developed for LISA until now. The mission consists of two separate research projects, which are the European LISA Technology Package (LTP), and the American project ST-7. LISA Pathfinder is planned to be launched in 2008.

Some of the components in LISA Pathfinder, which are essential for LISA, cannot be tested on Earth. These are the Inertial Reference Sensors (IRS) and the low-noise micronewton thrusters. A heterodyne Mach-Zender interferometer is used to verify the performance of the inertial reference sensors in the spacecraft.

The task of the inertial reference sensors is to isolate the test masses from non-gravitational effects such as variations in the pressure of electromagnetic radiation. The position of the test masses is measured by capacitive sensors. These give an input signal to correct the position of the satellite to guarantee a drag-free motion of the test masses.

The position of the satellite will be corrected by the micronewton thrusters, which compensate the influence of non-gravitational forces.

The interferometer will provide very precise information on the performance of the IRS. For this purpose, the interferometer needs to measure the position between the test masses with an accuracy of $10 \text{ pm}/\sqrt{\text{Hz}}$ between 3 mHz and 30 mHz. Therefore, an optical bench will be placed between the tanks containing the test masses. Figure 1.2 illustrates the LTP on board LISA Pathfinder. The interferometry concept for LISA Pathfinder is different from the interferometry planned for LISA. In spite of this fact, the technology developed for the LTP interferometer provides valuable knowledge to face the challenges represented by LISA.

The requirements on the LTP are demanding. However, the suppression of noise due to non-gravitational forces and the accuracy of the measurement of the distance between the test masses have been relaxed by an order of magnitude in frequency and sensitivity for LISA Pathfinder with respect to LISA, as shown by figure 1.3.

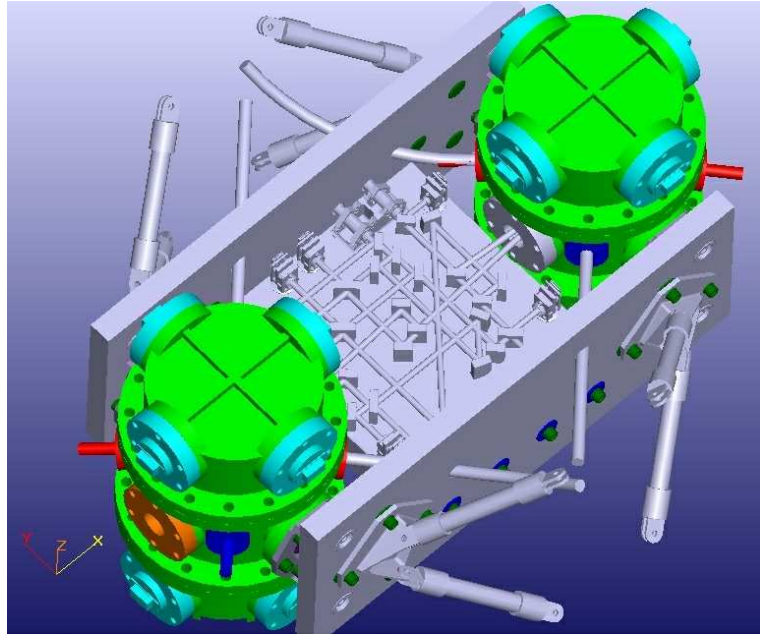


Figure 1.2: CAD model of the LISA Technology Package on board LISA Pathfinder. Illustrates the two tanks containing the test masses and the optical bench of the interferometer to measure the distance between them.

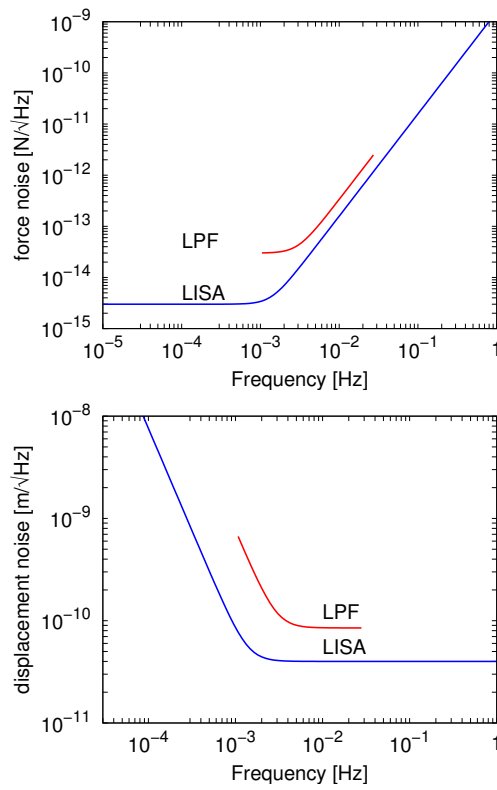


Figure 1.3: Force and displacement noise budgets for LISA and LISA Pathfinder

2 Interferometer on board LISA Pathfinder

This chapter describes the main components planned for the interferometer of the LISA Technology Package (LTP) on board LISA Pathfinder (LPF) and its required performance.

An explanation of the physics taking place at each stage of this interferometer configuration, as well as the principles of heterodyne interferometry are also provided.

2.1 Requirements on the Interferometry

The main goal of the LTP interferometer is to monitor the distance between two test masses. Thus, a verification of the Inertial Reference Sensors (IRS) is carried out as mentioned in the foregoing chapter. Figure 2.1 presents an schematic diagram of this measurement.

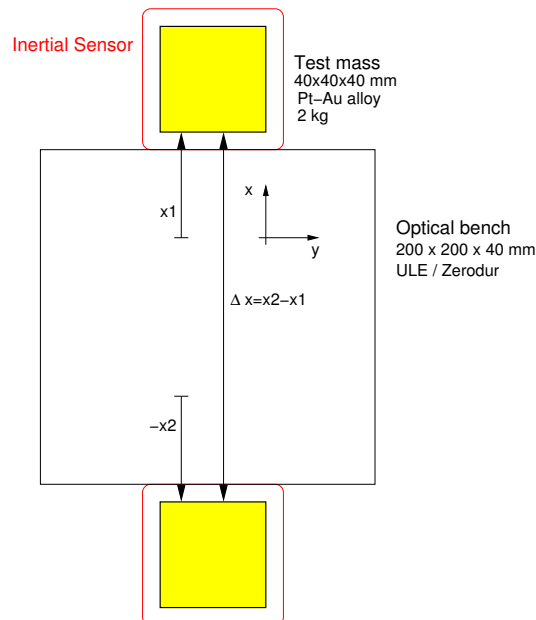


Figure 2.1: Measurement of the distance between the test masses

The position of the two drag-free masses have to be determined with an accuracy of $10 \text{ pm}/\sqrt{\text{Hz}}$ between 3 mHz and 30 mHz with a relaxation of $1/f^2$ towards 1 mHz. This precision must be obtained at mHz frequencies. Figure 2.2 [3]

shows the requirements on the phase measurement.

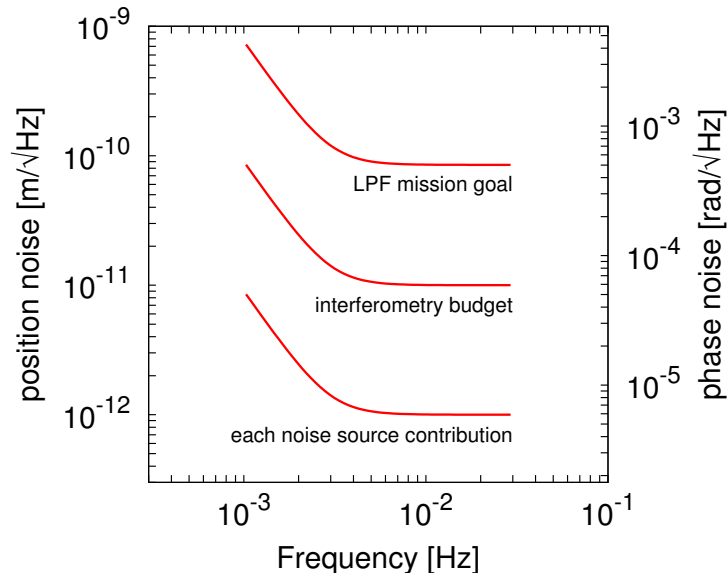


Figure 2.2: Requirements on the accuracy of LTP interferometer

In addition to overcome the interferometry obstacles, there are a number of other challenges that need to be addressed, such as the space qualification of optical and mechanical components on the optical bench.

Furthermore, it must be assured that after the launch and positioning of the satellite the interferometer and all its components remain adjusted and fully functional.

2.2 Interferometer Configuration

The distance between the two test masses in LISA Pathfinder can vary over many wavelengths of the light source, which is a Nd:YAG laser with a wavelength of 1064 nm. For this reason, conventional detectors, such as a Michelson interferometer operating on a dark fringe or a Fabry-Perot cavity, are not applicable to LISA Pathfinder, since they work at a fixed operation point and require actuators to act on the test masses to maintain it.

Therefore, a heterodyne Mach-Zender interferometer was chosen as the baseline configuration, due to its wide dynamic range, which enables to track the motion of the test masses over several wavelengths without losing information on the direction of the displacement. This configuration is illustrated in figure 2.3 and described in the next paragraph.

The laser beam from the Nd:YAG laser is split in two by a 50:50 beamsplitter. Each beam is separately frequency-shifted by an acousto-optic modulator (AOM). These electrical fields oscillate with frequencies which differ by the he-

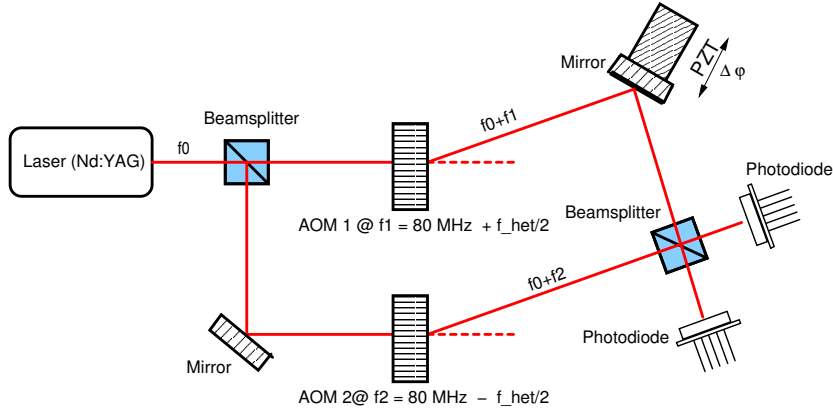


Figure 2.3: Heterodyne Mach-Zender Interferometer

terodyne frequency f_{het} .

The beams recombine at a beamsplitter generating a periodic signal on the photodiode. The phase of this signal yields the path difference between the two beams. The photocurrent generated at the photodiode oscillates with the heterodyne frequency.

Variations in the optical pathlength are detected as variations on the phase of the heterodyne signal. In the laboratory, a piezoelectric transducer coupled to a mirror simulates the variations on the optical pathlength.

2.2.1 Frequency shift by using Acousto-Optic Modulators

An acousto-optic modulator (AOM) consists of a piezoelectric transducer coupled to a crystal and is normally used to shift the frequency of a light beam. The piezoelectric element is driven by a RF signal, which generates acoustic waves in the crystal. These acoustic waves change the local density of the crystal, thus varying its index of refraction.

In this case, the behavior of the crystal can be compared with a classical grating, which is described by equation 2.1

$$\sin(\theta_m) = \frac{m \cdot \lambda_{\text{light}}}{d} = \frac{m \cdot \lambda_{\text{light}}}{\Lambda_s} \quad (2.1)$$

where d is the grating constant, $d = \Lambda_s$, $m=0, \pm 1, \pm 2, \dots$ the diffraction orders and λ_{light} is the wavelength of the light.

The laser beam is diffracted at angles θ_m . Figure 2.4 illustrates this phenomenon.

The sound waves oscillate with a frequency f_s . The wavelength of the acoustic waves is given by

$$\Lambda_s = \frac{v_s}{f_s} \quad (2.2)$$

where Λ_s is the wavelength of the acoustic waves and v_s is the speed of sound in the crystal.

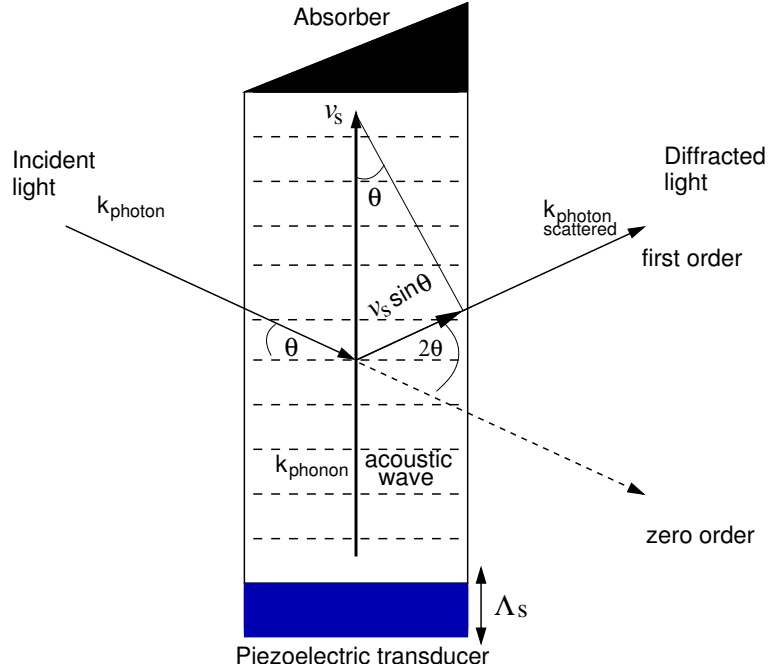


Figure 2.4: Diffraction of a light beam by acoustic waves in an acousto-optic modulator

The frequency shift arises from the fact that the acoustic waves are moving with respect to the reference system of the laboratory. This produces a Doppler shift on the frequency of the scattered photons.

The component of the velocity of the acoustic waves parallel to a scattered photon is $v_s \sin(\theta)$. Hence, the Doppler shift is given by

$$f_m = f_{\text{light}} \left(1 + \frac{v_s \sin(\theta)}{v_{\text{light}}} \right) \quad (2.3)$$

From equations 2.1 and 2.2

$$\Lambda_s \sin(\theta) = m \cdot \lambda_{\text{light}} \quad (2.4)$$

and

$$v_s \sin(\theta) = f_s \cdot \Lambda_s \sin(\theta) \quad (2.5)$$

For the photons scattered into the m -th order, the frequency shift is

$$f_m = f_{\text{light}} \left(1 + \frac{m \cdot f_s}{f_{\text{light}}} \right) = f_{\text{light}} + m \cdot f_s \quad (2.6)$$

This phenomenon can be also explained as an inelastic collision between the incident light (photon) and an acoustic wave (phonon), whereas these both are annihilated creating a new photon. When a photon of energy $E_{\text{photon}} = h f_{\text{light}}$ and momentum $\vec{p}_{\text{photon}} = \hbar \vec{k}_{\text{photon}}$ collides with a phonon of energy

$E_{\text{phonon}} = hf_s$ and momentum $\vec{p}_{\text{phonon}} = \hbar \vec{k}_{\text{phonon}}$, the momentum of the system must be conserved

$$\vec{p}_{\text{photon}_{\text{scattered}}} = \vec{p}_{\text{photon}} + \vec{p}_{\text{phonon}} \quad (2.7)$$

as well as the total energy

$$E_{\text{photon}_{\text{scattered}}} = hf_{\text{light}_{\text{scattered}}} = E_{\text{photon}} + E_{\text{phonon}} = hf_{\text{light}} + hf_s \quad (2.8)$$

From equation 2.8 the relation between the frequencies is given by

$$f_{\text{light}_{\text{scattered}}} = f_{\text{light}} + f_s \quad (2.9)$$

From this last equation, it is evident that a frequency shift of the diffracted light takes place by the frequency of the acoustic waves driving the piezoelectric transducer of the AOM.

2.2.2 Interference and Optical Heterodyne Detection

The frequency of the split beams is shifted by the heterodyne frequency by the method explained in section 2.2.1.

According to the notation used in [4], ρ is the amplitude reflectivity and τ the amplitude transmittance of a partially reflecting surface. These are positive real numbers with a value between 0 and 1, representing the reflected and transmitted amplitudes of the split beams. Neglecting the losses in the substrate, the transmitted and reflected power are such that

$$\rho^2 + \tau^2 = 1 \quad (2.10)$$

Therefore, a 50:50 beamsplitter has $\rho = \tau = \frac{1}{\sqrt{2}}$. Figure 2.5 shows the recombination of two beams at a beamsplitter.

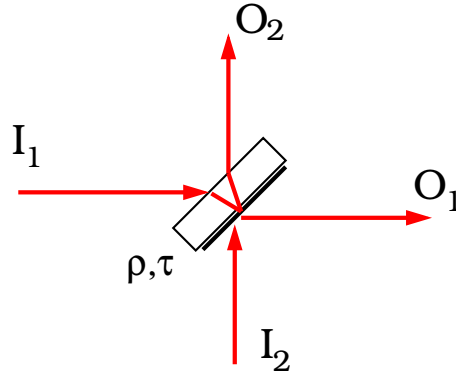


Figure 2.5: Amplitudes of the light fields at the beamsplitter

It is tempting to take the following approach, which is **wrong**, to calculate the transmitted and reflected light fields when the beams interfere at the beamsplitter as shown in figure 2.5

$$\begin{pmatrix} O_1 \\ O_2 \end{pmatrix} = \begin{pmatrix} \tau & \rho \\ \rho & \tau \end{pmatrix} \begin{pmatrix} I_1 \\ I_2 \end{pmatrix} \quad (2.11)$$

The outgoing power calculated by using equation 2.11 is given by

$$\begin{aligned}
 |O_1|^2 &= O_1 O_1^* = (\tau I_1 + \rho I_2)(\tau I_1^* + \rho I_2^*) = \tau^2 I_1 I_1^* + \rho^2 I_2 I_2^* + \tau\rho(I_1 I_2^* + I_1^* I_2) \\
 |O_2|^2 &= O_2 O_2^* = (\rho I_1 + \tau I_2)(\rho I_1^* + \tau I_2^*) = \rho^2 I_1 I_1^* + \tau^2 I_2 I_2^* + \tau\rho(I_1 I_2^* + I_1^* I_2) \\
 \underbrace{|O_1|^2 + |O_2|^2}_{\text{outgoing power}} &= \underbrace{(\rho^2 + \tau^2)}_1 \cdot \underbrace{(|I_1|^2 + |I_2|^2)}_{\text{incoming power}} + \underbrace{2\tau\rho \cdot (I_1 I_2^* + I_1^* I_2)}_{\text{complex extra term}}
 \end{aligned} \tag{2.12}$$

As it can be seen in equation 2.12, this result violates the conservation of energy, since the outgoing power cannot be greater than the incoming power.

Other relations which overcome this inconsistency by cancelling the extra term in equation 2.12 are proposed in [4] and [5], such as

$$\begin{pmatrix} O_1 \\ O_2 \end{pmatrix} = \begin{pmatrix} \tau & \rho \\ -\rho & \tau \end{pmatrix} \begin{pmatrix} I_1 \\ I_2 \end{pmatrix} \tag{2.13}$$

and

$$\begin{pmatrix} O_1 \\ O_2 \end{pmatrix} = \begin{pmatrix} i\tau & \rho \\ \rho & i\tau \end{pmatrix} \begin{pmatrix} I_1 \\ I_2 \end{pmatrix} \tag{2.14}$$

The latter equation is preferred by the author due to the symmetry of its matrix. The incoming fields can be described by

$$\begin{aligned}
 E_1(t) &= E_1 \cdot e^{i(\omega_1 t + \phi_1)} \\
 E_2(t) &= E_2 \cdot e^{i(\omega_2 t + \phi_2)}
 \end{aligned} \tag{2.15}$$

where $\omega_n = 2\pi \cdot f_n$ is the angular frequency and ϕ_n the phase of the field. The recombination of these beams is outlined by figure 2.6

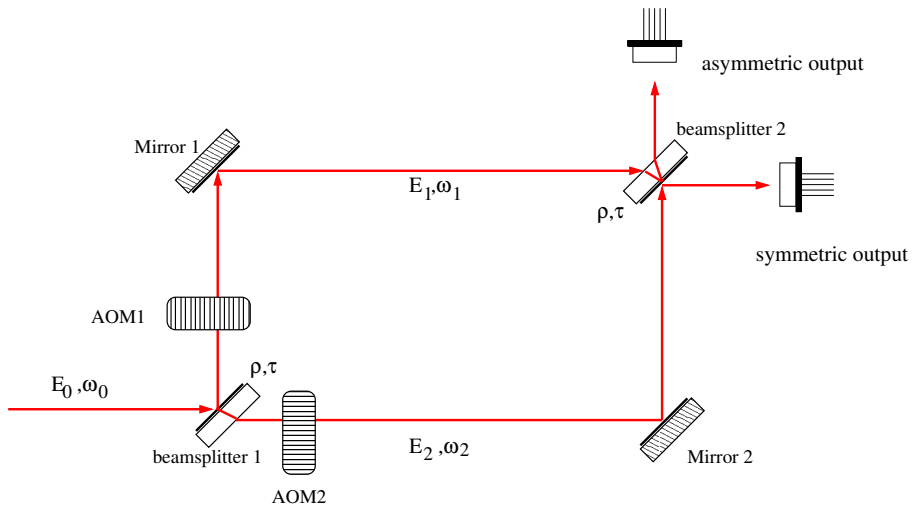


Figure 2.6: Recombination of the light fields at a beamsplitter in a Mach-Zehnder Interferometer

Hence, the interference of these light fields at a beamsplitter can be calculated by

$$\begin{aligned} \begin{pmatrix} E_{\text{sym}}(t) \\ E_{\text{asym}}(t) \end{pmatrix} &= \begin{pmatrix} i\tau & \rho \\ \rho & i\tau \end{pmatrix} \begin{pmatrix} E_1(t) \\ E_2(t) \end{pmatrix} \\ \begin{pmatrix} E_{\text{sym}}(t) \\ E_{\text{asym}}(t) \end{pmatrix} &= \begin{pmatrix} i\tau \cdot E_1 \cdot e^{i(\omega_1 t + \phi_1)} + \rho \cdot E_2 \cdot e^{i(\omega_2 t + \phi_2)} \\ \rho \cdot E_1 \cdot e^{i(\omega_1 t + \phi_1)} + i\tau \cdot E_2 \cdot e^{i(\omega_2 t + \phi_2)} \end{pmatrix} \end{aligned} \quad (2.16)$$

where $E_{\text{sym}}(t)$ and $E_{\text{asym}}(t)$ are the light fields emerging from the symmetric and asymmetric outputs of the beamsplitter respectively.

The intensity $I_{\text{sym}}(t)$ measured by a photodetector placed at the symmetric output (figure 2.6) would be proportional to $|E_{\text{sym}}|^2$

$$\begin{aligned} |E_{\text{sym}}|^2 &= |i\tau \cdot E_1 \cdot e^{i(\omega_1 t + \phi_1)} + \rho \cdot E_2 \cdot e^{i(\omega_2 t + \phi_2)}|^2 \\ &= \left(i\tau E_1 \cdot e^{i(\omega_1 t + \phi_1)} + \rho E_2 \cdot e^{i(\omega_2 t + \phi_2)} \right) \left(i\tau E_1 \cdot e^{i(\omega_1 t + \phi_1)} + \rho E_2 \cdot e^{i(\omega_2 t + \phi_2)} \right)^* \\ &= \left(i\tau E_1 \cdot e^{i(\omega_1 t + \phi_1)} + \rho E_2 \cdot e^{i(\omega_2 t + \phi_2)} \right) \left(-i\tau E_1 \cdot e^{-i(\omega_1 t + \phi_1)} + \rho E_2 \cdot e^{-i(\omega_2 t + \phi_2)} \right) \\ |E_{\text{sym}}|^2 &= \tau^2 \cdot E_1^2 + \rho^2 \cdot E_2^2 + i\tau\rho E_1 E_2 \underbrace{\left(e^{i(\omega_1 t + \phi_1)} - e^{-i(\omega_2 t + \phi_2)} \right)}_{2i \sin(\Delta\omega t + \Delta\phi)} \\ |E_{\text{sym}}|^2 &= \tau^2 \cdot E_1^2 + \rho^2 \cdot E_2^2 - 2\tau\rho E_1 E_2 \sin(\Delta\omega t + \Delta\phi) \end{aligned} \quad (2.17)$$

where $\Delta\omega = \omega_1 - \omega_2$ and $\Delta\phi = \phi_1 - \phi_2$.

In a similar way, a proportional expression $|E_{\text{asym}}|^2$ for the intensity $I_{\text{asym}}(t)$ of the light field coming out from the asymmetric output is given by

$$|E_{\text{asym}}|^2 = \rho^2 \cdot E_1^2 + \tau^2 \cdot E_2^2 + 2\tau\rho E_1 E_2 \sin(\Delta\omega t + \Delta\phi) \quad (2.18)$$

It can be seen from equations 2.17 and 2.18, that the signals from the two output ports of one single beamsplitter are shifted in the phase by exactly π .

The phases ϕ_1 and ϕ_2 represent the phases of the electrical fields $E_1(t)$ and $E_2(t)$ respectively. Variations in the length of one arm of the interferometer, due to the motion of a mirror coupled to a piezoelectric transducer or in LISA Pathfinder due to the motion of a test mass, change the phase of the corresponding light field by $\Delta\phi_{\text{meas}}$, so that

$$E_1(t) = E_1 \cdot e^{i(\omega_1 t + \phi_1 + \Delta\phi_{\text{meas}})} \quad (2.19)$$

$$E_2(t) = E_2 \cdot e^{i(\omega_2 t + \phi_2)}$$

This phase shift will affect both measured signals equally, so that the phase of the heterodyne signal will change with respect to a reference (see figure 2.7).

$$I_{\text{sym}}(t) \propto \tau^2 \cdot E_1^2 + \rho^2 \cdot E_2^2 - 2\tau\rho E_1 E_2 \sin(\Delta\omega t + \Delta\phi + \Delta\phi_{\text{meas}}) \quad (2.20)$$

$$I_{\text{asym}}(t) \propto \rho^2 \cdot E_1^2 + \tau^2 \cdot E_2^2 + 2\tau\rho E_1 E_2 \sin(\Delta\omega t + \Delta\phi + \Delta\phi_{\text{meas}})$$

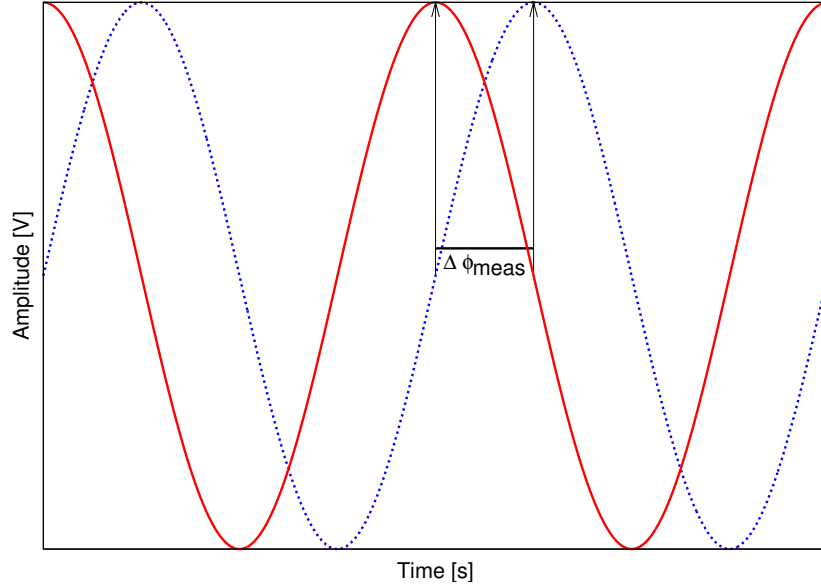


Figure 2.7: Phase difference between 2 heterodyne signals

The changes in the pathlength ΔL of one interferometer arm and the phase shift $\Delta\phi_{\text{meas}}$ are related by

$$\Delta\phi_{\text{meas}} = \frac{2\pi \Delta L}{\lambda} \quad (2.21)$$

where λ is the average wavelength of the two light fields $E_1(t)$ and $E_2(t)$ oscillating at the frequencies ω_1 and ω_2 respectively.

The phase shift $\Delta\phi$ from equation 2.20 will be omitted from now on, since it remains constant and does not contribute to the measurement of changes in the optical pathlength. Hence, the time dependency of the heterodyne signal can be expressed by

$$\cos(\varphi) = \cos(\Delta\omega t + \Delta\phi_{\text{meas}}) = \cos\left(2\pi f_{\text{het}} \cdot t + \frac{2\pi \Delta L}{\lambda}\right) \quad (2.22)$$

2.2.3 Contrast and Interference Pattern

The heterodyne signal measured by a photodetector can be illustrated, in general, by figure 2.8.

The contrast c is a parameter that gives information on how well the two beams are interfering, and can be calculated as follows

$$c = \frac{I_{\text{max}} - I_{\text{min}}}{I_{\text{max}} + I_{\text{min}}} \quad (2.23)$$

The contrast can only have values between 0 and 1. The interference pattern $I(\varphi)$ is given by

$$I(\varphi) = A \cdot (1 + c \cdot \cos(\varphi)) \quad (2.24)$$

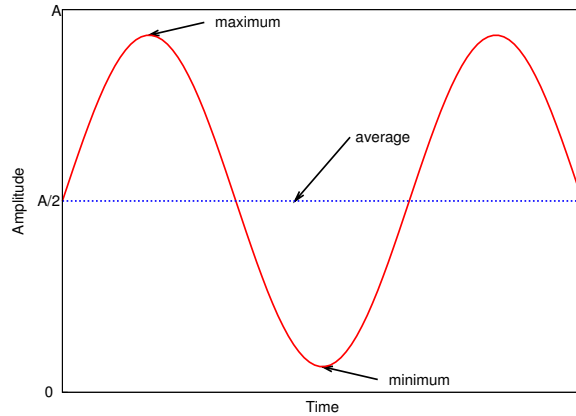


Figure 2.8: Heterodyne signal measured by a photodetector

where A is the amplitude of the signal measured by the photodetector, and $\cos\varphi$ is given by equation 2.22.

2.3 LISA Pathfinder Interferometer Setup

In LISA Pathfinder, the interferometer consists of two separated parts. The modules of the LPF interferometer are illustrated in figure 2.9.

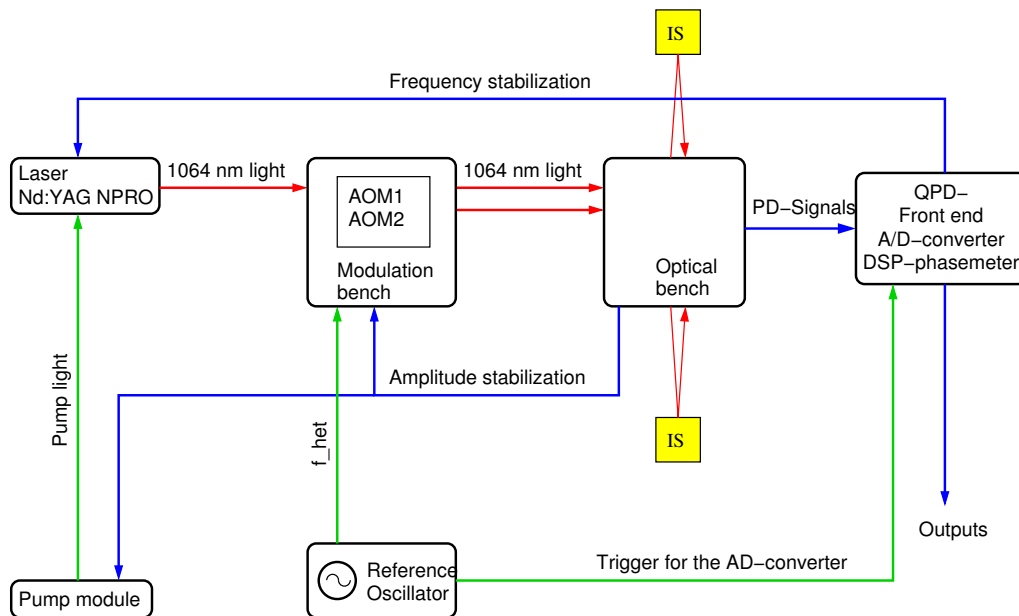


Figure 2.9: Schematic of the modules conforming the LPF interferometry system

One part is the modulation bench, where the main beam is split by a beam-splitter. The two beams are shifted in frequency by acousto-optic modulators

and each is coupled into a fiber and taken to the optical bench, where the actual interferometry takes place.

The components on the optical bench were bonded to a zerodur plate to form a quasi-monolithic unit with a low susceptibility to temperature variations.

The following sections introduce the modulation and the optical bench developed for the LTP.

2.3.1 Modulation Bench

In the modulation bench, the main laser is split into two beams by a beamsplitter. These two beams will be modulated each by an acousto-optic modulator driven by a RF signal of about 1W.

The acoustic signal coupled to the piezoelectric transducers in the AOMs oscillates with a frequency of approximately 80 Mhz. Figure 2.10 presents a diagram of the modulation bench.

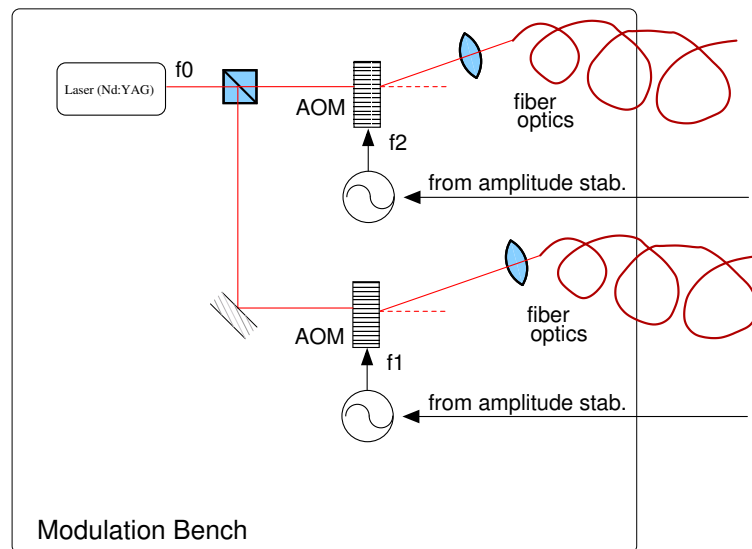


Figure 2.10: Schematic of the Modulation Bench on LPF

The shifted beams are coupled into fiber optics and injected to the optical bench. The modulation bench receives input signals from the optical bench for the control loops in charge of the frequency stabilization of the laser and amplitude stabilization of the RF signals driving the AOMs.

A photo of the space-qualified laser developed by the company TESAT-Spacecom GmbH for the LISA technology package is shown in figure 2.11.

A photo of the prototype for a space qualifiable modulation bench developed by the company Contraves AG is shown in figure 2.12. This prototype contains two AOMs coupled to fiber optics at the first diffraction order. It has one optical input for the main laser and two inputs for the RF signals driving the AOMs. It also provides two optical outputs for the frequency modulated beams.

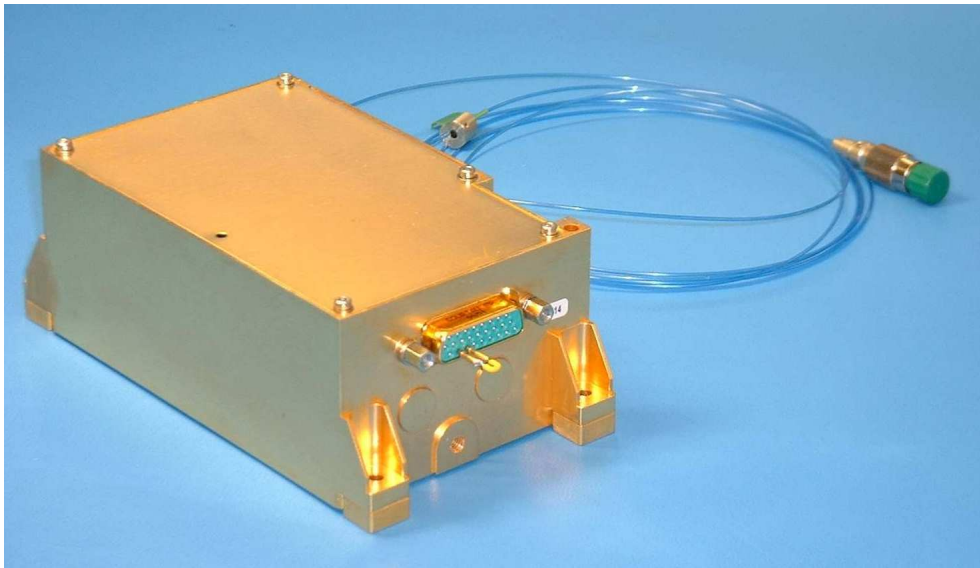


Figure 2.11: Space-qualified NPRO-laser developed by TESAT



Figure 2.12: Prototype for a space qualifiable modulation bench developed by Contraves

2.3.2 Optical Bench

The optical bench consists of 4 different interferometers, whose optical components are bonded to a single zerodur plate. One of these interferometers gives a reference for the phase measurement. Figure 2.13 presents a diagram of this interferometer.

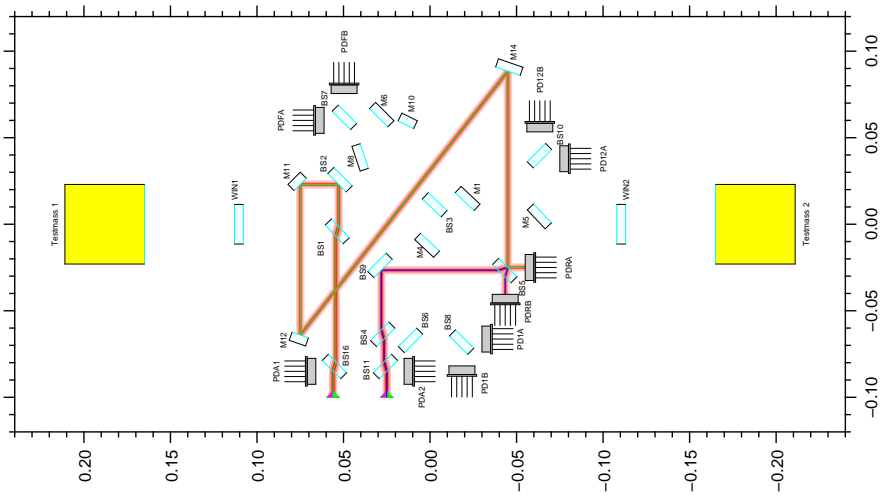


Figure 2.13: Opto-CAD model of the reference interferometer on the optical bench¹

It is important to remark that the armlengths of this interferometer on the optical bench are not equal. Nevertheless, the effective optical pathlengths are equal, since this difference is compensated by the length of each fiber. This difference in the length of the fiber optics is approximately 39 cm.

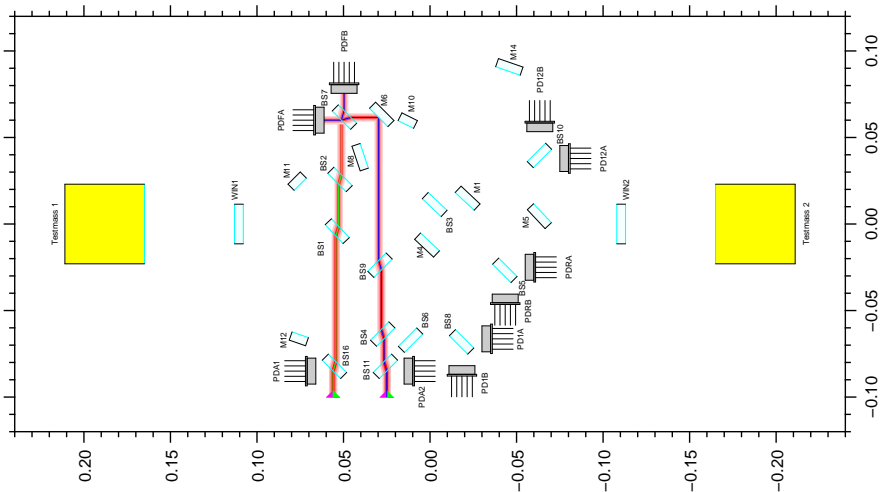


Figure 2.14: Opto-CAD model of the frequency interferometer on the optical bench¹

¹by Gerhard Heinzel

Another interferometer, presented in figure 2.14, provides an input signal for the regulation of the frequency of the laser on the modulation bench. The effective armlengths for this interferometer are intentionally unequal. Thus, the interferometer is sensitive to the frequency fluctuations of the laser source. Two interferometers perform the actual measurement planned for interferometry of the LTP. The X1 interferometer measures the distance from the test mass 1 to the optical bench, as shown in figure 2.15. The X1-X2 interferometer, in figure 2.16, measures the distance between the two test masses.

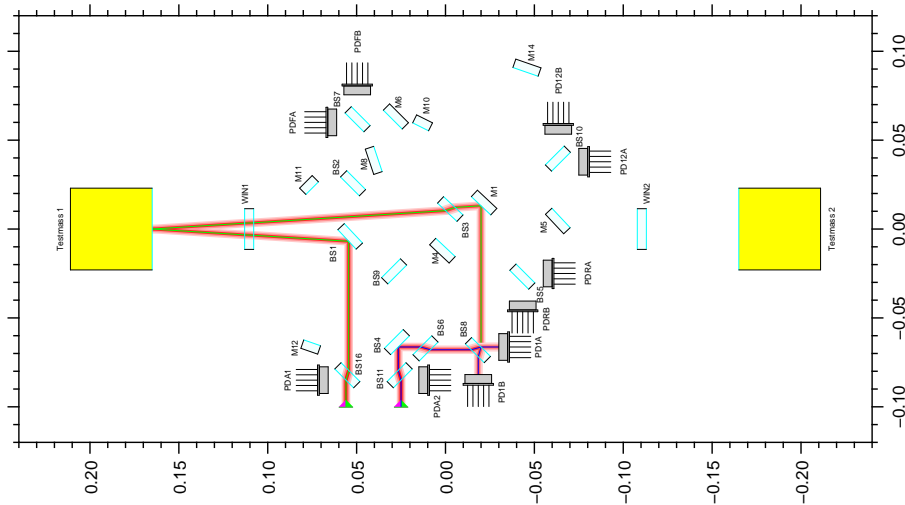


Figure 2.15: Opto-CAD model of the X1 interferometer on the optical bench ¹

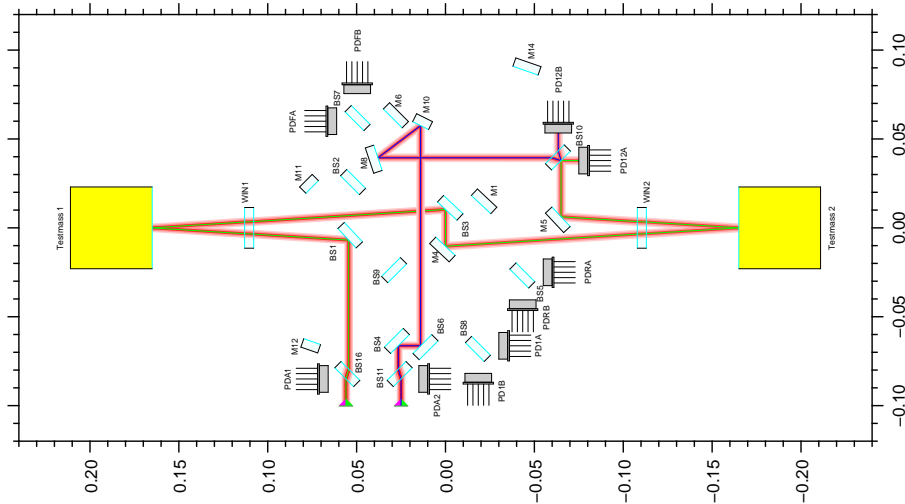


Figure 2.16: Opto-CAD model of the X1-X2 interferometer on the optical bench ¹

¹by Gerhard Heinzel

Figure 2.17 shows a photograph of the actual engineering model of the LTP optical bench, currently at the AEI in Hanover.

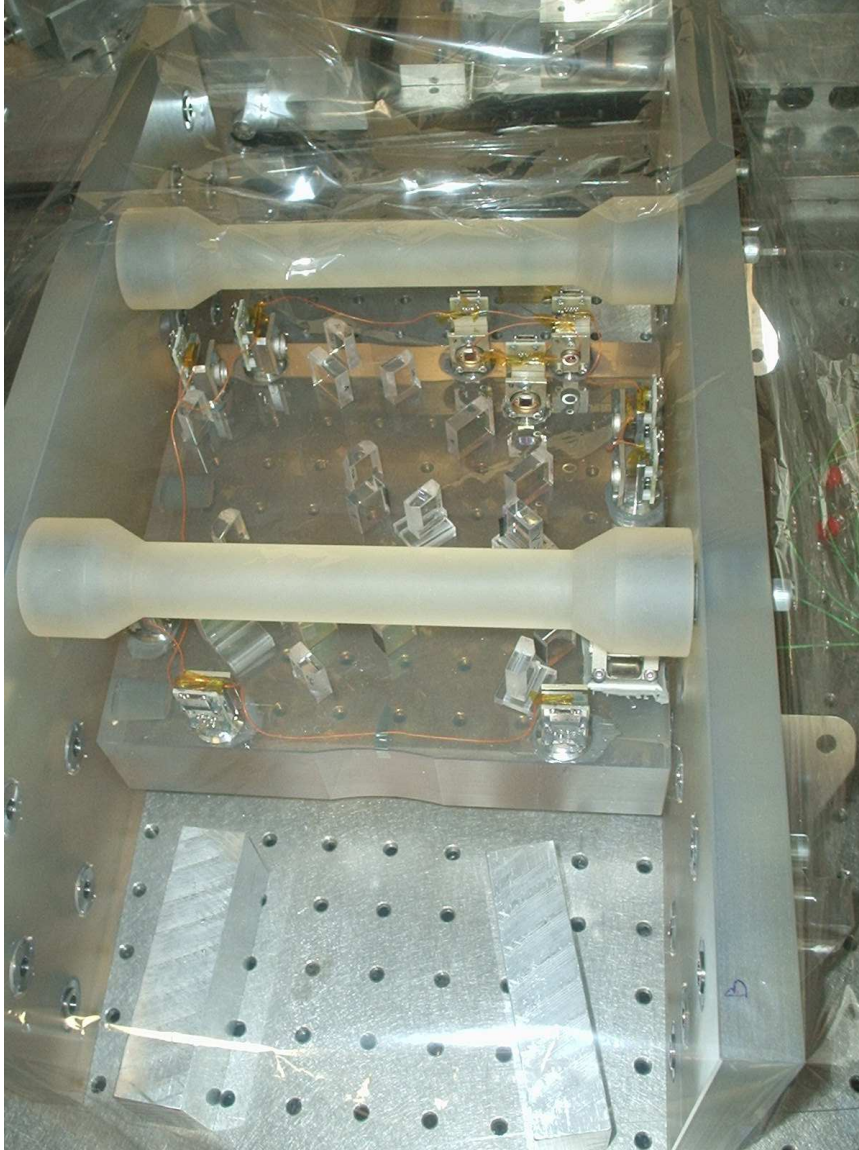


Figure 2.17: Engineering Model of the LPF Optical Bench built by the Rutherford Appellton Laboratory and EADS Astrium

This model was built by the Rutherford Appellton Laboratory (RAL) in cooperation with the University of Glasgow, the Albert Einstein Institute (AEI), and EADS Astrium.

This prototype passed the thermal and mechanical tests carried out at TNO-TPD in Delft, which are an important part of the space qualification process. The experience earned and the technology developed by the construction of this prototype builds a solid basis for the development of the final flight model of the LTP optical bench on board LISA Pathfinder.

2.4 Electronic System

The electronic system is a key component of the LPF interferometry. It consists mainly of the AOM drivers with their phase-locked loop, that is in charge of locking the frequencies of the oscillators in the AOM drivers to the heterodyne frequency.

2.4.1 Driver for the Acousto-Optic Modulators

The drivers for the acousto-optic modulators consist mainly of analog oscillators at 80 MHz and a power amplifier, which raises the power of the signal up to 2 W.

The drivers provide two low-power outputs, one at 80 MHz and the other one at 5 MHz. These serve as input signals for the control loops that regulate the frequency and phase locking on the PLL.

Two control inputs can be used for amplitude modulation of the RF signals and the frequency locking. Figure 2.18 shows a diagram of the AOM-drivers.

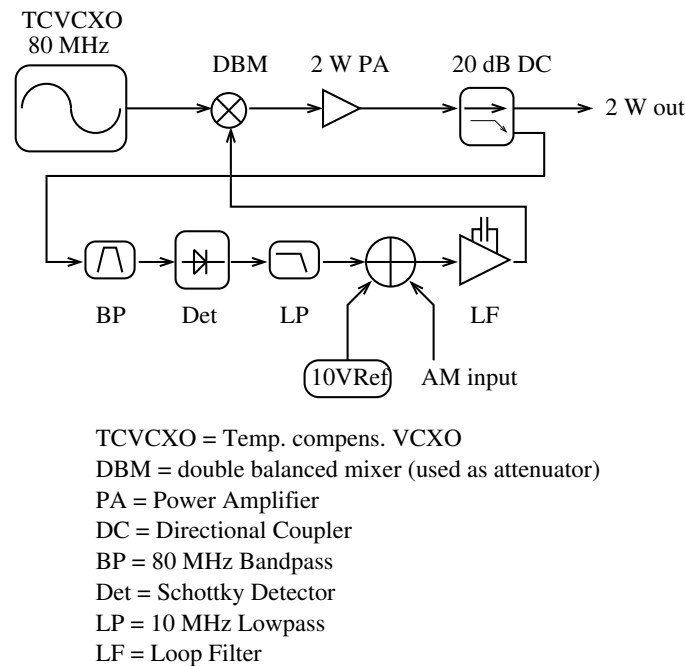


Figure 2.18: Block-diagram of the AOM-Drivers¹

2.4.2 Phase-Locked Loop (PLL)

The phase-locked loop is an electronic system responsible for regulating the frequencies of the RF signals driving the acousto-optic modulators. Figure 2.19 outlines the electronic components and signals integrating the PLL.

¹developed by Gerhard Heinzel

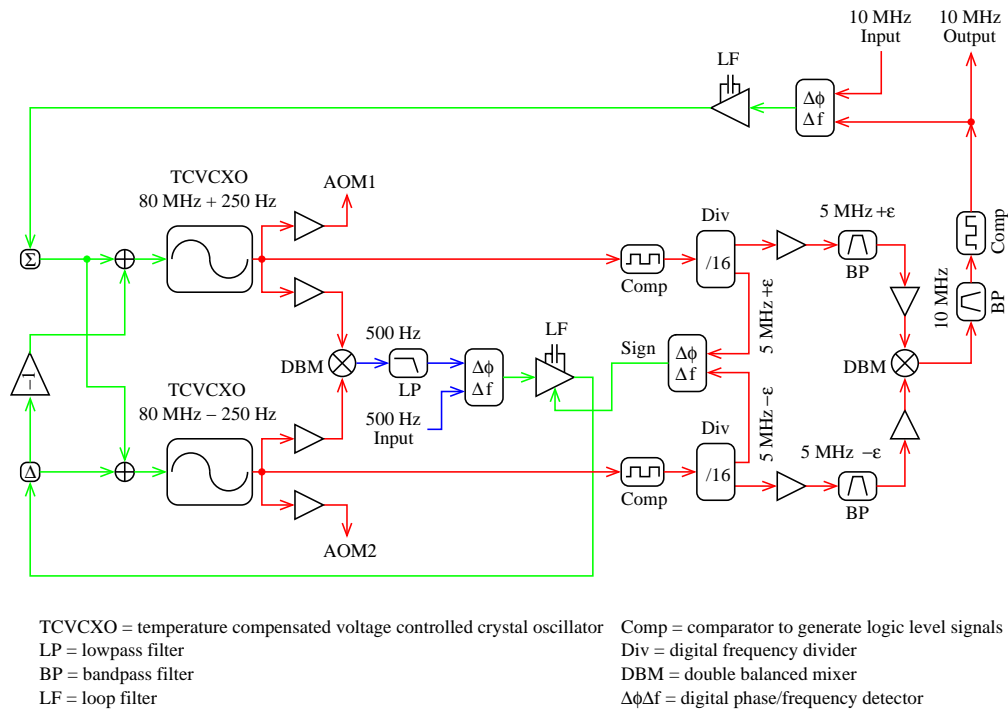


Figure 2.19: Block-diagram of the PLL¹

Signals taken from the AOM-drivers are compared to provide an input signal for the frequency and phase lock of the oscillators. The oscillators are locked to a frequency difference that equals the heterodyne frequency.

A 10 MHz digital oscillator gives the reference for the heterodyne frequency and the sampling frequency of the data acquisition system. Both signals come from the division of this 10 MHz reference by a divide-by-N counter and are therefore coherent.

2.4.3 Real-Time Digital Phasemeter

A digital phasemeter was developed (see [6]) at the Albert Einstein Institute for the data acquisition and data analysis of the phase measurements performed on all four interferometers of the optical bench.

The phasemeter consists mainly of a data acquisition system and software that enables the real-time analysis of the data. The data acquisition system is composed of an anti-aliasing filter, a sample and hold system, and the data acquisition processor DAP1216a from Microstar Laboratories. This processor has a 16-bit Analog-Digital-Converter and is placed on a normal PC as an ISA-Card. Figure 2.20 shows a diagram of the data acquisition system.

Several intensity samples are acquired over many periods of the heterodyne signal, in order to calculate a single value for the phase. A Single Bin Discrete Fourier Transform (SBDFFT, [6]) is applied to these time series to obtain

¹developed by Gerhard Heinzl

the phase of the heterodyne signal. Moreover, this phasemeter estimates the contrast measured at each photodetector and the phase difference of this signal to the reference interferometer. Its graphical user interface (GUI) supports the user by the adjustment of the interferometer. The photodetectors used for the phase measurement on the optical bench are quadrant photodiodes, which enable differential wave front sensing to detect rotations or tilting on the test masses. Figure 2.21 presents the GUI of the phasemeter.

A new phasemeter based on FPGAs (Field Programable Gate Array) is being developed at the moment at the AEI Hanover, which will simplify the electronic system and improve its performance.

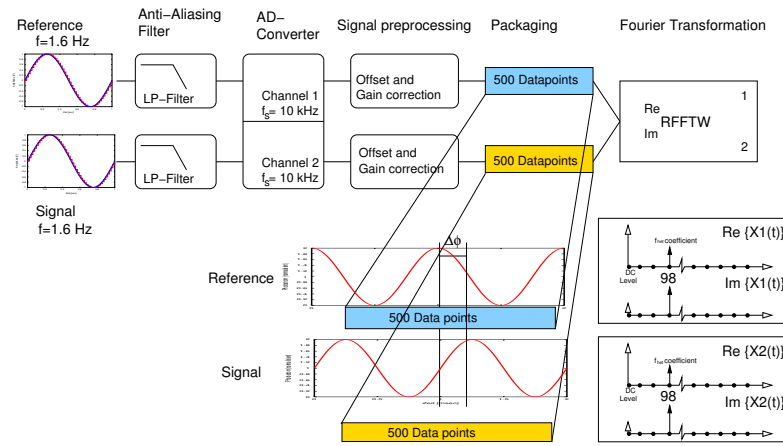


Figure 2.20: Block-diagram of the data acquisition system¹

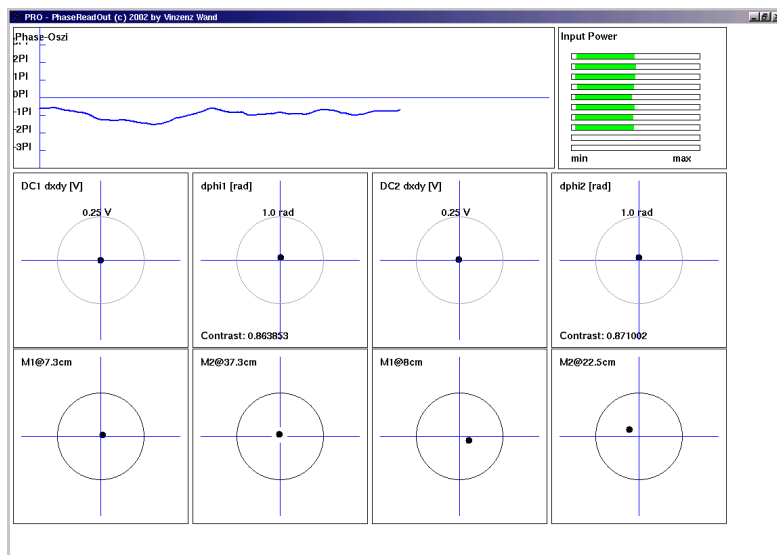


Figure 2.21: Graphical User Interface of the phasemeter¹

¹by Vinzenz Wand

2.5 Motivation

The actual motivation for this work is based on the performance measurements conducted on a tabletop interferometer with single-element photodiodes and quadrant photodiodes at the AEI Hanover. Similar measurements were performed on bonded interferometers developed at the University of Glasgow, due to their pathlength stability, and measured with the phasemeter developed at the AEI Hanover. Figure 2.22 presents the results obtained by the measurements performed in Glasgow.

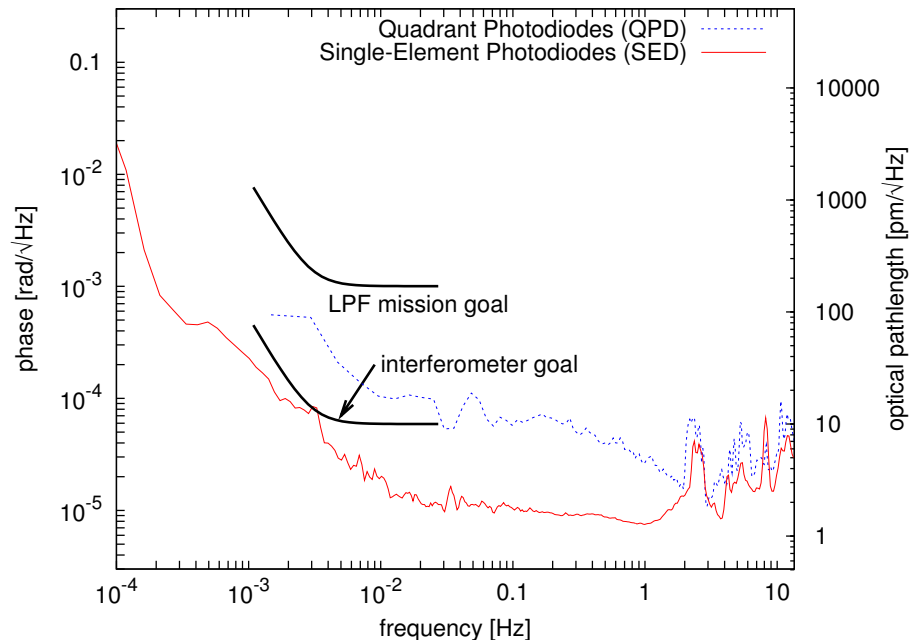


Figure 2.22: Noise level measured on a bonded prototype for the optical bench

These curves show the sensitivity reached by the phase measurement system on two interferometers bonded to the same plate.

The dashed curve presents the noise level obtained by measuring with quadrant photodiodes (QPD), and the solid curve by measuring with single-element photodiodes (SED).

As it can be read from the graph, the performance of the system is approximately 6 times worse by measuring with quadrant photodiodes than the sensitivity achieved with single-element photodiodes. However, the quadrant photodiodes are necessary to apply the differential wavefront sensing technique (DWS, see [6]) to detect any rotations or tilting on the test masses.

These results pose the question of why the sensitivity of the system with quadrant photodiodes is worse when the conditions for both measurements are the same.

The photodetectors, QPD and SED, are composed of the same semiconductor material (IR-enhanced silicon), having thus comparable physical properties.

The main difference between both kinds of photodetectors is the slit at the QPD separating the quadrants (see figure 2.23), which is approximately $50\ \mu\text{m}$ wide for typical devices.



Figure 2.23: Single-element photodiodes and quadrant photodiodes

The assumption made in this work to explain the deterioration of the performance by using QPD is that some information might be overlooked at the slit separating the quadrants. If the beam jitters on them [7] and the phase front presents an inhomogeneous spatial distribution, the slit would cut off sections of the phase front losing this information completely (figure 2.24).

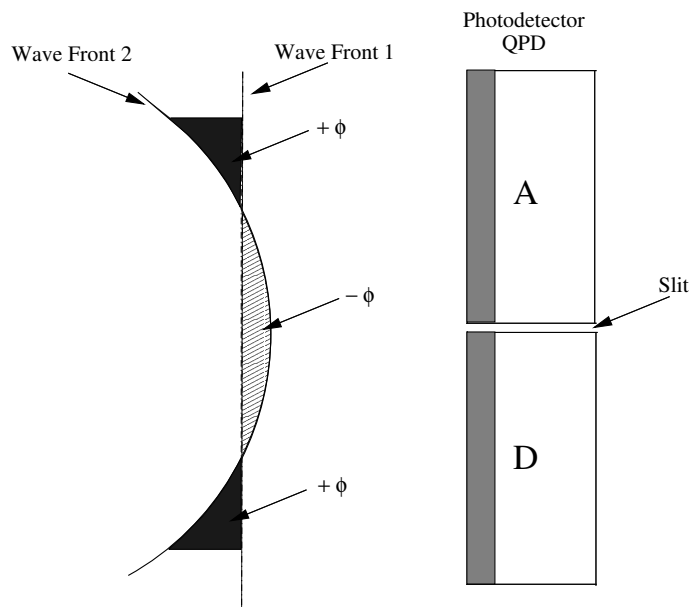


Figure 2.24: Overlapped wave fronts of interfering beams whose parameters are different. Inhomogeneous phase front

Although it is commonly assumed that a spatially homogeneous phase front will be obtained from the interference of two gaussian beams, this assumption is only valid when the profile of both beams is equal at the plane in which they interfere. This means that both beams should have the same beam parameters (distance to waist and Rayleigh range).

In order to analyze the geometry of the phase front (before this thesis began) a measurement was conducted by using a pin hole covering a single-element photodiode on a tabletop interferometer. The pin hole was moved by a x-y-table over the whole surface, sampling different sections of the beam. The phasemeter

was used to measure the phase at each position, obtaining hereby the spatial distribution of the phase. The results of this measurement are presented in figure 2.25.

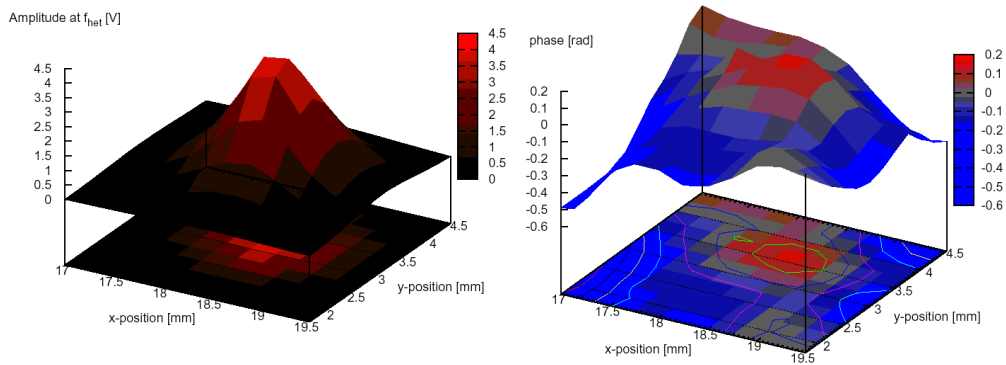


Figure 2.25: Phase front measured by using a pin hole over a single-element photodiode¹

Although the spatial resolution of this measurement is very low, it can be seen that the phase front does not present a homogeneous spatial distribution. This suggests that the profile of the interfering beams is different at the plane they recombine.

Even though both beams come from the same light source, their parameters are changed independently by coupling into fiber optics at the modulation bench (figure 2.10). If the lenses in the fiber injectors at the optical bench are not adjusted properly the wave front of the beams will not be affected uniformly. This fact plays an important role in measurements with quadrant photodiodes, since different sections of the phase front will be lost at the slit due to the beam jitter, obtaining different values for the measured phase.

One possibility to correct this problem would be to adjust the lenses of the fiber injectors, in order to countervail the difference between both beams to compensate their parameters. Before this technique can be utilized, a more precise picture of the phase front must be obtained in real-time and with a much higher spatial resolution than the one achieved in the measurement of figure 2.25. Moreover, the procedure followed to obtain this data is not only tedious enough, but makes also impossible neither to reach a significant spatial resolution of the phase front nor to adjust the fiber injectors on-line, according to the measured structure of the phase front.

Therefore, the idea emerged of using a spatially resolving photodetector, such as a CCD camera, to perform this measurement. Such a device allows to reach a high spatial resolution in the measurement and enables a real-time display of the phase front. To accomplish such a measurement, it is necessary to find a method to measure the phase by using this kind of device.

An explanation of a well known method for the estimation of the phase out of few intensity samples is given in chapter 3.

¹measured by Vinzenz Wand and Antonio Francisco García Marín

3 Phase Estimation Method

The algorithm used by the phasemeter mentioned in section 2.4.3 requires several intensity samples to estimate a single value for the phase of the heterodyne signal. The hardware for the data acquisition and the photodetectors used enable a real-time processing of the data, since the photodiodes are fast enough to continuously track the beat note generated by the inference of both laser beams. The intensity information acquired by every pixel of a CCD camera, however, cannot be read fast enough.

In this section, a well known method to estimate the phase of a signal out of very few intensity samples is presented.

3.1 Theoretical Approach

As explained in section 2.2.3, the interference pattern oscillates according to

$$I(\varphi) = A \cdot (1 + c \cdot \cos(\varphi)) \quad (3.1)$$

where I is the intensity of the signal, which can be written as a function of the phase $\varphi = \omega_{\text{het}} \cdot t + \phi$ as shown by equation 2.22 in section 2.2.2. A is the amplitude of the signal measured by the photodetector, and c is the contrast. In order to calculate the phase from a small number of intensity samples, it is necessary to discretize the intensity I in terms of the phase φ . Then each sample I_k can be expressed as a function of the phase by

$$I_k = I(\varphi + k \cdot \delta) \quad (3.2)$$

where δ is known as the phase shift representing the phase step between two consecutive intensity samples. This means that each sample has to be separated from its immediate neighbors in the phase by δ .

For experimental purposes in this thesis, the variation of δ is realized by varying time delays given by

$$\delta = \omega_{\text{het}} \cdot (n \cdot T_{\text{het}} + \Delta t) \quad (3.3)$$

where n is an integer number, $T = 1/f_{\text{het}}$ is the period of the heterodyne signal, and Δt is defined by the phase estimation algorithm.

The main idea of this method is to obtain a Discrete Fourier Transform of the signal. The argument of the Fourier Transform at the main frequency corresponds to the phase of the signal. Hence, the phase φ can be hence calculated as

$$\varphi = \arctan \left(\frac{\sum_{k=0}^{M-1} b_k \cdot I_k}{\sum_{k=0}^{M-1} a_k \cdot I_k} \right) = \arctan \left(\sum_{k=0}^{M-1} c_k \cdot I_k \right) = \arctan(S(\varphi)) \quad (3.4)$$

with

$$S(\varphi) = \sum_{k=0}^{M-1} c_k \cdot I_k \quad (3.5)$$

where $c_k = a_k + i \cdot b_k$ and M is the number of samples I_k needed by the algorithm to estimate a phase, which varies between $-\pi$ and π .

For example, in one common phase estimation algorithm, b_k and a_k are chosen to be proportional to a sine and cosine function respectively, to obtain a Discrete Fourier Transform of the signal

$$a_k \propto \cos(k \cdot \delta) \quad (3.6)$$

$$b_k \propto \sin(k \cdot \delta) \quad (3.7)$$

The intensity $I(\varphi)$ can be expanded in a Fourier series as

$$I(\varphi) = \sum_{n=-\infty}^{+\infty} \alpha_n \cdot e^{i \cdot n \varphi} \quad (3.8)$$

where the coefficient α_n corresponds to the magnitude of the intensity in the n -th order. Additionally, the oscillating term of the intensity $I(\varphi)$ in equation 3.1 is proportional to $\cos(\varphi)$, this implies for the coefficients of the orders n and $-n$ that $\alpha_n = \alpha_{-n}$, due to the symmetry of the Fourier transform of the cosine.

From this expression for $I(\varphi)$, the intensity sample I_k can be expressed, according to equation 3.2, as

$$I_k = \sum_{n=-\infty}^{+\infty} \alpha_n \cdot e^{i \cdot n(\varphi + k\delta)} \quad (3.9)$$

The function $S(\varphi)$ can be expanded in a Fourier series as well

$$S(\varphi) = \sum_{n=-\infty}^{+\infty} s_n \cdot e^{i \cdot n \varphi} = \sum_{n=-\infty}^{+\infty} S_n(\varphi) \quad (3.10)$$

An expression related to the intensity I_k can be found by substituting the equation 3.9 into equation 3.5 as follows

$$\begin{aligned} S(\varphi) &= \sum_{k=0}^{M-1} c_k \cdot \sum_{n=-\infty}^{+\infty} \alpha_n \cdot e^{i \cdot n(\varphi + k\delta)} \\ S(\varphi) &= \sum_{n=-\infty}^{+\infty} \alpha_n e^{i \cdot n \varphi} \underbrace{\sum_{k=0}^{M-1} c_k e^{i \cdot nk\delta}}_{S_n(\varphi)} \end{aligned} \quad (3.11)$$

where $S_n(\varphi)$ is the n -th Fourier component of $S(\varphi)$.

A very useful technique to design an algorithm for the estimation of the phase, based on this formalism, is the so called Characteristic Polynomial Method (CP, [8]). In this method a complex polynomial $P(x)$, whose coefficients correspond

to the coefficients $c_k = a_k + i \cdot b_k$ presented in equation 3.4, is defined. A characteristic polynomial $P(x)$ can be generally expressed by

$$P(x) = \sum_{k=0}^{M-1} c_k \cdot x^k \quad (3.12)$$

From this expression for $P(x)$ and considering equation 3.11, the n -th Fourier component $S_n(\varphi)$ of the function $S(\varphi)$ can be given in terms of P by

$$\begin{aligned} S_n(\varphi) &= \alpha_n e^{i \cdot n \varphi} \sum_{k=0}^{M-1} c_k \cdot \left(e^{i \cdot n \delta} \right)^k \\ S_n(\varphi) &= \alpha_n e^{i \cdot n \varphi} \cdot P \left(e^{i \cdot n \delta} \right) \end{aligned} \quad (3.13)$$

In order to design an algorithm that provides a significant result for the phase, it is necessary to choose a set of coefficients c_k that cancels all the components $S_n(\varphi)$ of the function $S(\varphi)$ except for the component $S_1(\varphi)$ given by the first order $n = 1$, since this is the component of the Fourier Transform at the right frequency.

Nevertheless, the dependency between $S_n(\varphi)$ and $S(\varphi)$ shown in equation 3.10 demands an infinite set of equations to obtain the coefficients required to achieve this, this implies that the number of samples M has to be infinite as well.

However, a finite set of coefficients c_k can be found to suppress only those components which have a strong influence to $S(\varphi)$ due to their magnitude.

To select the appropriate coefficients, it must be considered that the amplitude of the order $n = 0$, which corresponds to the DC average of the light power, has always a large amplitude. Therefore, its contribution strongly affects the function $S(\varphi)$. Furthermore, the amplitudes of the harmonics $n = -1$ and $n = 1$ are equal, this suggests that the order $n = -1$ must be removed.

Normally, the amplitude of the higher harmonics decrease rapidly, diminishing their influence to the result of $S(\varphi)$. For this reason, their elimination is not a complicated issue. Nevertheless, to consider their suppression in the algorithm will increase easily the number of samples required for a phase estimation.

The number of samples M is determined by the algorithm and corresponds to the order of its characteristic polynomial $M - 1$.

According to equation 3.13, the general form of the characteristic polynomial of an algorithm meant to suppress j harmonics is given by

$$P(x) = \gamma \cdot \prod_{\beta=0}^j \left(x - \left(e^{i \delta} \right)^{\Omega_\beta} \right) \quad (3.14)$$

where Ω is a vector consisting of j components and its component $\Omega_\beta = n$ is the order of the harmonic $S_n(\varphi)$ to be suppressed by the algorithm.

$$\Omega = \{\Omega_0, \Omega_1, \dots, \Omega_j\} \quad (3.15)$$

For example, $\Omega = \{0, -1, 2, -2\}$ for the suppression of the harmonics $S_0(\varphi)$, $S_{-1}(\varphi)$, $S_2(\varphi)$ and $S_{-2}(\varphi)$ respectively.

Equation 3.13 also shows that when $P\left(\left(e^{i\delta}\right)^n\right) = 0$, $S_n(\varphi)$ vanishes. Therefore, the term $\left(e^{i\delta}\right)^n$ must be a root of the polynomial $P(x)$, hence the form $\left(x - \left(e^{i\delta}\right)^n\right)$ of equation 3.14.

The complex coefficient γ can be chosen arbitrarily, since it only describes aliased versions of the same algorithm. This means that the phase provided by aliased algorithms differ only by a constant.

A proper selection of this coefficient brings certain advantages, such as grouping intensities in pairs, thus simplifying its software implementation. This can be assured if the coefficients possess a Hermitian symmetry [8], which can be accomplished if

$$c_0 = \gamma^* \quad (3.16)$$

where the $*$ denotes complex conjugation.

To analyze the difference between two aliased versions of the same algorithm, the argument of the harmonic $S_1(\varphi)$ can be found as follows

$$\eta \cdot S_1(\varphi) = \eta \cdot \alpha_1 \cdot e^{i\varphi} \cdot P\left(e^{i\delta}\right) \quad (3.17)$$

$$\arg(\eta \cdot S_1(\varphi)) = \varphi' = \arg(\eta) + \arg(\alpha_1) + \underbrace{\arg\left(e^{i\varphi}\right)}_{\varphi} + \arg\left(P\left(e^{i\delta}\right)\right)$$

$$\varphi' = \underbrace{\arg(\eta) + \arg(\alpha_1) + \arg\left(P\left(e^{i\delta}\right)\right)}_{\text{phase offset}} + \varphi \quad (3.18)$$

where φ' is the phase estimated by the corresponding aliased version of the algorithm. The difference between aliased versions of the same algorithm is given in equation 3.18 by the complex constant η .

It is evident from equation 3.18 that the difference between the phases estimated by aliased versions of the same algorithm will be given only by the contributions of η and $P\left(e^{i\delta}\right)$.

Equation 3.18 shows the calculated phase φ' still differs from the real phase φ by the argument of α_1 . The parameter α represents only the phase origin and depends on the first sample taken on the wave. If the first sample is taken at a bright fringe (maximum intensity), the sampled signal will be treated by the Fourier Transform as proportional to the cosine of φ . This implies that α is real positive resulting to $\arg(\alpha) = 0$. If the half of the amplitude is taken as first intensity sample $\alpha \propto \sin(\varphi)$, this connotes that $\arg(\alpha) = \frac{\pi}{2}$. This fact only shows that the algorithm introduces an offset to the calculated phase depending on when the sampling procedure begins.

3.1.1 Miscalibrations

A phase estimation algorithm can also be designed to minimize some types of errors introduced by miscalibrations in the measurement such as variations in the sampling frequency or amplitude drifts.

Errors introduced by a linear misadjustment of the sampling frequency [8] correspond to a miscalibration of the phase shift given by

$$\delta' = \delta \cdot (1 + \epsilon) \quad (3.19)$$

The first-order variation of $P(e^{i \cdot n \delta'})$ produced by this miscalibration of the phase shift can be obtained by taking its first derivative with respect to δ

$$\frac{dP(e^{i \cdot n \delta})}{d\delta} = i \cdot n \cdot \delta \cdot \epsilon \cdot \mathbf{D}P(e^{i \cdot n \delta}) \quad (3.20)$$

where \mathbf{D} is an operator defined by

$$\mathbf{D}P(x) = x \frac{dP(x)}{dx} \quad (3.21)$$

If the algorithm has to be insensitive to this type of miscalibrations up to the first order of ϵ for the n -th harmonic, it is necessary that $\mathbf{D}P(x) = 0$ for $x \neq 0$. This means that $e^{i \cdot n \delta}$ has to be a double root of $P(x)$.

This criterium can be generalized up to the order m in ϵ for the n -th harmonic by iterating equation 3.20. This only increases the order of the root $e^{i \cdot n \delta}$ in $P(x)$ by m : $P(x) \propto (x - e^{i \cdot n \delta})^{m+1}$.

Another example is given by linear variations of the DC component of the interference pattern (order $n = 0$ of $S(\varphi)$) that could affect the intensity samples I_k (amplitude drift). Such a modulation can be considered by a characteristic polynomial $P(x)$ as $\frac{d^m P(x)}{dx^m} |_{x=1} \neq 0$, for $x = (e^{i \cdot \delta})^0 = 1$. According to equation 3.12, this will introduce supplementary error terms in $P(x)$ given by

$$\frac{d^m P(x)}{dx^m} |_{x=1} = \sum_{k=0}^{M-1} c_k \cdot \prod_{r=0}^{m-1} (k - r) \quad (3.22)$$

In order to eliminate these terms up to the order m , it is necessary that $\frac{d^m P(x)}{dx^m} |_{x=1} = 0$. This requires an increment by m in the order of the root $x = 1$, which means $P(x) \propto (x - 1)^{m+1}$.

More information about these and other possible corrections that can be taken into account by designing a phase estimation algorithm can be found in [8].

3.2 Application of the Algorithms

The simplest example of a phase estimation by applying the CP method as explained before can be given by the 3-point algorithm with a phase shift $\delta = \frac{\pi}{2}$. Hereby, the components $S_n(\varphi)$ to be eliminated are $n = 0$ and $n = -1$, the rest will be ignored. For this reason, the vector Ω is given by $\Omega = \{0, -1\}$.

In this case, the interference pattern must be sampled 3 times, each sample being equally spaced in the phase from its immediate neighbors by $\frac{\pi}{2}$, as shown in figure 3.1.

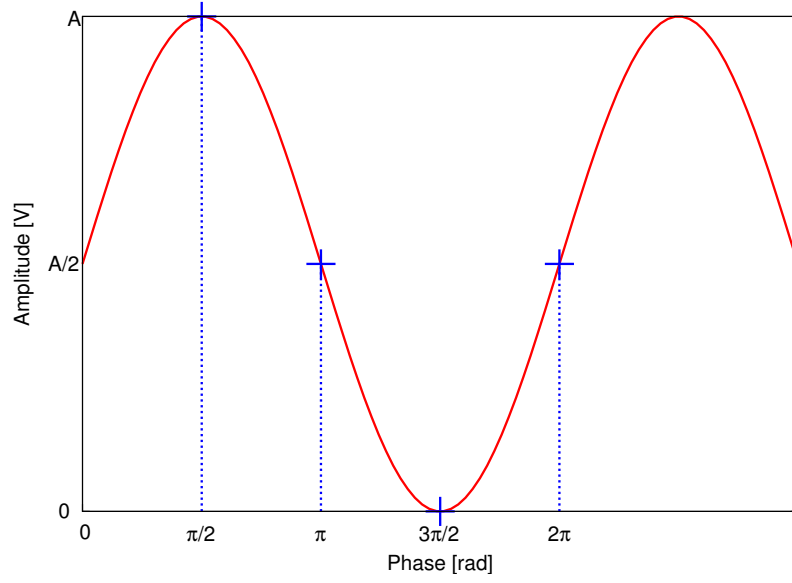


Figure 3.1: Representation of the sampling procedure by a phase shift of $\frac{\pi}{2}$ starting at a bright fringe

The CP for this algorithm, following equation 3.14, can be written as

$$\begin{aligned}
 P_1(x) &= \gamma_1 \cdot \left(x - \left(e^{i \cdot \frac{\pi}{2}}\right)^0\right) \cdot \left(x - \left(e^{i \cdot \frac{\pi}{2}}\right)^{-1}\right) \\
 &= \gamma_1 \cdot (x - 1)(x + i) \\
 &= \gamma_1 \cdot (x^2 + (i - 1) \cdot x - i)
 \end{aligned} \tag{3.23}$$

The coefficient γ_1 will be chosen according to the criterion in equation 3.16, yielding

$$\begin{aligned}
 c_0 &= -i = \gamma_1^* \\
 \gamma_1 &= i
 \end{aligned} \tag{3.24}$$

Substituting this value into equation 3.23 gives the following expression for $P_1(x)$

$$P_1(x) = i \cdot x^2 + (-1 - i) \cdot x + 1 \tag{3.25}$$

From the coefficients c_k of the polynomial $P_1(x)$, and following the expression given by equation 3.4, the parameters a_k and b_k are given by

$$\begin{aligned}
 a_{0,1,2} &= \{1, -1, 0\} \\
 b_{0,1,2} &= \{0, -1, 1\}
 \end{aligned} \tag{3.26}$$

Hence, the phase φ is computed from 3 intensity samples as

$$\varphi = \arctan\left(\frac{I_2 - I_1}{I_0 - I_1}\right) \tag{3.27}$$

Applied to the test signal of figure 3.1, this yields

$$\varphi = \arctan\left(\frac{0 - \frac{A}{2}}{\frac{A}{2} - 0}\right) = -\frac{\pi}{4} \text{ rad} \quad (3.28)$$

Note that for all practical implementations, the 4-quadrant arcustangens function must be used, e.g. `atan2(x,y)` in the C programming language.

At this point, it is interesting to analyze the phase contribution of the polynomial $P_1(x)$ to the calculated phase φ' . The argument of $P_1(x)$ for $x = e^{i\delta} = e^{i\frac{\pi}{2}} = i$ must be taken, because this is the contribution of the first order $n = 1$.

$$P_1(i) = i \cdot i^2 + (-1 - i) \cdot i + 1 = 2 \cdot (1 - i) \quad (3.29)$$

$$\arg(P_1(i)) = \arg(2 \cdot (1 - i)) = -\frac{\pi}{4} \quad (3.30)$$

This result shows that the relation between the calculated phase φ' and the real phase φ is

$$\varphi' = \varphi - \frac{\pi}{4} \quad (3.31)$$

Only the polynomial $P_1(x)$ makes a contribution, in this case, to the estimated phase, since the phase origin α was taken at a bright fringe, as shown in figure 3.1, and η was not considered for this algorithm, which means $\eta = 1$.

It could be expected, depending on the application, that the algorithm delivers a result that fulfills the relation $\varphi' = \varphi$. This can be achieved by a proper design of an aliased version of this algorithm, selecting a suitable value for η in equation 3.18.

In the specific case of the 3-point algorithm presented in equation 3.25, it is necessary to find a new characteristic polynomial $P_2(x) = \eta \cdot P_1(x)$ that cancels the phase contribution of $-\frac{\pi}{4}$ introduced by $P_1(x)$. Obviously, this means that the factor η has to make a contribution to the calculated phase of exactly $+\frac{\pi}{4}$, and demands that $\arg(\eta) = \frac{\pi}{4}$. The simplest expression for η fulfilling this condition would be $\eta = 1 + i$. Hence, the new characteristic polynomial $P_2(x)$ reads

$$\begin{aligned} P_2(x) &= \eta \cdot P_1(x) = (1 + i) \cdot (i \cdot x^2 + (-1 - i) \cdot x + 1) \\ P_2(x) &= (-1 + i) \cdot x^2 - 2i \cdot x + (1 + i) \end{aligned} \quad (3.32)$$

To be sure this algorithm accomplishes its aim, the verification from equation 3.30 can be applied to $P_2(x)$

$$\begin{aligned} P_2(i) &= (-1 + i) \cdot i^2 - 2i \cdot i + (1 + i) = 4 \\ \arg(P_2(i)) &= \arg(4) = 0 \end{aligned} \quad (3.33)$$

showing that $\varphi' = \varphi$.

The coefficients a_k and b_k of this aliased version of the 3-point algorithm can be identified from equation 3.32

$$\begin{aligned} a_{0,1,2} &= \{1, 0, -1\} \\ b_{0,1,2} &= \{1, -2, 1\} \end{aligned} \quad (3.34)$$

Thus, the phase φ can be computed from 3 intensity samples by this algorithm as

$$\varphi = \arctan \left(\frac{I_0 - 2 \cdot I_1 + I_2}{I_0 - I_2} \right) \quad (3.35)$$

For the test signal of figure 3.1, this yields

$$\varphi = \arctan \left(\frac{A - 2 \frac{A}{2} + 0}{A - 0} \right) = 0 \text{ rad} \quad (3.36)$$

This result can be verified by applying the 4-point algorithm presented in [9] with a phase shift $\delta = \frac{\pi}{2}$ to the same case. The coefficients a_k and b_k for this algorithms can be obtained from equation 3.16

$$\begin{aligned} a_{0,1,2,3} &= \{1, 0, -1, 0\} \\ b_{0,1,2,3} &= \{0, -1, 0, 1\} \end{aligned} \quad (3.37)$$

This algorithm fulfills the condition $\varphi' = \varphi$ as well. From these coefficients, the characteristic polynomial $P_3(x)$ corresponding to this algorithm can be reconstructed as

$$P_3(x) = 1 - i \cdot x - x^2 + i \cdot x^3 \quad (3.38)$$

In order to determine which harmonics must be suppressed by this algorithm, the characteristic polynomial $P_3(x)$ can be factored as follows

$$P_3(x) = (x - 1) \cdot (x + i) \cdot (x + 1) \quad (3.39)$$

Since the phase shift is given and equals $\frac{\pi}{2}$, the polynomial $P_3(x)$ can be also expressed as

$$P_3(x) = \underbrace{\left(x - \left(e^{i \cdot \frac{\pi}{2}} \right)^0 \right)}_{x-1} \cdot \underbrace{\left(x - \left(e^{i \cdot \frac{\pi}{2}} \right)^{-1} \right)}_{x+i} \cdot \underbrace{\left(x - \left(e^{i \cdot \frac{\pi}{2}} \right)^{\pm 2} \right)}_{x+1} \quad (3.40)$$

From this results, and recalling equations 3.14 and 3.15, the vector Ω is given by

$$\Omega = \{0, -1, 2, -2\} \quad (3.41)$$

which implies that the harmonics suppressed by this algorithm are $S_0(\varphi)$, $S_{-1}(\varphi)$ and $S_2(\varphi)$.

The phase φ can be estimated by this algorithm as

$$\varphi = \arctan \left(\frac{I_3 - I_1}{I_0 - I_2} \right) \quad (3.42)$$

The application of this algorithm to the test signal in figure 3.1 yields consequently

$$\varphi = \arctan \left(\frac{\frac{A}{2} - \frac{A}{2}}{A - 0} \right) = 0 \text{ rad} \quad (3.43)$$

and complies with the result obtained in equation 3.36.

3.3 Measurement Outlook

In the previous sections, a theoretical approach to estimate the phase of a signal was discussed. The actual application of this method will be explained with regard to measuring a phase front.

The interference pattern will be sampled M times using a CCD camera to obtain the intensities I_k for each pixel. A predefined and well controlled phase shift $k \cdot \delta$ must be applied to each measurement. Furthermore, an algorithm similar to that which has been described in this chapter can be applied over these samples, in order to estimate a value for the phase at each pixel. The output produced by this procedure will be a measurement of the spatial distribution of the phase front.

Different estimation algorithms were implemented in this experiment. One is the above mentioned 4-point algorithm presented in equation 3.42.

Another one is the 7-point WDFT introduced by [8]

$$\varphi = \arctan \left(\frac{(I_0 - I_6) - 3 \cdot (I_2 - I_4)}{2 \cdot (I_1 + I_5) - 4I_3} \right) \quad (3.44)$$

The corresponding characteristic polynomial for this algorithm is given by

$$\begin{aligned} P(x) &= -i \cdot \left(x - \left(e^{i \frac{\pi}{2}} \right)^0 \right)^2 \cdot \left(x - \left(e^{i \frac{\pi}{2}} \right)^{-1} \right)^2 \cdot \left(x - \left(e^{i \frac{\pi}{2}} \right)^{\pm 2} \right)^2 \\ &= -i \cdot (x - 1)^2 \cdot (x + i)^2 \cdot (x + 1)^2 \\ &= i + 2 \cdot x - 3i \cdot x^2 - 4 \cdot x^3 + 3i \cdot x^4 + 2 \cdot x^5 - i \cdot x^6 \end{aligned} \quad (3.45)$$

It can be seen from equation 3.45, that this algorithm suppresses the harmonics $S_n(\varphi)$ of order 0, -1, 2, and -2. In addition to this, it also corrects first-order variations of the DC component and first-order miscalibrations of the sampling frequency at the harmonics -1 and ± 2 .

The 9-point algorithm¹

$$\varphi = \arctan \left(\frac{4 \cdot (I_7 - I_1) + 12 \cdot (I_3 - I_5)}{I_0 - 8 \cdot (I_2 + I_6) + 14 \cdot I_4 + I_8} \right) \quad (3.46)$$

whose characteristic polynomial is given by

$$\begin{aligned} P(x) &= \left(x - \left(e^{i \frac{\pi}{2}} \right)^0 \right)^2 \cdot \left(x - \left(e^{i \frac{\pi}{2}} \right)^{-1} \right)^4 \cdot \left(x - \left(e^{i \frac{\pi}{2}} \right)^{\pm 2} \right)^2 \\ &= (x - 1)^2 \cdot (x + i)^4 \cdot (x + 1)^2 \\ &= 1 - 4ix - 8x^2 + 12ix^3 + 14x^4 - ix^5 - 8x^6 + 4ix^7 + x^8 \end{aligned} \quad (3.47)$$

suppresses the harmonics of orders 0, -1, 2, and -2, also considering first-order variations of the DC component, as well as first and third-order misadjustments of the sampling frequency at the harmonics ± 2 and -1 respectively.

The 13-point algorithm² suppresses the harmonics 0, -1, 2, and -2 and corrects

¹Yves Surrel [Private Communication]

²Gerhard Heinzel [Private Communication]

third-order amplitude variations (DC misadjustments) and frequency miscalibrations for the harmonics -1, 2, and -2 up to the third order. This algorithm corresponds to

$$\varphi = \arctan \left(\frac{4 \cdot (I_{11} - I_1) + 20 \cdot (I_3 - I_9) + 40 \cdot (I_7 - I_5)}{I_0 - 10 \cdot (I_2 + I_{10}) + 31 \cdot (I_4 + I_8) - 44 \cdot I_6 + I_{12}} \right) \quad (3.48)$$

The characteristic polynomial for this algorithm is given by

$$\begin{aligned} P(x) &= \left(x - \left(e^{i \cdot \frac{\pi}{2}} \right)^0 \right)^4 \cdot \left(x - \left(e^{i \cdot \frac{\pi}{2}} \right)^{-1} \right)^4 \cdot \left(x - \left(e^{i \cdot \frac{\pi}{2}} \right)^{\pm 2} \right)^4 \\ &= (x - 1)^4 \cdot (x + i)^4 \cdot (x + 1)^4 \end{aligned} \quad (3.49)$$

All these algorithms require a phase shift $\delta = \frac{\pi}{2}$.

4 Experimental Approach

This chapter presents some experimental components that are necessary to realize the measurement introduced in section 3.3.

4.1 Requirements

In order to perform a useful measurement of the phase front which allows a proper adjustment of the optics on the interferometer, the following aspects must be taken into account:

1. The frames should correspond to point-like intensity samples to determine a significant structure of the spatial distribution of the phase front. This means that the integration time of the spatially resolving photodetector should be as short as possible. Each exposure is required, in this application, to be no greater than $\frac{1}{40}$ times of the heterodyne period T_{het} . This sets the integration time to $\frac{1}{40} \cdot 616 \mu s \approx 15 \mu s$ for a heterodyne frequency of 1623 Hz.
2. The frames have to be captured such that a phase difference of $\frac{\pi}{2}$ separates consecutive exposures in the phase (phase shift δ). This corresponds to a delay of $\frac{T_{het}}{4} \Rightarrow \frac{616 \mu s}{4} \approx 154 \mu s$ between the samples. It turns out that such short delays are impossible to achieve. Instead, equivalent delays of $n \cdot T_{het} + k \cdot T_{het}$ with integers n and k are realized.
3. The camera must reach a frame rate high enough to enable a real-time processing and display of the data, at least 2 phase fronts per second. This is a very important requirement, in order to enable a proper adjustment of the optics on the interferometer to achieve a homogeneous phase front.

4.2 Spatially Resolving Photodetectors

A description of the characteristics of the photodetectors considered in this thesis is given in the following subsections.

4.2.1 Silicon Charge-Coupled Device (CCD) Camera

A CCD camera consists of thousands of small photodiodes, known as pixels, arranged in a rectangular array. Each pixel integrates a different section of the spatial distribution of the incoming light source, thus providing an image. The incoming photons which penetrate into a photocell (pixel) excite the electrons in the valence band of the semiconductor material. These photons supply the necessary energy for the transition of these electrons into the conduction

band. This effect is known as internal photoeffect.

The number of electrons transferred from the valence band into the conduction band is proportional to the number of photons captured by the photocell during an exposure. This means that a pixel holds an average of the charge accumulated in the conduction band over the time this pixel was set in a "capture mode".

Naturally, the internal photoeffect will take place as long as the photocell is exposed to the light source. It can, however, be controlled electronically if the information (electrons in the conduction band) should be kept in the register or not, as well as how long this capture mode should take. This time is known as integration time or exposure time.

Commercial CCD devices typically offer two types of capture modes. One of them, known as "free-mode", operates by acquiring one line of pixels while another line is still integrating. The information detected by different pixels is, therefore, captured at different moments.

The second operational mode of a CCD camera is known as "global shutter". This mode triggers the capture operation for all pixels, of equal duration for all pixels, at the same time. This way, no temporal shifting between the samples measured by different pixels can take place.

The operation of the CCD device in the latter "global shutter" capture mode is mandatory to perform the measurement aimed by this thesis.

The registers of each cell are read out sequentially, line by line, and the charge accumulated is converted into a proportional analog voltage level. These voltages are digitized by an Analog/Digital converter (ADC).

The lines are sequentially shifted through the array until they reach the bottom line, where each line is then shifted in the orthogonal direction to the single ADC. This linewise shifting through the array causes the "blooming" effect which takes place if light is still present after the exposure has finished.

Afterwards, these signals are multiplexed to be transferred through a conventional interface like USB, Firewire, PCI, among others, to a computer for further processing of the data. Figure 4.1 shows the schematic working procedure of a CCD camera.

The CCD camera used in the experimental setup described in section 5.1.1 is the WinCamD from the company DataRay.

This camera achieves to capture reliably 3-4 frames per second by external triggering at its maximum resolution. The minimum exposure time for this camera is $16 \mu s$.

The frames can only be obtained from the camera for further processing through the provided software delivered by DataRay, which operates only on Microsoft Windows platform.

According to the specifications given by the manufacturer, the sensitivity of the camera covers the spectral range between approximately 300 nm to 1100 nm wavelength. Figure 4.2 presents the quantum efficiency of a typical silicon CCD camera. The WinCamD camera is too slow to sample the interference pattern as expected in the measurement. The limitations presented by its software hinder further processing that would enable an on-line measurement of the phase front. Its low quantum efficiency with a 1064 nm Nd:YAG laser, provides difficulties with the blooming effect which are commented in detail in section 5.1.1.

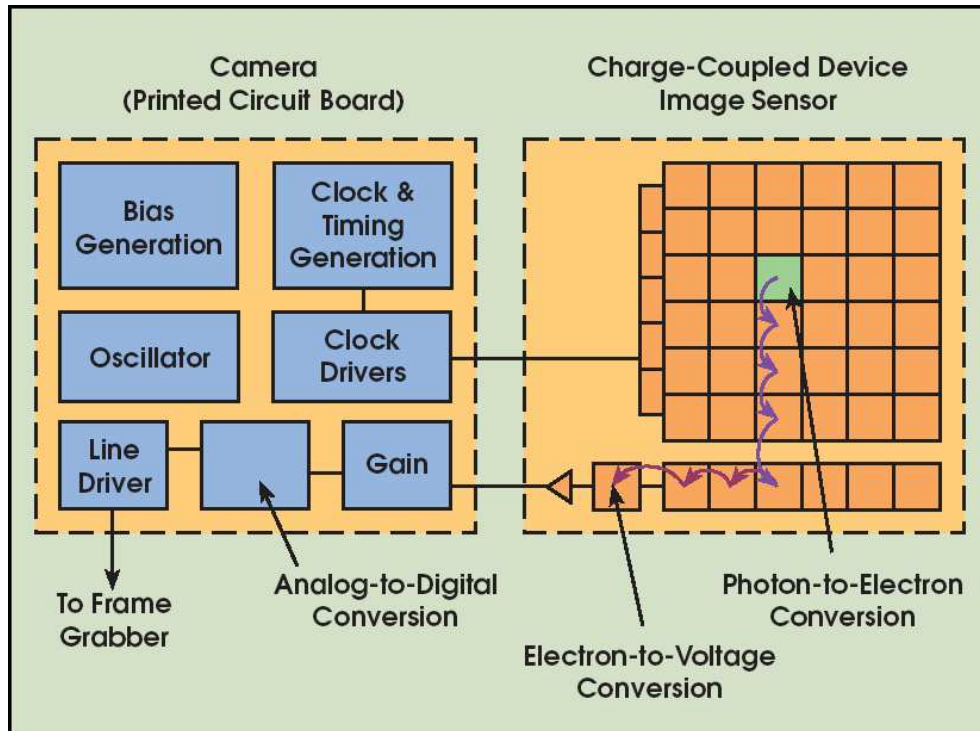


Figure 4.1: Diagram of the functional procedure of a CCD camera [10]

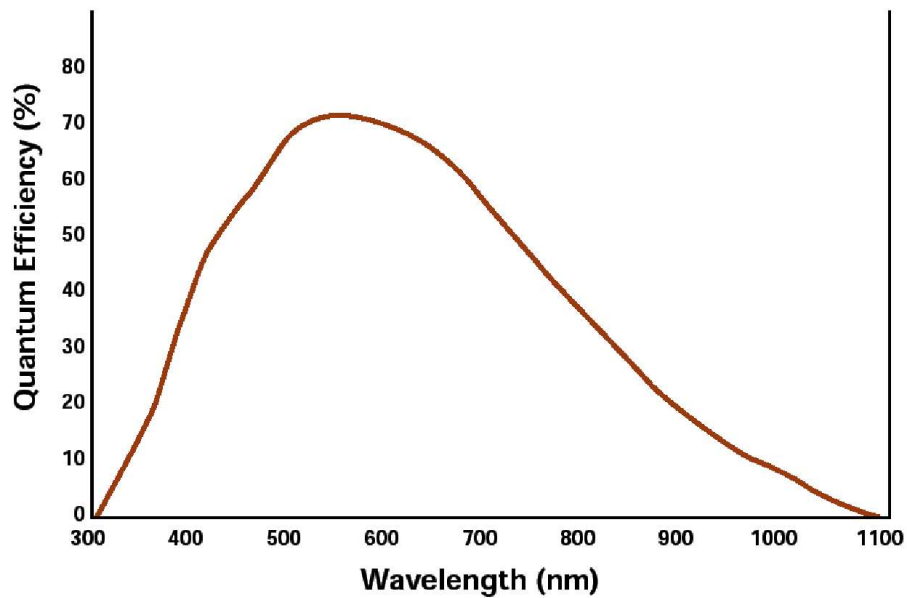


Figure 4.2: Quantum Efficiency for a typical CCD photodetector

Nevertheless, an experiment to measure the phase front with this camera was performed in order to analyze the viability of the experiment, and to support the intention of developing a tool to perform this measurement in real-time with concrete results.

4.2.2 Silicon Complementary Metal Oxide Semiconductor (CMOS) Camera

A different type of spatially resolving photodetectors is the CMOS camera. The most important difference between these devices and the CCDs is the extra circuitry below each photocell as shown in figure 4.3.

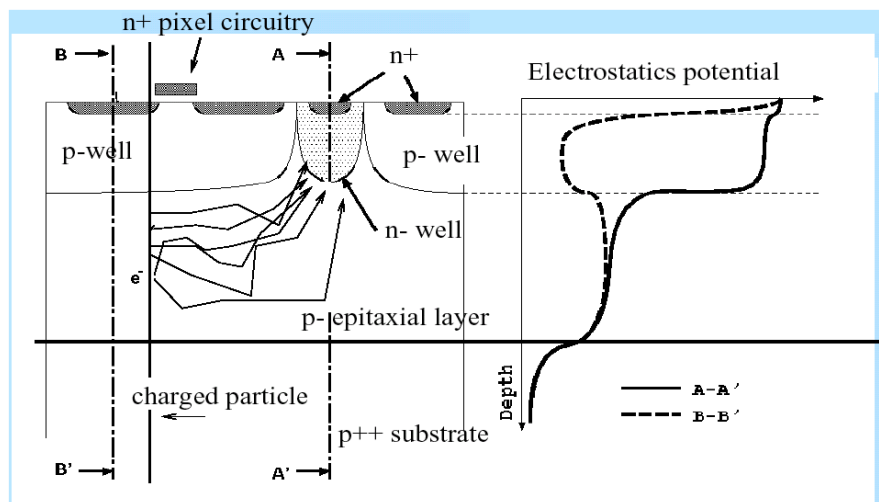


Figure 4.3: Diagram of a pixel of a CMOS imaging sensor[11]

These additional electronics are responsible for the conversion of the charge accumulated in the conduction band, due to the captured photons, into a voltage level. Hence, an overflow of electrons into the neighbor cells cannot take place by overexposing the device. This means that these cameras are not affected by the blooming effect. Figure 4.4 shows the functional diagram of a CMOS camera.

However, the photodetector in these cameras is made of silicon as well. Therefore, the quantum efficiency at the Nd:YAG laser wavelength (1064 nm) is as low as with CCDs, approximately 3%. Figure 4.5 shows the quantum efficiency of a CMOS camera distributed by the company PCO Imaging¹.

The problem with these cameras is that the material is almost "transparent" for the wavelength used. Because 97% of the laser power is going through the photocells, the circuitry below the pixels, which controls the electron-voltage conversion, is being exposed to this moderate power radiation. This disturbs the electronics and leads to decreased performance or even malfunction.

For this particular reason, the silicon CMOS camera was excluded from the

¹Information provided within the frame of a possible sale to AEI Hanover

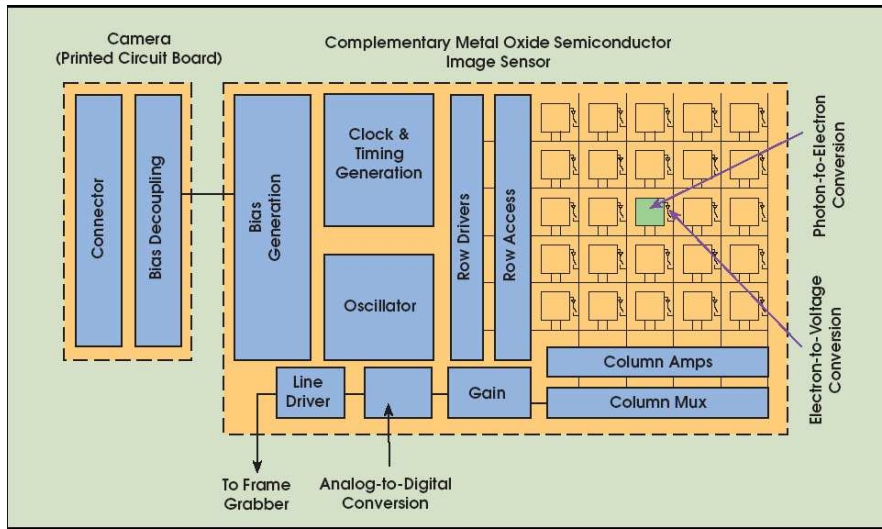


Figure 4.4: Diagram of the functional procedure of a CMOS camera [10]

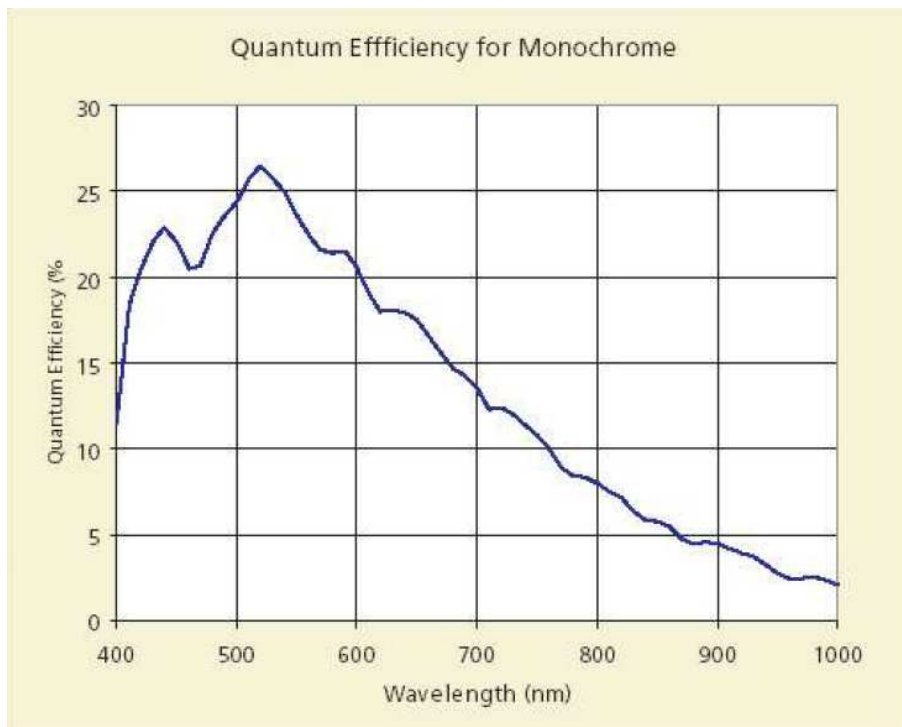


Figure 4.5: Quantum Efficiency for the Micron MT9M413 CMOS photodetector distributed with the pco.1200hs camera from PCO Imaging

application.

4.2.3 Indium-Gallium-Arsenide (InGaAs) CCD Camera

Indium-gallium-arsenide (InGaAs) is a semiconductor material that has a high quantum efficiency in the near-infrared.

The camera XEVA-USB provided by XenICs is a CCD device, whose photodetector is made of InGaAs. Figure 4.6 shows the quantum efficiency of the XFPA photodetector inside the XEVA-USB.

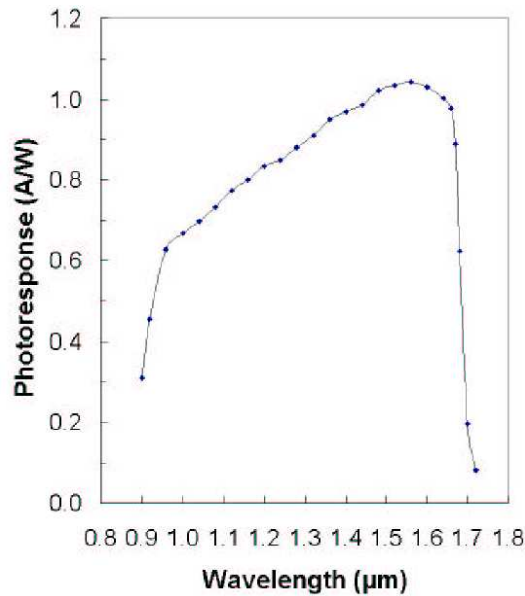


Figure 4.6: Quantum Efficiency for the InGaAs CCD photodetector FPA distributed by XenICs

It can be seen from this curve that for a wavelength of 1064nm, the quantum efficiency of this device is approximately 80 %, much better than any camera based on a silicon chip.

According to the data sheets and to the tests performed on this device, the shortest integration time settable is $1 \mu\text{s}$. This value corresponds to $\frac{1}{616}$ times (approximately 0.16 %) the oscillation period. For this reason, it is possible to perform a very precise sampling of the interference pattern.

The camera is also able to acquire 30 frames per second. The software, driver and libraries enable the user to program their own software to control the camera.

This fact allows an on-line processing of the data and simplifies the implementation of a real-time measurement and display of the phase front.

The Linux driver for this camera makes possible to implement an application based on an X-windows system platform. It is for these reasons that this device was chosen to perform the sampling of the interference pattern. This camera simplified the development of a state-of-the-art measuring apparatus capable

to acquire the phase front in real-time.

The experimental setup designed to measure the phase front with this camera is presented in section 5.2.1.

4.3 Measurement Procedure

The experimental setup and measurement procedure designed to measure the phase front with help of a spatially resolving photodetector are described in this section.

As explained in chapter 3, all the algorithms implemented for the phase estimation have a phase shift $\delta = \frac{\pi}{2}$. This means that a sample must be taken every $\frac{T_{\text{het}}}{4}$. As mentioned before, the heterodyne signal oscillates with a period of $616 \mu\text{s}$. This implies that the camera should be able to capture about 6500 frames per second. An investigation of the products available in the market showed that neither the devices mentioned before nor other types of cameras can achieve this frame rate with a sufficient spatial resolution and sensitivity at 1064 nm .

Therefore, the time delays between exposures are extended by an integer number of heterodyne periods: $\Delta t = \left(n + \frac{k}{4}\right) \cdot T_{\text{het}}$. Since the absolute timing of the heterodyne signal may fluctuate during this additional delay, it is necessary to find an additional trigger signal that tracks the overall interference phase with high fidelity. For this purpose, a single-element photodiode is placed at one output of the beamsplitter where the interference take place. This photodiode tracks the heterodyne signal and generates an electrical current such as the signal presented in figure 4.7

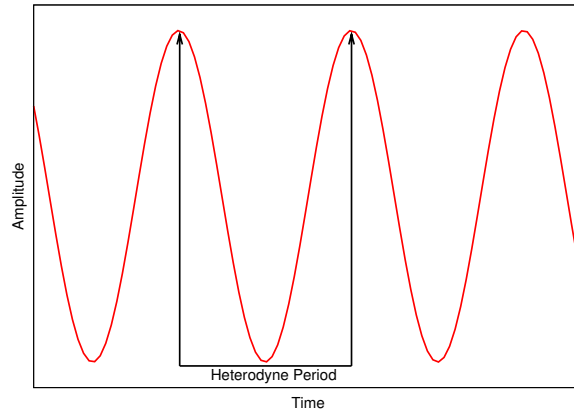


Figure 4.7: Electrical signal produced by a photodiode exposed to the interference beam

Through proper processing of this signal, it is possible to determine the momentary timing of the interference pattern. Together with the corresponding phase shift $k \cdot \delta$, for $k = \{0, 1, 2, \dots\}$, pulses can be generated to trigger the camera at

the right moment to acquire the frame k .

All this can be achieved easily by using a Field Programmable Gate Array (FPGA). It detects a reference point on the signal and sends the corresponding trigger pulse to the camera to capture the frame k with the required delay $k \cdot \delta$ relative to this reference point.

A FPGA is a digital chip consisting of thousands of logical gates, which can be connected as desired by loading the appropriate program onto the device.

The electrical signal generated by the photodiode must therefore be digitized before it can be processed by the FPGA.

Since this sinusoid cannot oscillate around a zero-voltage-level (there is no "negative" intensity to be detected by the photodiode) the DC component of the signal must be removed to center the wave around zero. This is necessary to make the signal cross through zero, and perform a clean digitization by using a simple comparator.

Every time the wave crosses through zero from negative to positive voltages, a rising edge will be generated by the comparator. Hence, the FPGA can detect this rising edge of the digitized heterodyne signal and use it as reference point on the wave.

In order to decouple the DC-component from the electrical signal generated by the photodiode, the signal must be filtered by a band-pass. The filter designed for this purpose is shown in figure 4.8 (see appendix A).

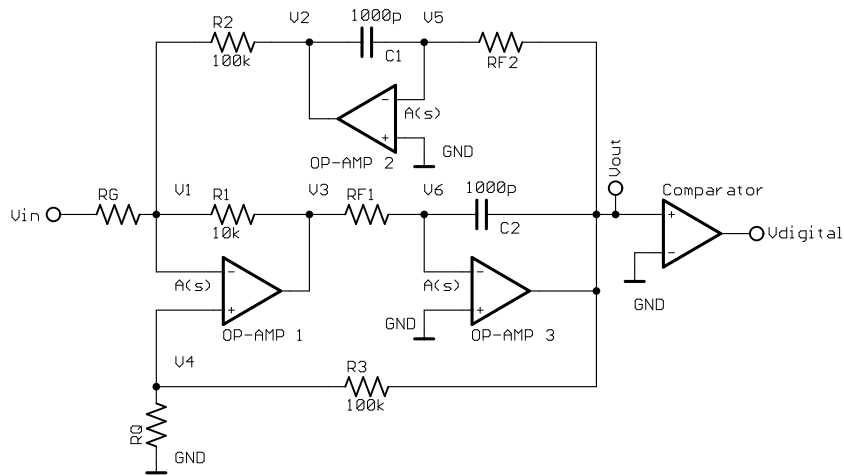


Figure 4.8: Topology used for the electronic circuit of the band-pass filter

The criteria for setting the values of the unknown resistors are [12]

$$\begin{aligned}
 R_F &= \frac{5.03 \cdot 10^7}{f} \Omega \\
 R_Q &= \frac{10^5}{3.48 \cdot Q - G - 1} \Omega \\
 R_G &= \frac{3.16 \cdot 10^4 \cdot Q}{G} \Omega
 \end{aligned} \tag{4.1}$$

where f is the center frequency, Q is the quality factor of the filter, and G is the gain. The special characteristic of this filter is that the center frequency can be changed easily with the resistor R_F without affecting the other factors. In this case, the frequency f would be set to approximately 1623 Hz, which is the heterodyne frequency. The gain G and the quality factor Q were chosen to be 1, since no extra gain is needed for the signal and the purpose of the filter is only to suppress the DC-component. From these parameters, the commercial values for the unknown resistances can be determined: $R_F = 30.1 \text{ k}\Omega$, $R_Q = 27.4 \text{ k}\Omega$ and $R_G = 30.1 \text{ k}\Omega$.

Hence, the measurement procedure till this point can be illustrated by figure 4.9

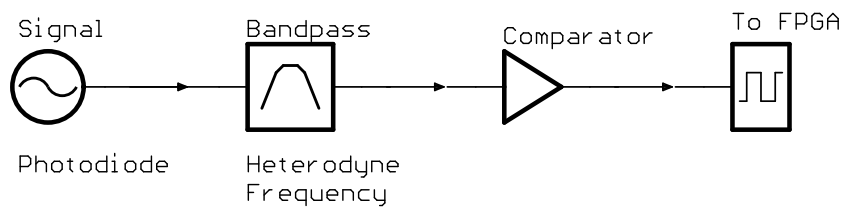


Figure 4.9: Block diagram of the electronics for digitizing the heterodyne signal

The configuration of the experimental setup for the measurement of the phase front is outlined in figure 4.10.

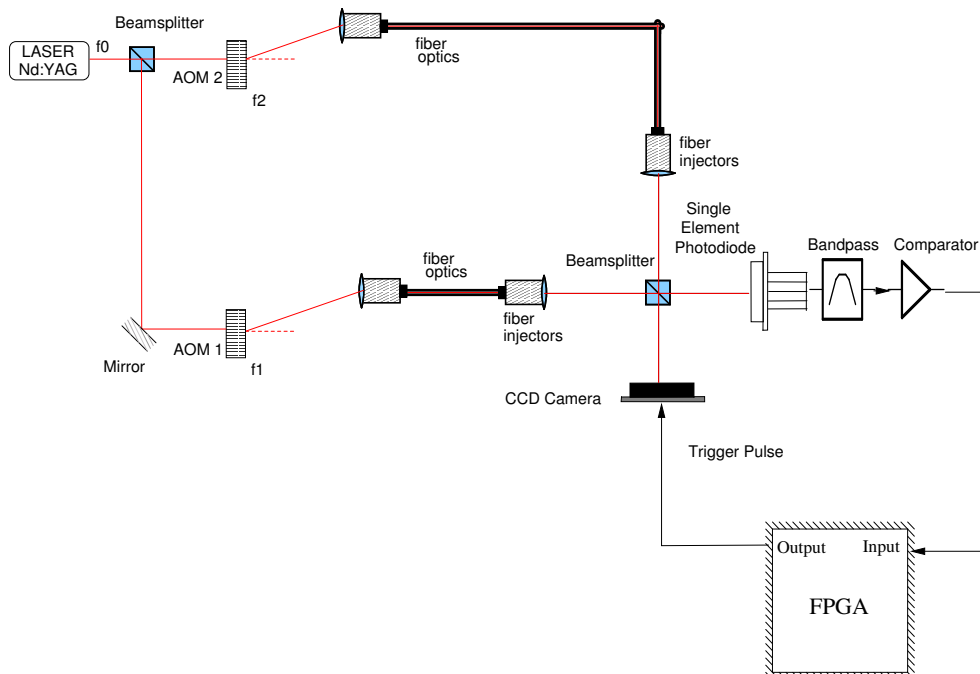


Figure 4.10: Interferometer configuration for the measurement of the phase front with a spatially resolving photodetector

The DC component of the signal measured by the photodiode is filtered by the band-pass. This signal is then digitized by the comparator and sent to the FPGA.

The FPGA detects a rising edge of the digitized heterodyne signal and sends immediately a trigger pulsed to the camera. After the camera has acquired the frame and is ready to capture the next one, the FPGA detects a rising edge again and sends a trigger pulse to the camera after $\frac{T_{\text{het}}}{4}$. This trigger pulse is delayed, since the exposures have to be separated by $\frac{\pi}{2}$ in the phase, which corresponds to $\frac{T_{\text{het}}}{4}$.

Therefore, the delay of the trigger pulse with respect to the rising edge detection to capture the frame k is $k \cdot \frac{T_{\text{het}}}{4}$.

This procedure must be performed M times to capture the necessary frames for applying a M -point algorithm to the intensities sampled at each pixel.

5 Phase Front Measurement

This chapter presents the configuration of the experimental setups designed for a successful phase front measurement with the WinCamD and with the XEVA USB cameras.

5.1 Phase Front Measurement with the WinCamD

5.1.1 Experimental Setup

The experimental setup presented in section 4.3 was reconfigured in order to use the WinCamD camera for the phase front measurement.

The main problem in performing this measurement with the WinCamD arose from the fact that this camera has a low sensitivity to the wavelength of the laser used (figure 4.2).

As a result, the camera could not see anything at the normal laser power during the minimum exposure time ($16\ \mu\text{s}$). For this reason, the power of the laser was increased for the camera to be able to take an exposure of the beam. The problem was that the camera was affected by the blooming effect, making the intensity samples useless for further processing. This occurs when the camera remains exposed to the light source while the lines are shifted through the array. The electrons generated due to the internal photoeffect flow into the neighboring cells adulterating the intensity information which is read out from the camera. Figure 5.1 presents an example of a frame taken by this camera with blooming.

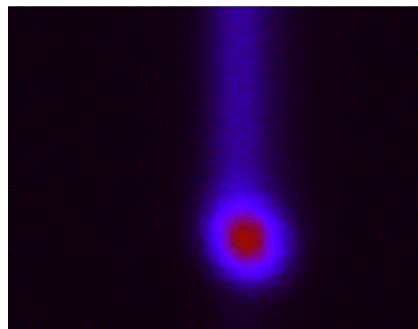


Figure 5.1: Frame captured by the WinCamD under the effects of blooming

In order to solve this problem, high frequency switches were designed to actuate on the laser. These switches control the actual light exposure of the camera. The switches regulate the power of the RF signals driving the AOMs (1-2 W)

and are operated such that the modulation of the laser can be turned ON and OFF for the time needed. This procedure was chosen to avoid an actuation on the main laser, since only the first diffraction order of the light modulated by the AOMs is used for the interference.

These RF switches are controlled by an extra signal generated by the FPGA. A time diagram describing the functional process of these signals and their dependency to the heterodyne signal is shown in figure 5.2.

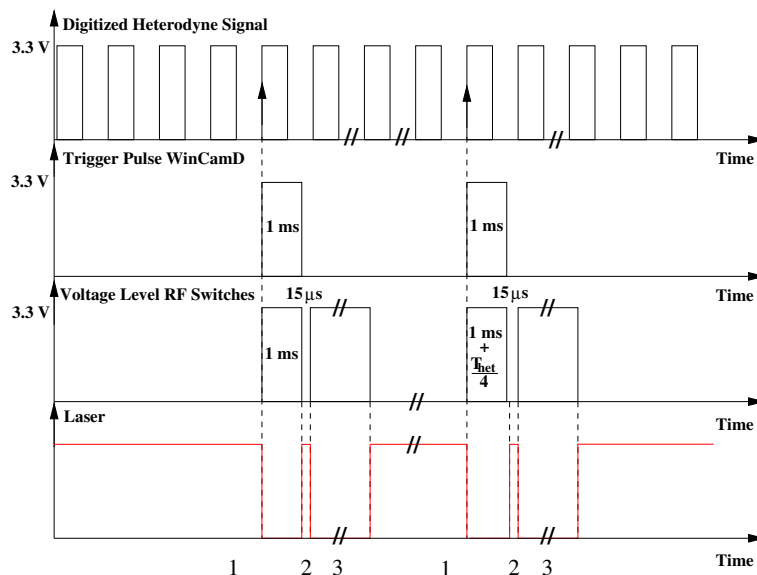


Figure 5.2: Diagram of the signals processed and sent by the FPGA

1. Laser is ON to allow settling of the bandpass filter and acquisition of phase with the single-element photodiode.
2. Exposure.
3. Laser is OFF to allow reading out the CCD camera without blooming.

The FPGA detects a rising edge of the digitized heterodyne signal and sends a trigger pulse to the WinCamD. At the same time a TTL voltage level (3.3 V) is set at the input of the RF switches to turn off the modulation of the beams. After 1 ms, which is the reaction time of the camera, the RF switches are set to LOW for exactly $15 \mu\text{s}$, which is the desired exposure time, and then back to HIGH to avoid the blooming. After a rising edge detection, the input of the RF switches remain HIGH for $1 \text{ ms} + k \cdot \frac{T_{\text{het}}}{4}$ to capture the frame k , in order to obtain frames which are shifted by $\frac{\pi}{2}$ in the phase. This procedure produces the M necessary exposures for a phase front estimation.

The program loaded onto the FPGA makes it work as a state machine in charge of tracking the heterodyne signal and controlling the instruments for the measurement of the phase front. The functional process of this state machine can be described by the flow diagram shown in figure 5.3.

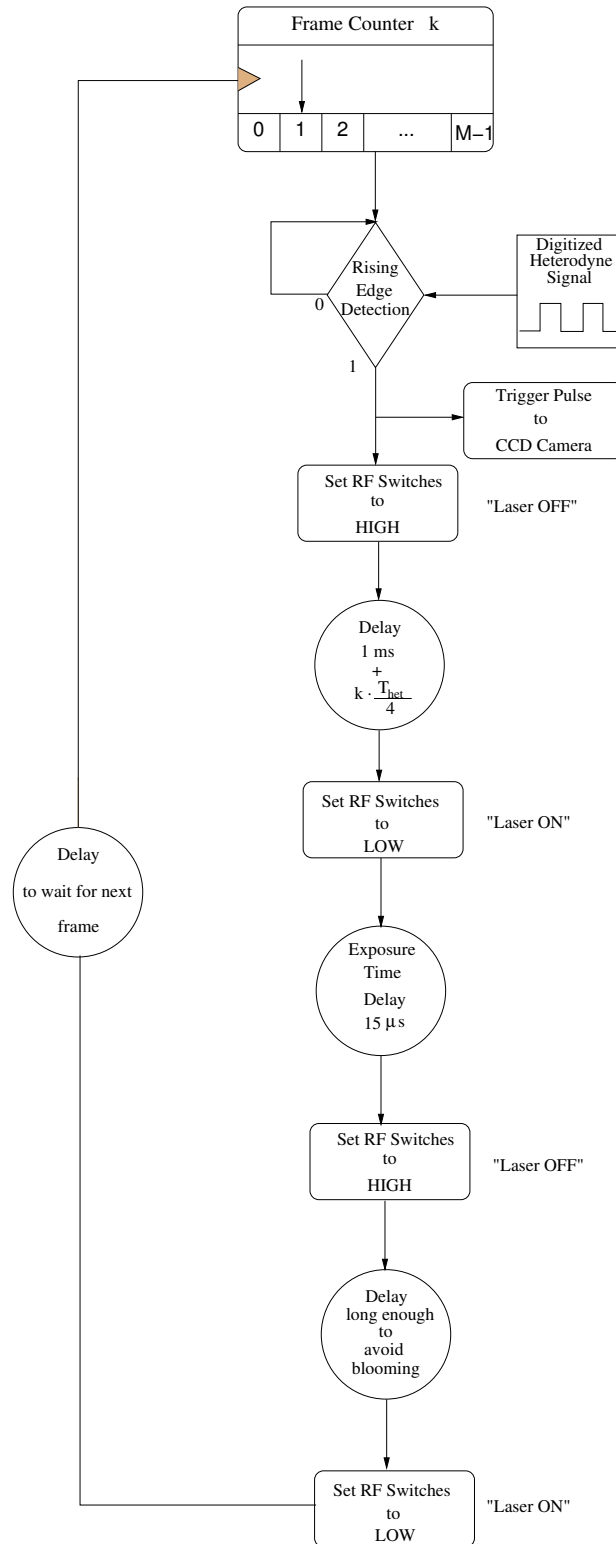


Figure 5.3: Flow diagram of the program loaded onto the FPGA for the phase front measurement with the WinCamD

Hence, the experimental configuration used to perform a phase front measurement with the silicon CCD camera WinCamD is outlined by figure 5.4.

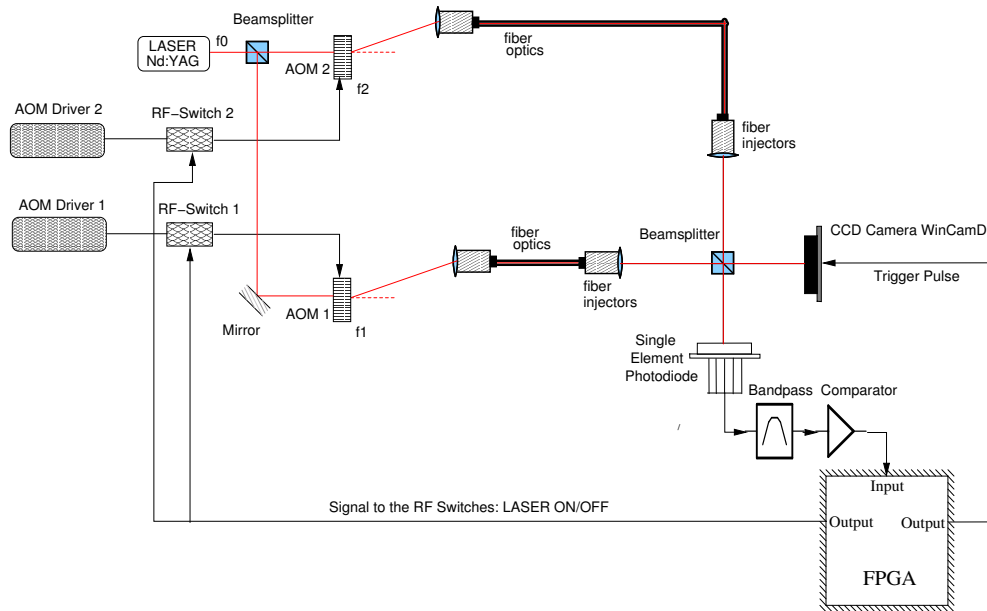


Figure 5.4: Illustration of the experimental setup used for the measurement of the phase front with the WinCamD

The FPGA monitors the digitized signal from the single-element photodiode and waits for a rising edge to proceed triggering the CCD camera and switching off the modulation at the AOMs by setting the input of the RF switches to HIGH. After 1 ms of the first rising edge detection, the FPGA sets the voltage to the RF switches to LOW for exactly $15 \mu\text{s}$, and then back to HIGH to avoid blooming, controlling hereby the exposure time needed for the intensities sampled.

The FPGA waits approximately 300 ms between each sampling procedure, since this camera takes only 3 frames per second.

This setup succeeded in measuring the phase front. Nevertheless, some parameters had to be changed in the interferometer for this camera to measure significant intensities. The exposure time had to be increased to $50 \mu\text{s}$, since the frames captured at $15 \mu\text{s}$ had very low intensity values, and were therefore strongly influenced by the background. In order to maintain the significance of the measured structure of the phase front, the heterodyne frequency was correspondingly decreased to 293 Hz. Hence, the resistance R_F in the filter of figure 4.8 was readjusted for the new heterodyne frequency to a value of $182 \text{ k}\Omega$. A representative measurement achieved by this setup is presented in the next section.

5.1.2 Results

Well-Aligned Interferometer

The measuring procedure described in the preceding section was used to analyze the structure of the phase front of a well-aligned interferometer. This interferometer was adjusted for optimal contrast and an ideal alignment of the beams. Figure 5.5 presents the results of this measurement.

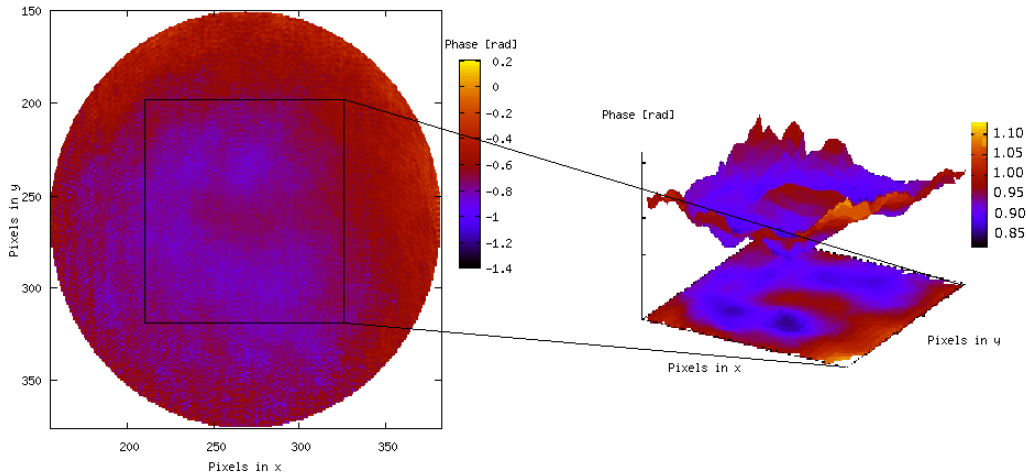


Figure 5.5: Phase front measured by the silicon CCD camera WinCamD at a well-adjusted interferometer

As shown in this image, the phase front varies by approximately ± 0.15 rad in the central region, and even more at the edges of the interference pattern. Considering the assumption made in section 2.5 and commented in [7], this inhomogeneity of the phase front, in conjunction with beam jitter and the finite insensitive slits in the quadrant photodiodes, is expected to generate errors in the phase measurement. This could explain the deteriorated performance in the measurement with quadrant photodiodes compared to the performance achieved by measuring with single element photodiodes, shown in figure 2.22. Additionally, figure 5.5 presents also a small protuberance in the center of the phase front of about 0.2 rad, which resembles the measurement made with a pin hole covering a single element photodiode, presented in figure 2.25, shown here once again in figure 5.6.

These two measurements are not really comparable, since the instrumentation and optical components used in both cases were different. Furthermore, the spatial resolution of the measurement performed with the WinCamD is much higher.

However, the most important conclusion that can be made from these results is that a homogeneous phase front is, as matter of fact, not often obtained without having to conduct an extra adjustment on the wave front of the beams to counteract the difference between their parameters.

To accomplish such an adjustment it is necessary to have a tool that allows the

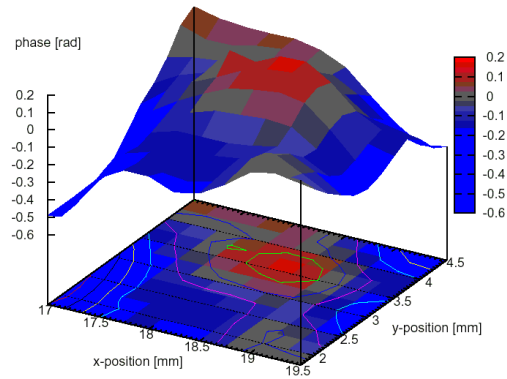


Figure 5.6: Phase front measured with a pin hole covering a single element photodiode using the phasemeter presented in section 2.4.3

measurement and display of the phase front in real time to follow continuously the changes of its structure and achieve a spatial homogenization. The development of this tool was the main purpose of this thesis and it is presented in the following section.

Different Beam Parameters

Another interesting result was obtained by recombining two beams, whose parameters were very different. In order to change the beam parameters of only one of the beams, a lens with a focal length of 500 mm was placed into one arm of the interferometer as shown in figure 5.7.

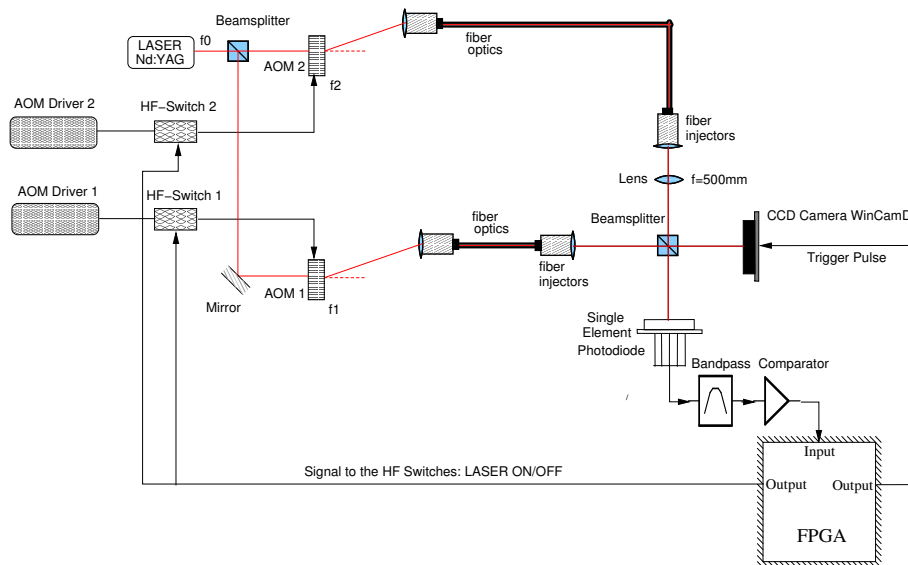


Figure 5.7: Setup for the measurement of the phase front with a lens of 500mm focal length on one arm of the interferometer using the WinCamD camera

The interferometer was adjusted to achieve a maximum contrast. Nevertheless, the contrast measured by the photodiode was approximately 5-10%. This is not surprising, since the interference by such beams is not optimal. The phase front measured in this case is shown in figure 5.8.

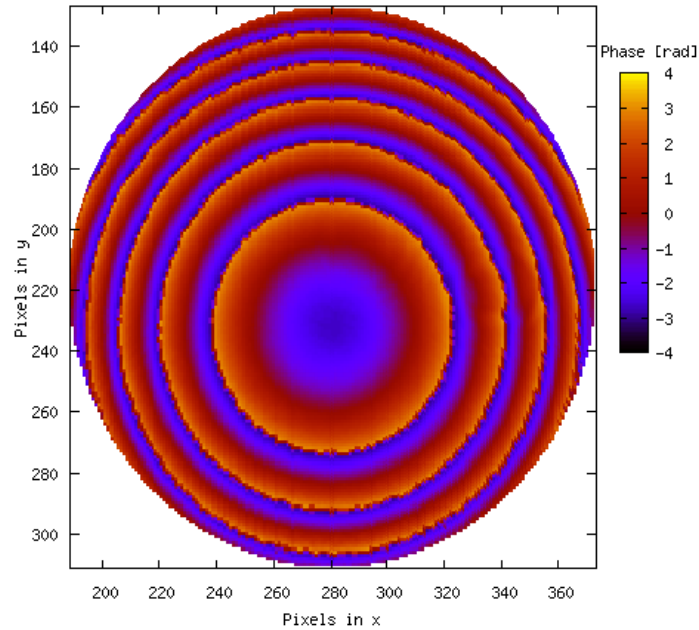


Figure 5.8: Measurement of the spatial phase distribution for very different beam parameters

It is clear in this case that the difference between the parameters of both beams is so strong that the phase varies abruptly many times between $-\pi$ rad and π rad within the area of interest.

These variations represent actually a constant increment of the phase, from a minimum value in the center, till a maximum of several times π . Since the estimation algorithms provide only values for the phase between $-\pi$ rad and π rad, the maximum magnitude for the phase presented in this image is π rad. In order to corroborate this experimental result, the beam parameters were measured and the interference was simulated¹ by software. The result obtained from this simulation is presented in figure 5.9.

On the other hand, the interference pattern also shows rings in the intensity, as presented in figure 5.10.

This effect can be explained by the large variations presented in the phase front

¹In collaboration with Vinzenz Wand

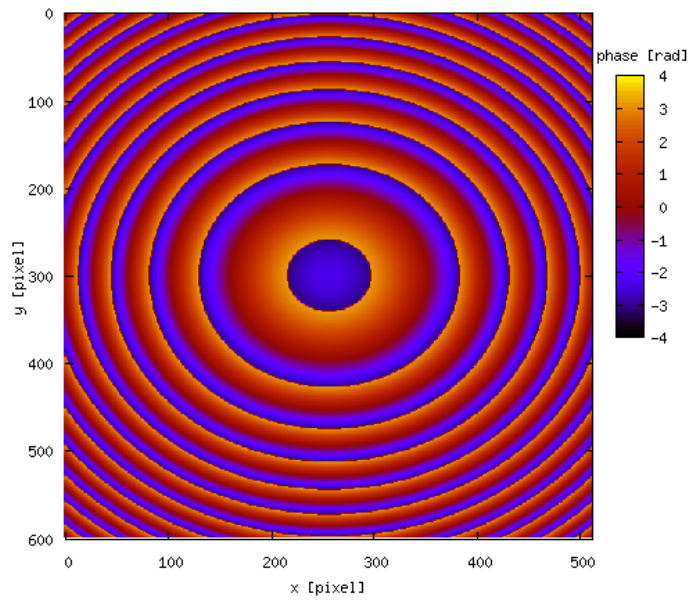


Figure 5.9: Phase front obtained by the simulation of the interference between beams using the beam parameters measured for the case in figure 5.8

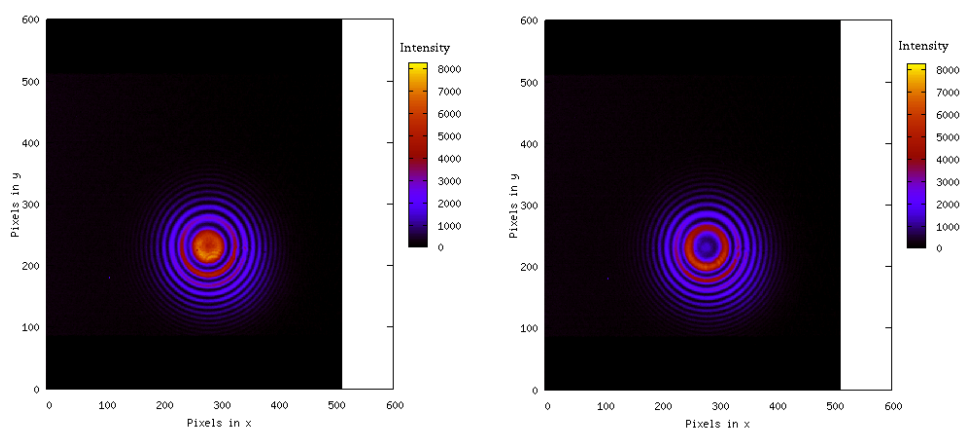


Figure 5.10: Interference pattern for the measurement of the phase front presented in figure 5.8

in figure 5.8. Whereas some regions in the beam reach a maximum of the intensity, others, due to a phase difference of π , reach a minimum. This also means that the position of these rings of minimum intensity do not remain constant over time, but move along the beam, as shown in the figure.

The time dependence of the variation of the rings confirms that their appearance is only due to the interference of the beams and not due to some aberration of the wave front that the lens might have caused, such as Newton's rings, since both beams separately showed a normal gaussian profile.

5.2 Phase Front Measurement with the XEVA USB

This section presents the measuring apparatus developed for this thesis to perform a real-time measurement of the phase front.

An on-line processing and display of the data is enabled by the software developed for this application together with the hardware utilized in the new experimental setup. The new configuration of the experimental setup is presented in the following section.

Section 5.2.2 presents the software developed for the analysis and display of the data and contains a description of each display programmed for the graphical user interface (GUI), within an explanation of how every quantity is calculated.

5.2.1 Experimental Setup

Contrary to the configuration designed for the silicon CCD camera, the experimental setup was simplified for this new application due to the better performance of the InGaAs camera XEVA USB.

As mentioned in section 4.2.3, this camera reaches a higher frame rate (30 fps) than the WinCamD and is able to acquire frames at very short exposure times and low laser power.

For this reason, it was possible to overcome the problem of the blooming effect presented in section 5.1.1.

The program written to run the FPGA was also improved and could be simplified. One simplification is the omission of the signal sent to the RF switches, because there is no need any more to switch the laser off.

Moreover, an interface was developed to control the FPGA through the parallel port of the computer. The software programmed for the analysis and display of the data contains also a routine that determines the delay $\tau = k \cdot \delta$ corresponding to the delay required for the frame k . This delay τ is transferred to the FPGA through the parallel port.

The counter and additional delays shown in figure 5.3 can be omitted, since the counting process is done by the software in the computer.

The new program of the FPGA can be described by figure 5.11. The experimental setup for the real-time measurement of the phase front is outlined by figure 5.12

The software sends a command to the FPGA which includes the delay $\tau = k \cdot \delta$ to capture the frame k . The FPGA detects a rising edge of the digitized heterodyne signal and sends a single trigger pulse to the camera with the correspond-

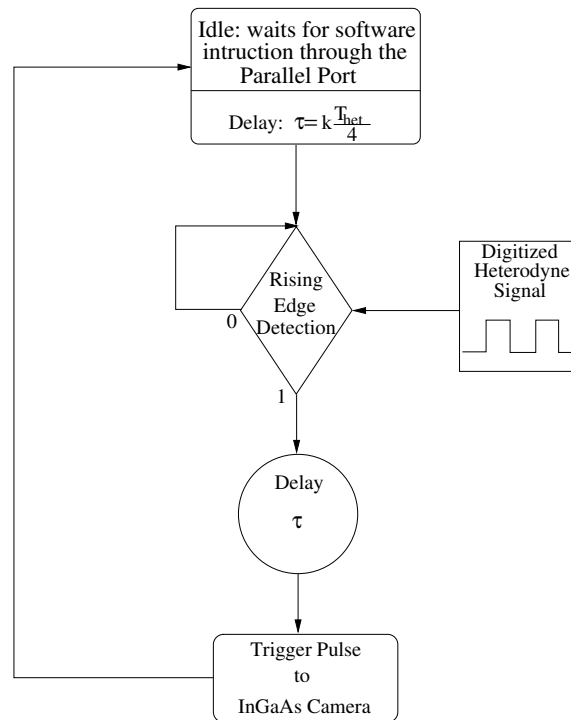


Figure 5.11: Flow diagram of the program of the FPGA for the new application

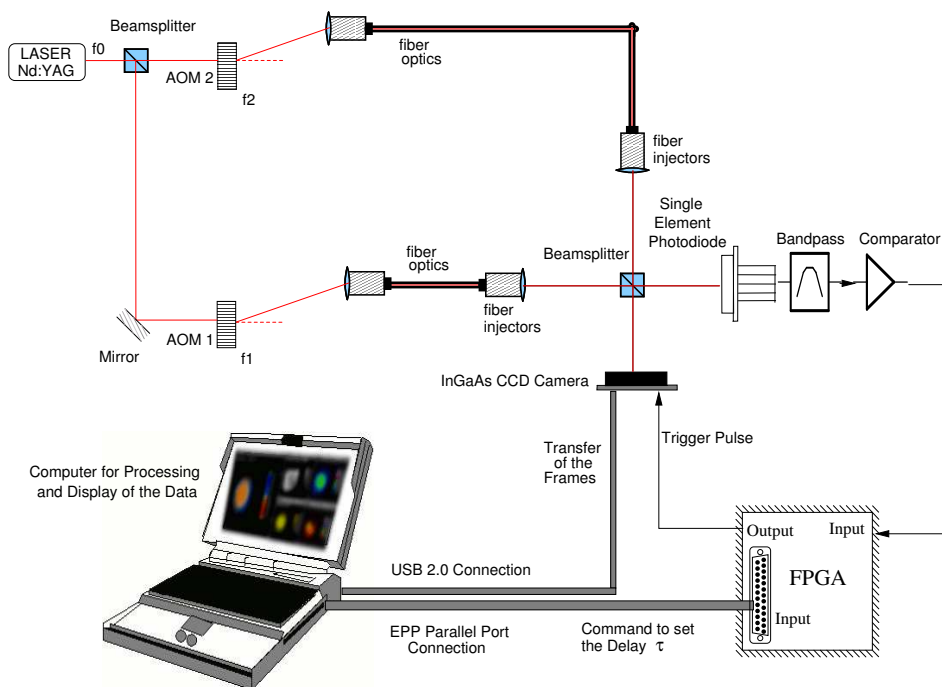


Figure 5.12: Setup for the real-time measurement of the phase front with the InGaAs camera

ing delay with respect to the rising edge detection. After the software has sent M delay commands to the FPGA, and the camera has captured M exposures which are separated from each other by $\frac{T_{\text{het}}}{4}$, the frames are processed by the software that applies a pixelwise phase estimation algorithm on them.

The estimated data is displayed by the software on the graphical user interface (GUI). This procedure is run continuously and is fast enough to accomplish a real-time measurement.

5.2.2 Graphical User Interface

The graphical user interface (GUI) had to be programmed in a graphical library fast enough to display the data in real-time.

After testing different possibilities, the library chosen was GLUT (OpenGL Utility Toolkit) for its fast performance on displaying the data. Figure 5.13 presents the GUI designed for this application.

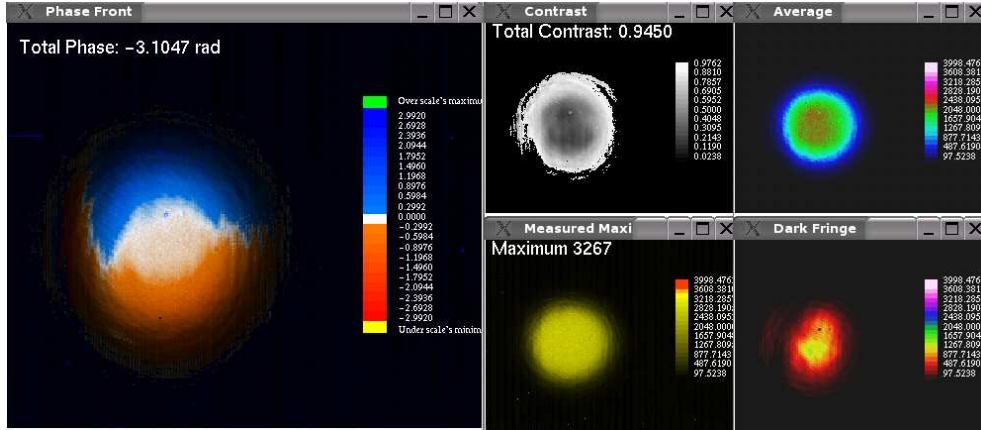


Figure 5.13: Graphical User Interface (GUI) develop for the display of the data

The whole software was written in the C programming language on a Linux operating system. The compiler used is the Gnu C Compiler (gcc) 3.3.3.

After the camera has been triggered M times, the intensity information corresponding to every pixel of each frame is saved in a matrix. The software processes these frames pixelwise. The results are saved in separated matrices to be displayed in the corresponding windows.

The following sections introduce each display independently together with an explanation of the calculations performed by the software for the data represented on them.

To simplify the explanation of the calculations for each display, the following variables are defined for the pixel n as

$$s_n = \sum_{k=0}^{M-1} b_k \cdot I_k^{(n)} \quad (5.1)$$

$$(5.2)$$

$$c_n = \sum_{k=0}^{M-1} a_k \cdot I_k^{(n)} \quad (5.3)$$

$$(5.4)$$

$$d_n = \sum_{k=0}^{M-1} h_k \cdot I_k^{(n)} \quad (5.5)$$

$$(5.6)$$

$$sum = \sum_{k=0}^{M-1} h_k \quad (5.7)$$

where s_n and c_n are the real and imaginary part of the oscillating term measured by the pixel n respectively. The coefficients h_k are a linear combination of the coefficients a_k and b_k defined in equation 3.4. The parameter d_n is proportional to the average intensity of the signal on the pixel n , and the intensity $I_k^{(n)}$ is the intensity measured by the pixel n in the exposure k .

The following parameters can be used for calculations of quantities over the whole surface.

$$s_{total} = \sum_n s_n \quad (5.8)$$

$$(5.9)$$

$$c_{total} = \sum_n c_n \quad (5.10)$$

$$(5.11)$$

$$d_{total} = \sum_{k=0}^{M-1} h_k \cdot I_k^{avg} \quad (5.12)$$

$$(5.13)$$

$$I_k^{avg} = \sum_n \frac{I_k^{(n)}}{n} \quad (5.14)$$

where I_k^{avg} is the averaged intensity measured by the frame k .

Phase Front

The *Phase Front* display shows the results of the measurement of the spatial distribution of the phase front and is shown by figure 5.14.

The phase front is estimated pixelwise by the algorithms presented in section 3. Using the notation introduced in this section, the phase φ_n measured at the pixel n can be estimated as

$$\varphi_n = \arctan\left(\frac{c_n}{s_n}\right) \quad (5.15)$$

Using equations 5.8 and 5.10, the total phase can be calculated as

$$\varphi_{total} = \arctan\left(\frac{c_{total}}{s_{total}}\right) \quad (5.16)$$

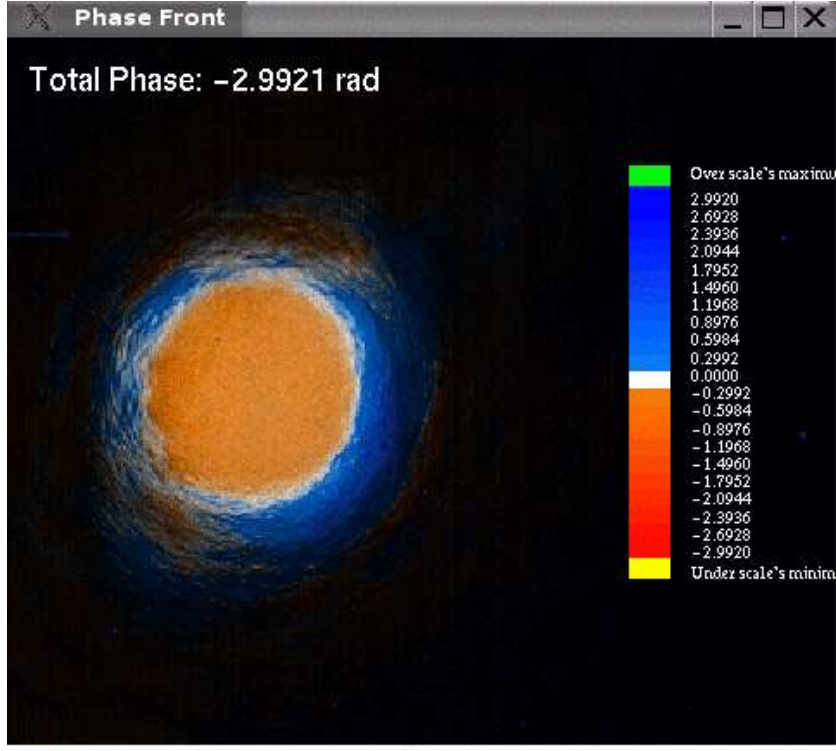


Figure 5.14: Window to display the phase front

In order to simplify the recognition of significant changes in the structure of the phase front, the values of the phases φ_n are shifted to a phase φ'_n centered around a reference, namely 0 rad.

This can be easily accomplished by subtracting the total phase φ_{total} from the phase φ_n in each pixel. Problems with phase jumps of the arctan function are avoided by using the equivalent formulation with complex numbers:

$$\varphi'_n = \arg \left(\frac{z_n}{z_{\text{total}}} \right) \quad (5.17)$$

where $z_n = s_n + i \cdot c_n$ and $z_{\text{total}} = s_{\text{total}} + i \cdot c_{\text{total}}$.

The palette was chosen such that the phases φ'_n designate the color of the pixels, blue for positive phases and red for negative phases. The scale can be modified by the user during a measurement, therefore the colors green and yellow represent the regions within the area of interest where the value of the phase is greater/less than the upper/lower limit of the scale respectively.

However, the phase is calculated for every pixel of the camera, even at the edges of the interference pattern where the intensity is negligible and is dominated by background noise. Naturally, the values obtained for the phase in these areas are not representative.

Therefore, the palette was chosen as a HSB (Hue-Saturation-Brightness) scheme, where only the characteristics provided by hue and brightness are considered. Hue is the actual color for each pixel n given by an RGB model and can be expressed

as the vector

$$\text{hue}(\varphi_n) = \{r(\varphi_n), g(\varphi_n), b(\varphi_n)\} \quad (5.18)$$

with $0 \leq r(\varphi_n), g(\varphi_n), b(\varphi_n) \leq 1$ for the coloring corresponding to φ_n . The brightness $\text{brg}(\varphi_n)$ of each pixel n is determined by the ratio of the maximum intensity measured at each pixel and the maximum intensity measured by the camera over M acquired exposures for a phase front estimation

$$\text{brg}(\varphi_n) = \left(\frac{I_{\max}^{(n)}}{I_{\max}} \right)^\gamma \quad (5.19)$$

where γ is known as Gamma factor in image processing and defines the contrast of an image.

Thus, the palette can be described as shown in figure 5.15

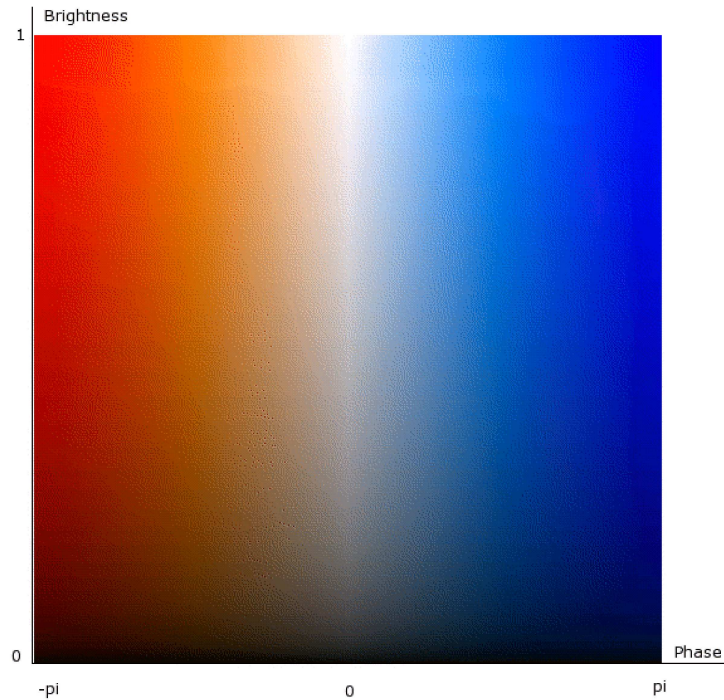


Figure 5.15: Palette chosen for the display of the phase front

From equations 5.18 and 5.19, the coloring $\text{col}(n)$ displayed for the pixel n is given by the RGB model $\{r_n, g_n, b_n\}$ and can be calculated as

$$\text{col}(n) = \{r_n, g_n, b_n\} = \text{brg}(\varphi_n) \cdot \text{hue}(\varphi_n) \quad (5.20)$$

Maximum

The window *Measured Maximum* displays the maximum intensity $I_{\max}^{(n)}$ measured by the camera at the pixel n over M takings. Figure 5.16 shows this display.

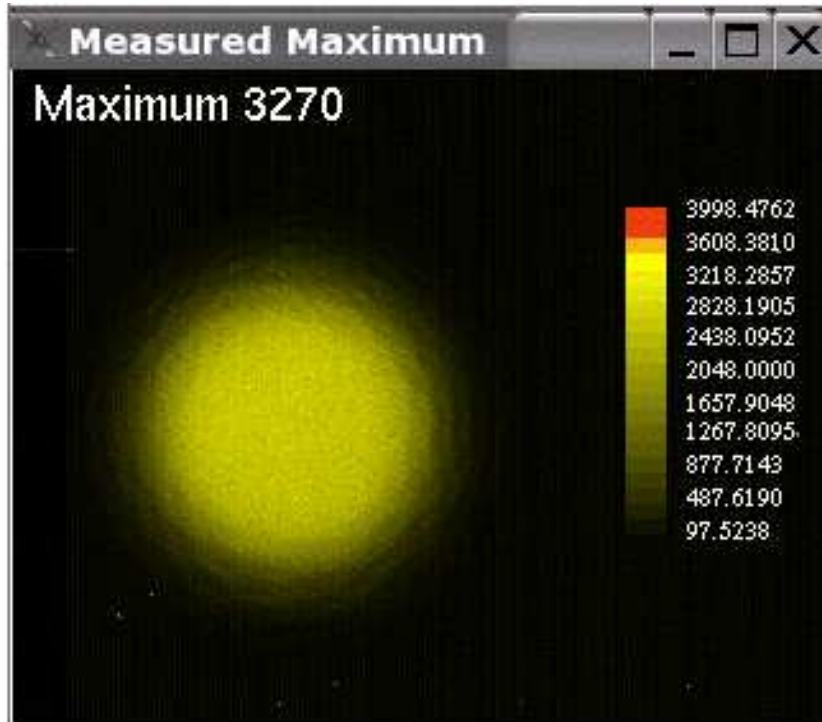


Figure 5.16: Window that displays the maximum intensity on every pixel

The maximum possible intensity value given by the camera is 4095 a.u., since the A/D converter of the camera has a dynamic range of 12 bit.

The palette was selected to represent the data by the brightness of a constant color, namely yellow. If the maximum intensities measured come close to the camera's maximum, the corresponding pixels begin turn red. This helps the user to notice easily if the camera is becoming overexposed, in order to prevent damages to the device, and distortion of the data.

Average

The *Average* display shows a weighted average of the intensity on each pixel over M frames acquired. Figure 5.17 shows the display captured at a real measurement.

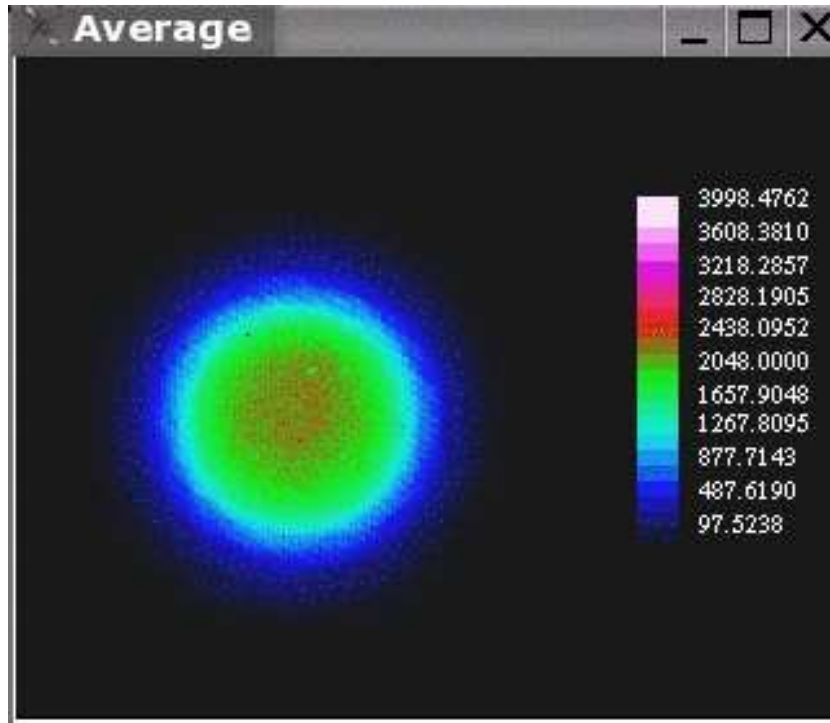


Figure 5.17: Window to display the average of the intensity

The averaged intensity $I_{\text{avg}}^{(n)}$ for the pixel n is calculated as

$$I_{\text{avg}}^{(n)} = \frac{d_n}{\text{sum}} \quad (5.21)$$

Afterwards, this intensity $I_{\text{avg}}^{(n)}$ is converted into a color and displayed for every pixel. In this case, the intensities are represented by a conventional multicolor scale.

Contrast

The window *Contrast*, in figure 5.18, displays the contrast calculated for every pixel.

The contrast con_n for the pixel n can be calculated as

$$con_n = 2 \cdot \frac{\sqrt{s_n^2 + c_n^2}}{d_n} \quad (5.22)$$

Hence, the overall contrast con_{total} can be computed, according to equations 5.8, 5.10, and 5.12 as

$$con_{\text{total}} = 2 \cdot \frac{\sqrt{s_{\text{total}}^2 + c_{\text{total}}^2}}{d_{\text{total}}} \quad (5.23)$$

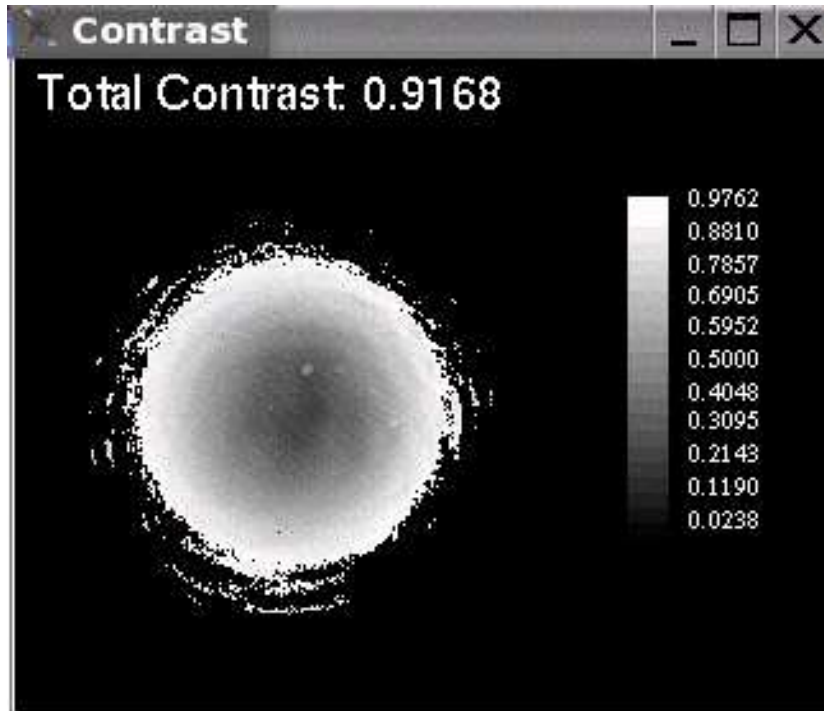


Figure 5.18: Display of the contrast on every pixel

Dark Fringe

The *Dark Fringe* display, in figure 5.19, shows an actual exposure of the interference pattern.

After M frames were captured and all the preceding calculations of the foregoing windows were accomplished by the program, the FPGA sends an extra trigger pulse to the camera with a delay (τ with respect to a rising edge of the digitized heterodyne signal from the single-element photodiode) computed as

$$\tau = \frac{\frac{3\pi}{2} - \varphi_{\text{total}}}{2 \cdot \pi} \cdot T_{\text{het}} \quad (5.24)$$

This delay corresponds to the location of the minimum of the sinusoid and takes into account the phase difference of π between the both outputs of the beamsplitter where the recombination of the beams take place.

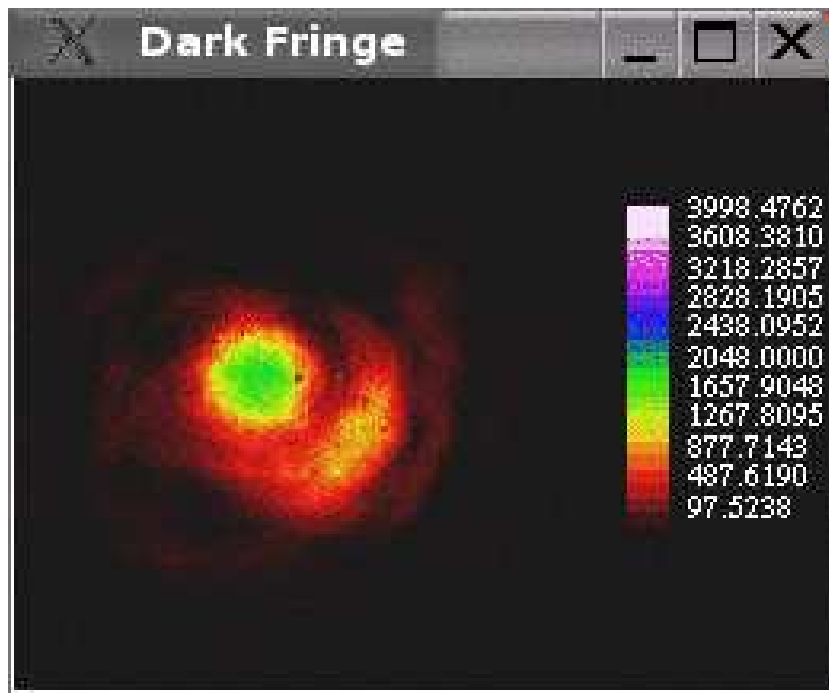


Figure 5.19: Window to display a frame of the dark fringe

This GUI was equipped with some special features to make this software more user friendly. More information about the functions implemented until now can be found in [appendix B](#).

6 Results

This chapter presents several measurements performed with the configuration introduced in section 5.2 utilizing the real-time phasemeter developed in this thesis with the XEVA USB camera. These results show that the phasemeter is able to measure the spatial distribution of the phase front in real-time with sufficient spatial resolution.

6.1 Alignment Procedure

The real-time display of the data (approximately 5-6 phase fronts per second) allows the user to perform an optimal adjustment of the interferometer. The following images present a short sequence of an alignment procedure. As shown in figure 6.1, the horizontal and vertical coordinates of the beams (with respect to the camera) must be corrected to achieved their recombination.

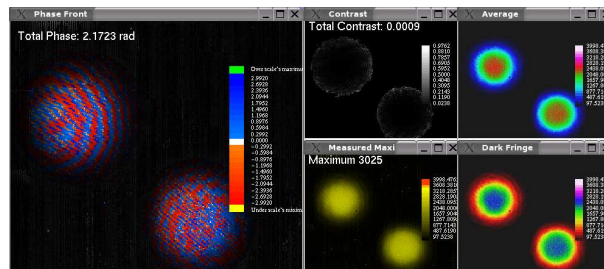


Figure 6.1: Step 1: Alignment procedure of an interferometer

The information displayed by the program allows the user to perform these corrections accurately.

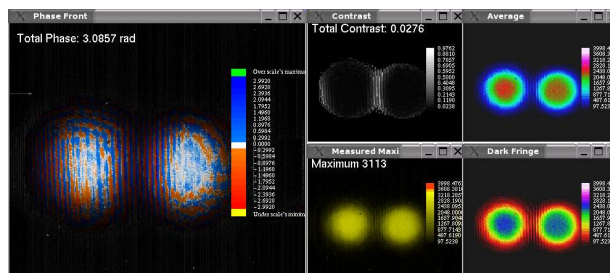


Figure 6.2: Step 2: Alignment procedure of an interferometer

Consequently to the situation presented in figures 6.1 and 6.2, the window *Phase Front* does not display a defined structure of a phase front.

Figure 6.3 shows how the beams begin to interfere. Therefore, the window *Contrast* displays a thin area where the contrast increases.

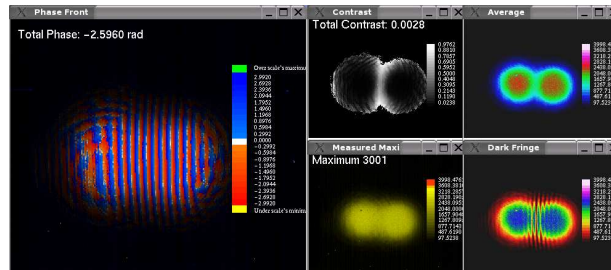


Figure 6.3: Step 3: Alignment procedure of an interferometer

As the interference of the beams improves, the displayed phase front begins to present a defined structure. It can be seen in figure 6.4 that the contrast raises over the area of interest as well.

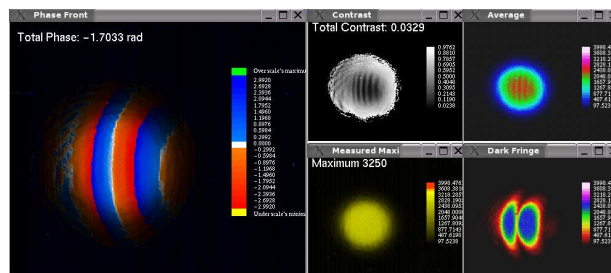


Figure 6.4: Step 4: Alignment procedure of an interferometer

In figure 6.5, the phase front presents a well-defined structure. This is an indicator that the beams have been aligned properly. However, the phase front shows an inhomogeneous spatial distribution and the contrast is still not optimal. At this stage, the parameters of the interfering beams can be optimized by adjusting the lenses in the fiber injectors.

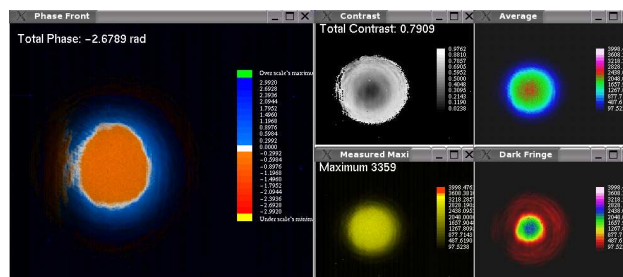


Figure 6.5: Step 5: Alignment procedure of an interferometer

Figure 6.6 shows the displayed data after a slight correction of the position of the lens in one of the fiber injectors. The higher grade of white in the *Phase Front* window indicates a more evenly distributed phase front. The display *Contrast* also shows a significant increment in the overall contrast. This complies with the intensity measured at the dark fringe, which considerably diminished.

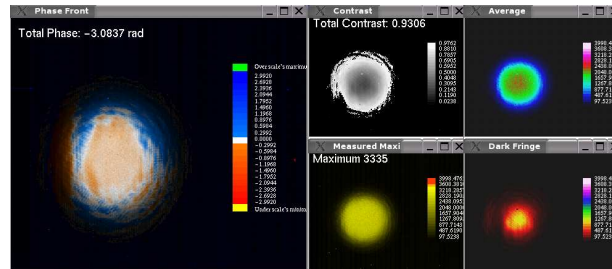


Figure 6.6: Step 6: Alignment procedure of an interferometer

6.2 Misaligned Interferometer

In this case, the misalignment can be understood as a small tilt between the two beams when the recombination takes place. This tilt is enough to maintain sufficient contrast for triggering at the photodiode.

Due to the angle between both beams, the planes perpendicular to the propagation axes of the beams are not parallel. This means that the cross section of the interference pattern is tilted with respect to the plane of the camera.

The influence of such a tilt between the beams on the phase front is a linear gradient of the spatial distribution of the phase relative to the plane of the camera.

Figure 6.7 shows a graphic representation of this misalignment.

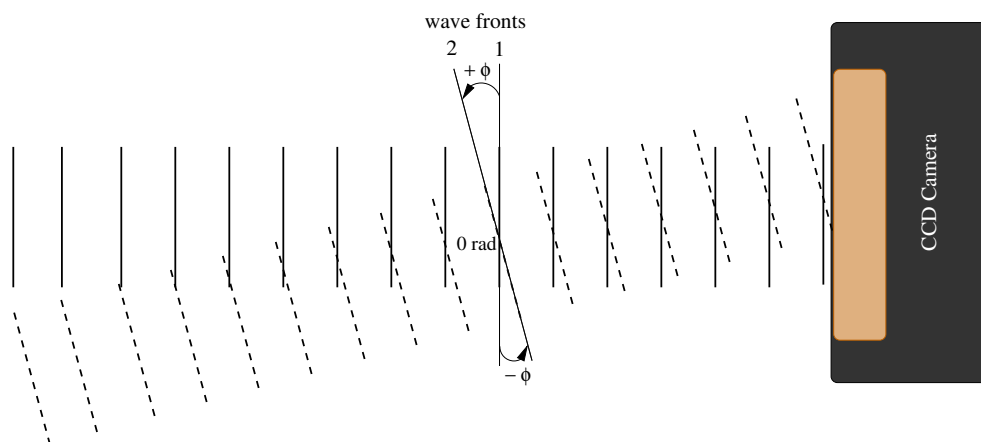


Figure 6.7: Interference between two slightly tilted beams. Phase front measured with the XEVA USB camera

The interferometer was misaligned intentionally to measure the phase front in this configuration. An image of the phase front measured in this case is presented in figure 6.8.

The linear gradient of the spatial distribution of the phase can be clearly identified by the color scale of the graph and the 3D illustration of the data, which represents a tilt of the phase front with respect to the plane of the CCD camera. Thus this measurement confirms the explanation given above, and implies that the measurement procedure works as expected.

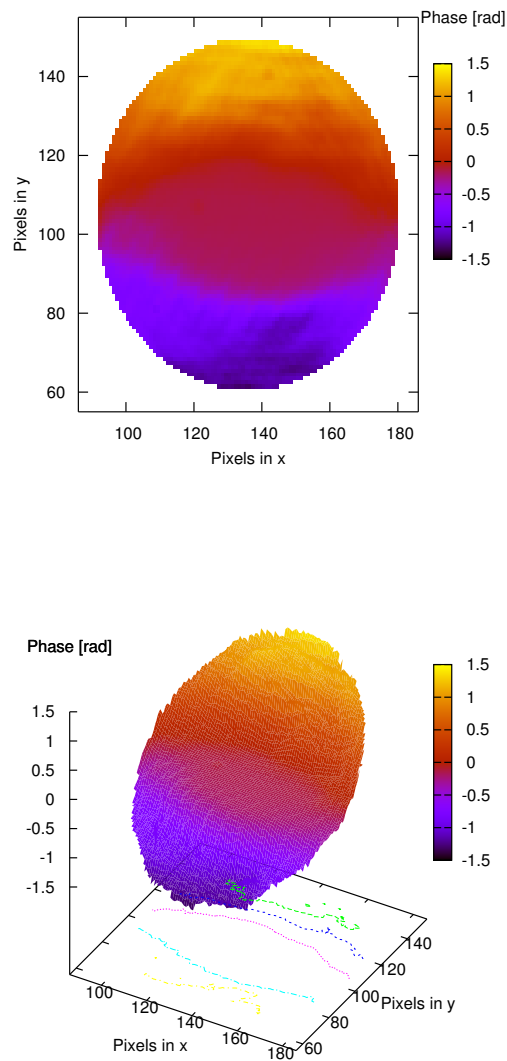


Figure 6.8: Phase front measured with the XEVA USB camera between two slight tilted beams

6.3 Different Beam Parameters

For this measurement, the lens at one of the fiber injectors was misaligned. By doing this, the parameters of the beam coming out from this fiber injector were strongly changed. This influences the recombination of the beams affecting severely the phase front. The results of this measurement is shown in figure 6.9.

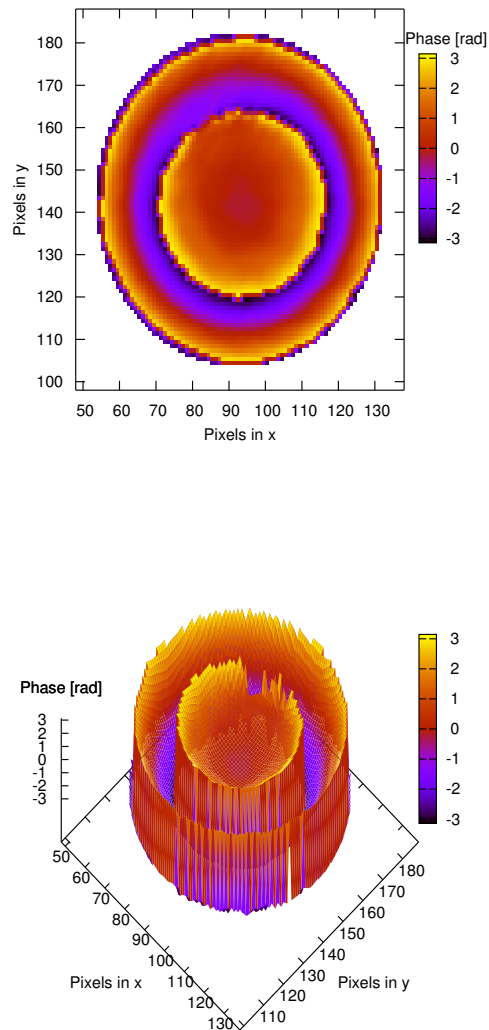


Figure 6.9: Phase front measured with the XEVA USB camera for a misaligned lens of a fiber injector. Different beam parameters

This result complies with the phase front measured using the WinCamD camera shown in figure 5.8. The lens at the fiber injector affects the wave front of the beam similar to the lens used in the experimental setup in figure 5.7.

6.4 Engineering Model of the LTP Interferometer

Due to its high relevance for the LPF mission, a phase front measurement was performed on one of the four interferometers of the engineering model of the optical bench. For practical reasons, the frequency interferometer (see figure 6.10) was chosen, since it is the only one with nearly identical armlengths.

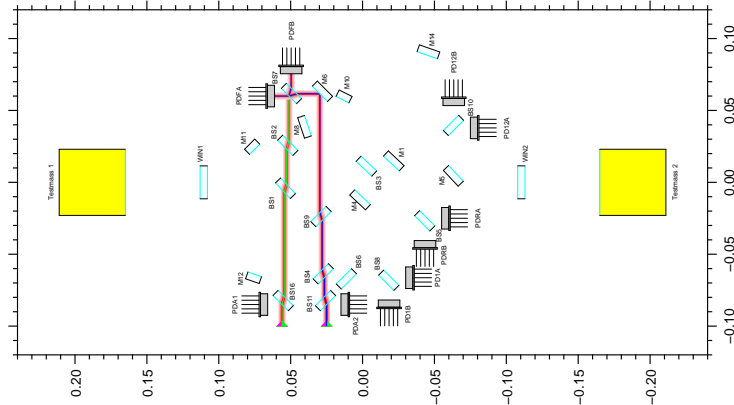


Figure 6.10: Frequency interferometer of the engineering model of the optical bench for the LTP

The phase front obtained from this measurement is shown in figure 6.11.

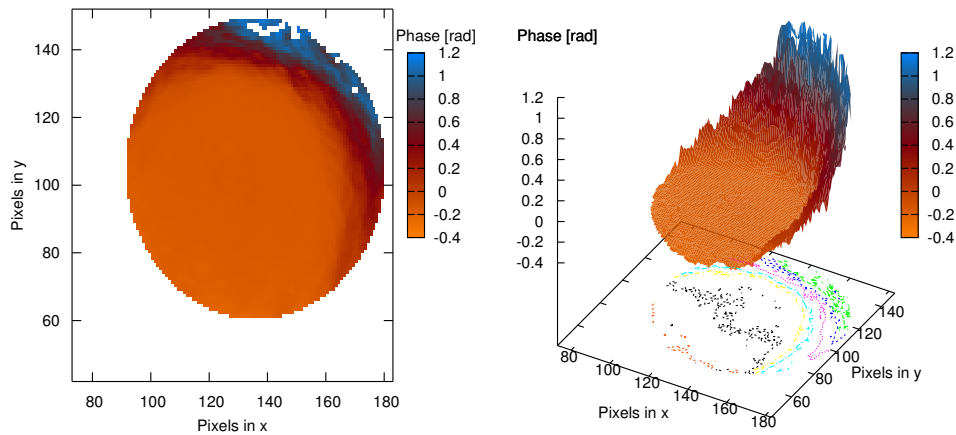


Figure 6.11: Phase front measured at the engineering model of the optical bench for the LTP with the XEVA USB camera

It is clear that the phase front is not homogeneous, and this can be attributed to the misalignment of the lenses in the fiber injectors. This fact implies a discrepancy on the parameters of both beams, since the armlengths of the in-

terferometer are practically equal.

It can be read from the scale that this flexion is not large in the center. However, the 3D illustration shows a significant inhomogeneity of the spatial distribution of the phase front.

This inhomogeneity in the phase front combined with with beam jitter can adversely affect the performance of the interferometer for LISA Pathfinder, because the optical bench of the LTP has quadrant photodiodes for the phase measurement.

6.5 Homogeneous Phase Front

The most important question in the scope of this thesis was, how easily can a phase front be homogenized by simple adjustment.

An experiment was conducted on a tabletop interferometer utilizing the spatially resolving phasemeter.

This experiment aimed the adjustment of the lenses in the fiber injectors, in order to obtain a homogeneous spatial distribution of the phase front with help of this new device. The outcome of this experiment is illustrated by figure 6.12.

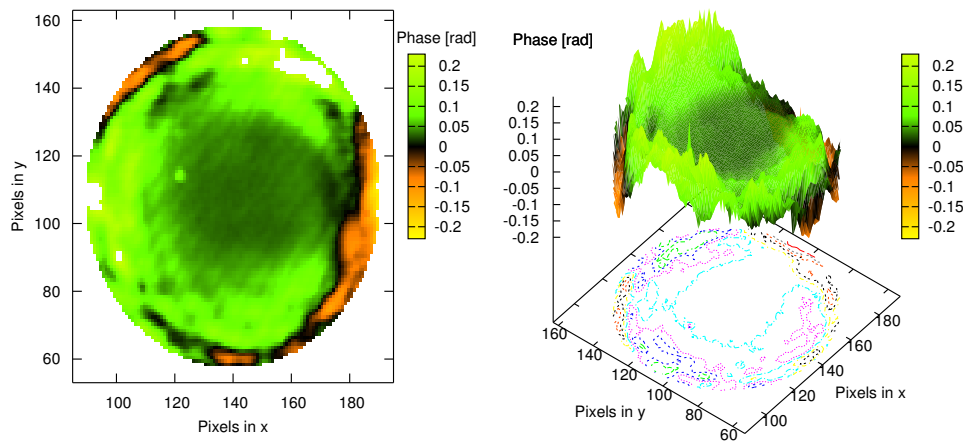


Figure 6.12: Homogeneous phase front obtained by the adjustment of the lenses in the fiber injectors on a tabletop interferometer

Figure 6.12 shows a considerably broad area of the phase front presenting a homogeneous structure.

The adjustment of this homogeneous phase front was easily accomplished by using conventional laboratory equipment.

The decisive factor in this achievement was the availability of a device that allows the user to visualize the structure of the phase front in real-time, enabling them to adjust the optics on the interferometer according to the displayed data.

Since the phase front presents a homogeneous spatial distribution, the loss of information would not affect so strong the performance of the phase measurements with quadrant photodiodes, due to beam pointing jitter on the quadrants.

The results obtained from the Engineering Model and essentially from this experiment strongly suggest the application of this device for the development of the final Flight Model of the LTP optical bench. This will enable a proper adjustment of the optical components to improve the performance of the interferometry designed for LISA Pathfinder.

A Frequency Analysis of a Bandpass Filter

A frequency analysis of the bandpass filter shown in figure 4.8 is given in this section. The transfer function is obtained from the reduction of the block diagram representation obtained for this filter. Therefore, a short explanation of the block algebra is given as well.

A.1 Block Algebra

A block diagram is a pictorial representation of a system and the links between its subsystems. The block algebra is the group of operations which can be applied to the blocks representing the parts of a system. These operations allow to simplify the diagram and unify all the blocks to a single one, which contains the transfer function of the entire system. The block algebra consists of simple arithmetical operations which can be obtained from the mathematical expressions of the links represented by a block diagram. Some of the most frequently cases are presented in this section.

A.1.1 Cascade Blocks

The connection of blocks in a block diagram as shown in figure A.1 is called cascade.

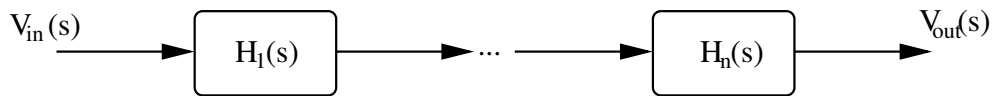


Figure A.1: Diagram of n -blocks in cascade

Each block represents a part of a system with a transfer function $H_i(s)$. This transfer function is normally represented in the frequency domain, where the complex variable $s = i \cdot \omega$ is the Laplace variable.

For the case of the cascade blocks in figure A.1, the transfer function of the system $H(s)$ can be expressed as

$$H(s) = \frac{V_{\text{out}}(s)}{V_{\text{in}}(s)} = \prod_{i=1}^n H_i(s) \quad (\text{A.1})$$

A.1.2 Parallel Blocks

In a block diagram, the connection in parallel of the blocks can be outlined by figure A.2.

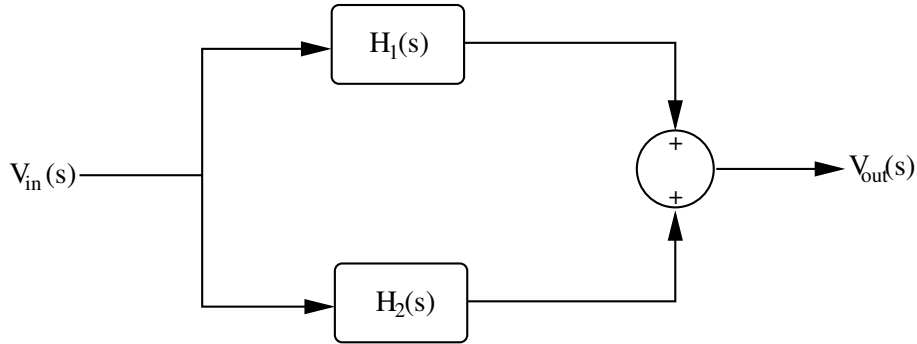


Figure A.2: Diagram of blocks connected in parallel

The transfer function of the system $H(s)$ can be calculated in this case as

$$H(s) = \frac{V_{out}(s)}{V_{in}(s)} = H_1(s) + H_2(s) \quad (\text{A.2})$$

For the general case, where n -blocks are connected in parallel, the transfer function of the system $H(s)$ would be given by

$$H(s) = \frac{V_{out}(s)}{V_{in}(s)} = \sum_{i=1}^n H_i(s) \quad (\text{A.3})$$

A.1.3 Feedback

One of the most common links illustrated by a block diagram is the feedback, as shown in figure A.3.

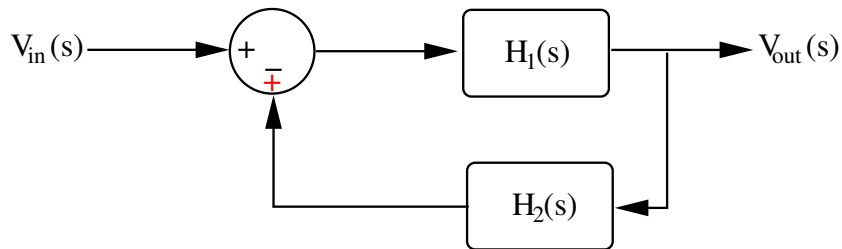


Figure A.3: Representation of feedback in a block diagram

The transfer function of such a link can be expressed as

$$H(s) = \frac{V_{out}(s)}{V_{in}(s)} = \frac{H_1(s)}{1 \pm H_1(s) \cdot H_2(s)} \quad (\text{A.4})$$

A.1.4 Displacement of Bifurcation Points

The bifurcation points in a block diagram can be displaced back and forth as shown in figure A.4.

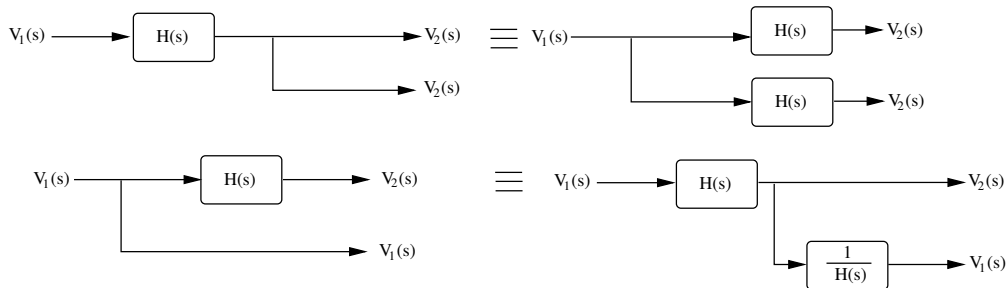


Figure A.4: Displacement of bifurcation points in a block diagram

A.1.5 Displacement of Summation Points

The displacement of summation points in a block diagram is outlined by figure A.5.

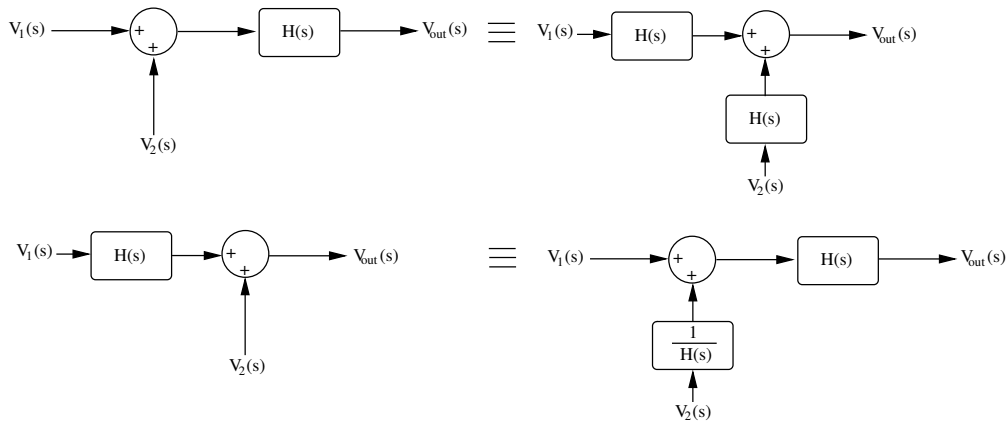


Figure A.5: Displacement of summation points in a block diagram

A.2 Bandpass Filter

The bandpass filter presented in figure 4.8 and shown here in figure A.6 can be represented in a block diagram. The operations described in the foregoing section can be applied to this diagram in order to obtain easily the transfer function of this filter.

Many programs have been developed to analyze and simulate the behavior of electronic circuits in the frequency domain, providing a faithful description of the system in short time and without much effort like LISI, used in this work,

or SPICE.

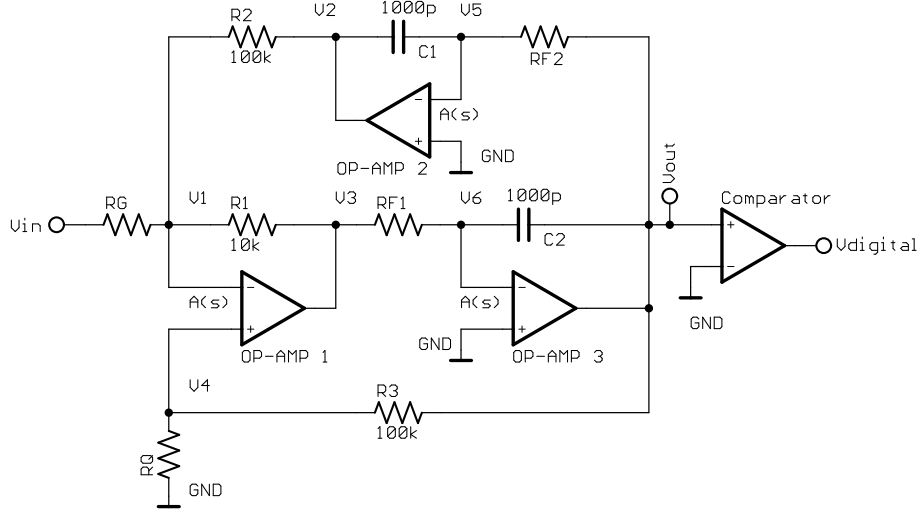


Figure A.6: Circuit of the bandpass filter used in the experimental setup

However, the author found interesting to present the analysis of this filter by using the block diagram method, since it allows to obtain a representative model of a system, like this simple electronic circuit, and to calculate easily its transfer function after few steps.

The first step to obtain the block diagram of this system is to express each voltage, between the corresponding node and ground, in terms of the other voltages. The easiest and fastest way to do this, is to calculate each voltage from the superposition of the voltages between ground and the neighbor nodes. For example, $V_1(s)$ can be obtained from the superposition of $V_{in}(s)$, $V_2(s)$, and $V_3(s)$.

This means that $V_1(s)$ is given by the sum of the expressions obtained when only one of corresponding voltages is considered active ($V_2(s) = 0$, $V_3(s) = 0$; $V_3(s) = 0$, $V_{in}(s) = 0$; $V_2(s) = 0$, $V_{in}(s) = 0$). Thus, $V_1(s)$ is given by

$$V_1(s) = \underbrace{\frac{R_1 // R_2}{R_G + R_1 // R_2}}_{K_1} \cdot V_{in}(s) + \underbrace{\frac{R_1 // R_G}{R_2 + R_1 // R_G}}_{K_2} \cdot V_2(s) + \underbrace{\frac{R_2 // R_G}{R_1 + R_2 // R_G}}_{K_3} \cdot V_3(s) \quad (\text{A.5})$$

where $R_x // R_y$ denotes the parallel of R_x and R_y . Similarly, for $V_4(s)$ yields

$$V_4(s) = \underbrace{\frac{R_Q}{R_3 + R_Q}}_{K_4} \cdot V_{out}(s) \quad (\text{A.6})$$

The voltage $V_5(s)$ can be expressed as

$$V_5(s) = \underbrace{\frac{X_C}{R_F + X_C}}_{K_5(s)} \cdot V_{\text{out}}(s) + \underbrace{\frac{R_F}{R_F + X_C}}_{K_6(s)} \cdot V_2(s) \quad (\text{A.7})$$

where $X_C = \frac{1}{i\omega \cdot C} = \frac{1}{s \cdot C}$ is the frequency dependent impedance of the capacitance C .

In a similar way, $V_6(s)$ is given by

$$V_6(s) = \underbrace{\frac{X_C}{R_F + X_C}}_{K_5(s)} \cdot V_3(s) + \underbrace{\frac{R_F}{R_F + X_C}}_{K_6(s)} \cdot V_{\text{out}}(s) \quad (\text{A.8})$$

The voltages $V_2(s)$, $V_3(s)$, and $V_{\text{out}}(s)$ are the outputs of the operational amplifiers. Since the operational amplifier amplifies the difference between its two inputs ($V_+ - V_-$), these voltages can be expressed as

$$V_2(s) = -A(s) \cdot V_5(s) \quad (\text{A.9})$$

$$V_3(s) = A(s) \cdot (V_4(s) - V_1(s)) \quad (\text{A.10})$$

$$V_{\text{out}}(s) = -A(s) \cdot V_6(s) \quad (\text{A.11})$$

where $A(s)$ is the frequency dependent gain of the operational amplifier.

The links represented from equation A.5 to equation A.11 allow to build easily the following block diagram

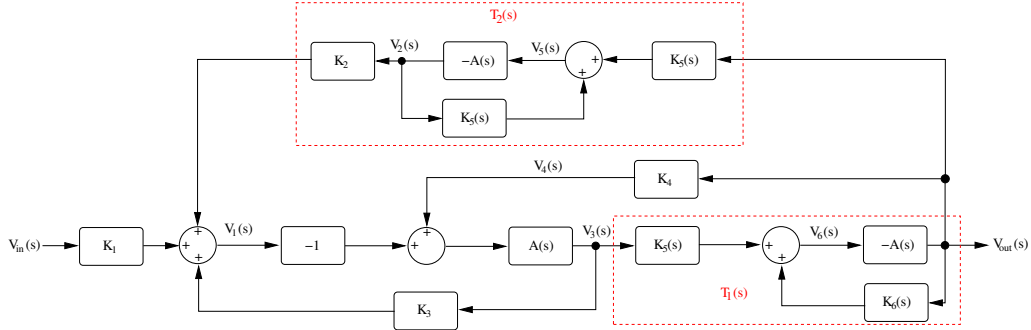


Figure A.7: Block diagram of the bandpass filter shown in figure A.6

The blocks inside the dashed rectangles can be easily reduced, since they are only a combination of one positive feedback in cascade with other blocks. Hence, from equations A.4 and A.1 yields

$$T_1(s) = \frac{-K_5(s) \cdot A(s)}{1 + K_6(s) \cdot A(s)} \quad (\text{A.12})$$

$$T_2(s) = \frac{-K_2 \cdot K_5(s) \cdot A(s)}{1 + K_6(s) \cdot A(s)} \quad (\text{A.13})$$

The bifurcation point before $T_1(s)$ ($V_3(s)$) can also be moved as shown in figure A.4. Hence, in this first step the block diagram can be reduced to figure A.8.

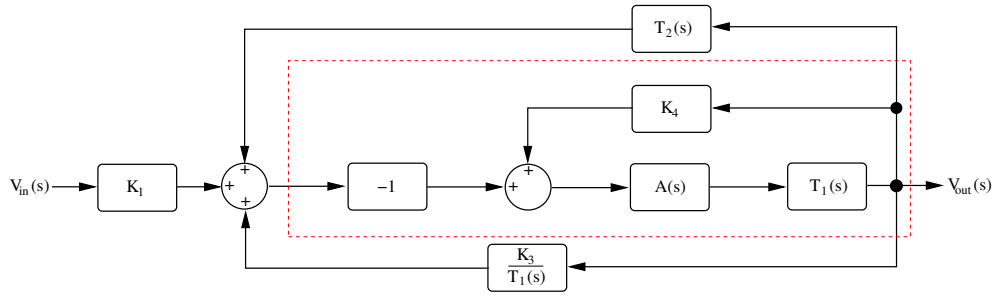


Figure A.8: First simplification of the block diagram shown in figure A.7

The next simplification is marked on figure A.8 by a dashed rectangle. This is only a positive feedback in cascade with a block. Thus, the simplified block diagram is shown in figure A.9.

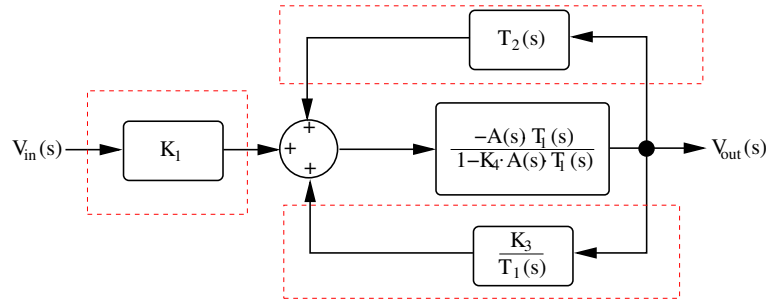


Figure A.9: Second simplification of the block diagram shown in figure A.7

Figure A.9 shows 2 blocks in parallel and a summation point that can be easily displaced. Thus, according to equation A.3 and figure A.5, the block diagram can be finally reduced to

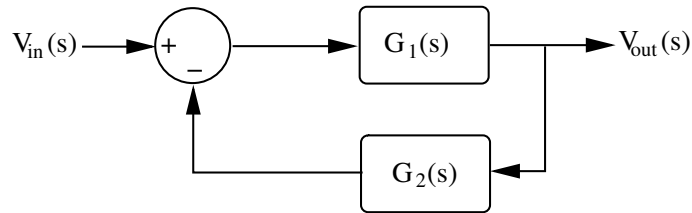


Figure A.10: Reduced block diagram of the bandpass filter shown in figure A.6

where

$$G_1(s) = \frac{-K_1 \cdot A(s) \cdot T_1(s)}{1 - K_4 \cdot A(s) \cdot T_1(s)} \quad (\text{A.14})$$

$$G_2(s) = \frac{-K_3}{K_1 \cdot T_1(s)} - \frac{T_2(s)}{K_1} \quad (\text{A.15})$$

Hence, the transfer function of the filter $H(s)$ is given by

$$H(s) = \frac{V_{\text{out}}(s)}{V_{\text{in}}(s)} = \frac{G_1(s)}{1 + G_1(s) \cdot G_2(s)} \quad (\text{A.16})$$

Usually, the operational amplifier is taken as ideal. This means that $A(s) \rightarrow \infty$. In this case, the operational amplifier used is the OP27 from Texas Instruments, which is a conventional operational amplifier.

The gain of an operational amplifier $A(s)$ can be modelate in first order as

$$A(s) = \frac{GBW}{s + \omega_a} \quad (\text{A.17})$$

where GBW is the gain-bandwidth product and ω_a is the frequency of the first pole in the transfer function of the operational amplifier.

According to figure 14 of the datasheet of the OP27 (figure A.11), available in the internet homepage of Texas Instruments, the frequency $\omega_a = 2 \cdot \pi \cdot 8$ and the gain-bandwidth product $GBW = 2 \cdot \pi \cdot 8 \cdot K_G$. K_G is the gain of the operational amplifier, which is read from this curve 127 dB.

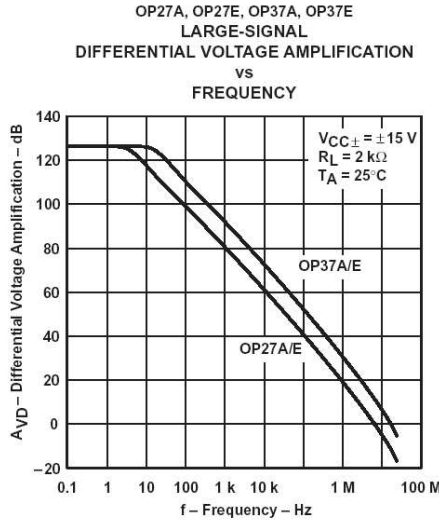


Figure 14

Figure A.11: Large-signal differential voltage amplification of the OP27 [13]

According to figure A.6 and equations 4.1, the resistors and capacitors used for the filter at 1600 Hz are

$$R_F = R_{F1} = R_{F2} = 30.1 \text{ k}\Omega \quad (\text{A.18})$$

$$R_Q = 27.4 \text{ k}\Omega \quad (\text{A.19})$$

$$R_1 = 10 \text{ k}\Omega \quad (\text{A.20})$$

$$R_2 = R_3 = 100 \text{ k}\Omega \quad (\text{A.21})$$

$$C = C_1 = C_2 = 1 \text{ nF} \quad (\text{A.22})$$

Substituting these values into the expression calculated for the transfer function of the filter and plotting its Bode diagram in figure A.12 yields

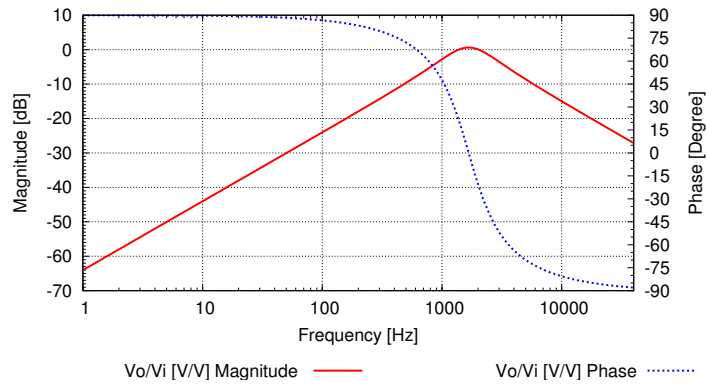


Figure A.12: Transfer function calculated for the bandpass filter in figure A.6 at a center frequency of 1600 Hz

This electronic circuit was also simulated with LISO¹, which is a program to fit and simulate analog electronic circuits. The transfer function of this bandpass filter obtained from the LISO simulation is presented in figure A.13.

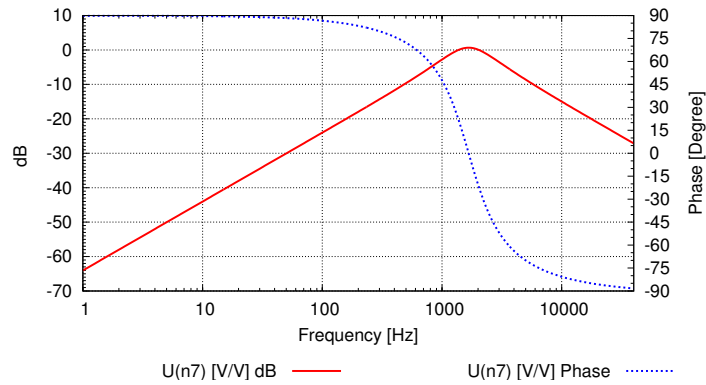


Figure A.13: Transfer function obtained by LISO for the bandpass filter in figure A.6 at a center frequency of 1600 Hz

The spectrum analyzer SR785, distributed by Stanford Research Systems, was used to measure the transfer function of this filter. The measurement was

¹developed by Gerhard Heinzel

conducted with relative long integration and averaging. This can explained the unusual low noise level shown by the acquired data at low frequencies. The transfer function obtained from this measurement is shown in figure A.14.

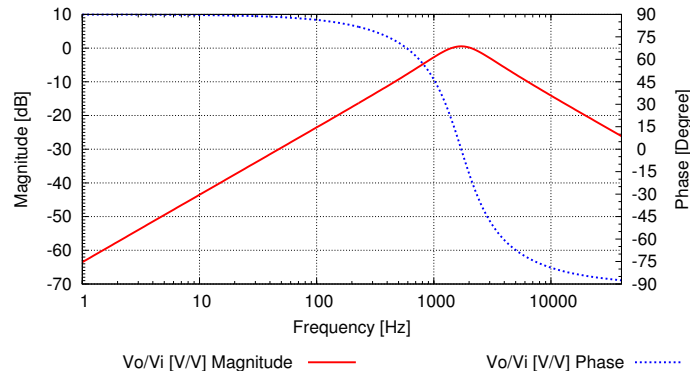


Figure A.14: Transfer function measured for the bandpass filter in figure A.6 at a center frequency of 1600 Hz

This filter was modified for the experimental setup presented in section 5.1.1. The center frequency was changed to 293 Hz. Therefore, only the resistor R_F was changed to 182 k Ω . Figure A.15 presents the transfer function calculated for this new filter, which complies with the LISO simulation. This transfer function was also measured with the spectrum analyzer SR785 (figure A.16) and showed a very low noise at low frequencies as well. As previously mentioned, this could be explained due to the relative long averaging set to the spectrum analyzer.

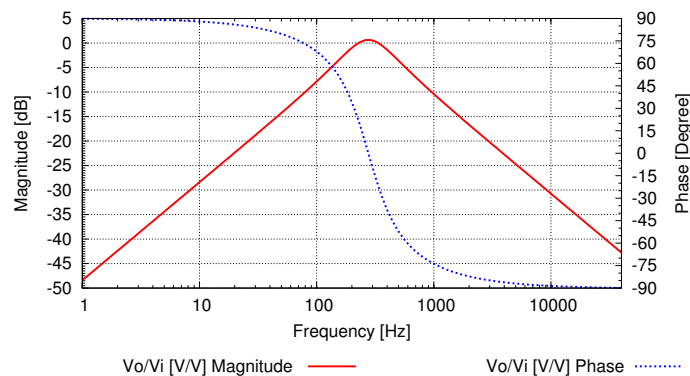


Figure A.15: Transfer function calculated for the bandpass filter in figure A.6 at a center frequency of 290 Hz

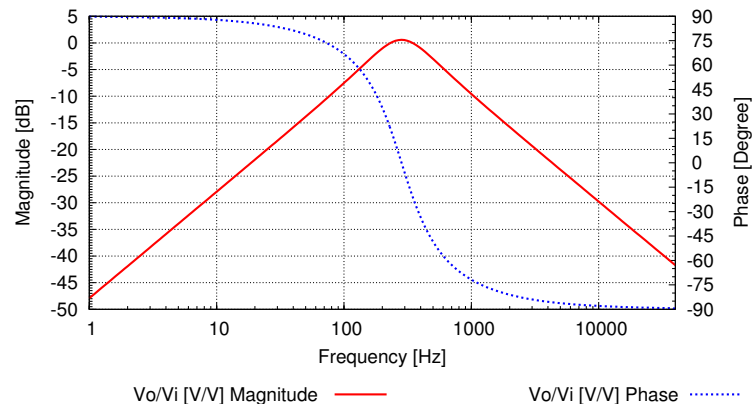


Figure A.16: Transfer function measured for the bandpass filter in figure A.6 at a center frequency of 290 Hz

B Features programmed for the GUI

The GUI is equipped with special functions which simplify and improve the display and process of the data and make the software gentler to the user.

These functions can be easily operated as "hotkeys" through the keyboard of the computer by pressing the corresponding key on an active window of the program.

These features can be classified in two groups: Functional Features and Display Features.

B.1 Functional Features

These features were implemented to improve the functionality of the device and include the following functions:

Save Data This function can be called by pressing the key "s". It creates a folder named by the date and time when the measurement was carried out in the format `YYYY - MM - DD_hh : mm : ss`.

This folder contains six text files, namely one for each of the five displays explained before and one containing the whole information in a format that can be read by Gnuplot.

Background Substraction The callback of this function is the key "b". This function is designed to capture three exposures of the background and average them. It sets the application in a stand-by modus, for the user to obstruct the laser, and waits for the ENTER key to be pressed to acquire the frames of the background. The intensity information obtained here is later on subtracted pixelwise from the new frames.

Period Measurement By pressing the key "p", the software operates the FPGA to conduct a measurement of the heterodyne period T_{het} in order to refresh on-line this value to be used in further calculations.

B.2 Display Features

This assembly of functions are used to modify on-line the display parameters for the Phase Front display only. They correct the display parameters, in order to help the user for a better analysis of the data. The functions implemented are:

Modification of the Palette This function can be activated by the keys "+" and "-" to change the palette of the display by increasing or decreasing the phase range represented by the white color respectively.

Brightness: GAMMA Factor The brightness of the displayed data can be modified by the increasing or decreasing the GAMMA factor through the keys "*" and "/" respectively. This factor multiplies the palette changing its brightness.

Scale: Upper Limit The upper limit of the phase scale can be incremented or decremented independently by pressing the keys "u" and "i" respectively.

Scale: Lower Limit The keys "l" and "k" increment or decrement the lower limit of the phase scale respectively.

Scale: Symmetric Shifting This function was designed to increment or decrement both limits of the scale uniformly by pressing the keys "h" and "j" respectively.

These last three features were programmed to enable an accurate analysis of smaller structures presented by the phase front, and thus support the user to perform fine adjustments, among other applications.

C Code Developed for the FPGA

This appendix presents the VHDL code developed for the FPGA, which is a main component of the phasemeter developed in this thesis.

```
-- ec0.vhd
-- CCD trigger for real-time phasefront measuring system
-- with parallel port interface (EPP mode)
-- written for ACTEL APA075 FPGA.
-- G. Heinzl, F. Guzmán Cervantes August 2004.

library IEEE;
use IEEE.STD_LOGIC_1164.all;
use IEEE.numeric_std.all;

entity clockdivider is
  port(clkin : in std_logic;
        reset : in std_logic;    -- active low
        clkout : out std_logic);
end clockdivider;

architecture behavior of clockdivider is
  signal clk20m, clk10msig : std_logic;
begin

  process (clkin, reset, clk20m)
  begin
    if reset = '0' then
      clk20m <= '0';
    elsif RISING_EDGE(clkin) then
      clk20m <= not clk20m;
    end if;
  end process;

  process (clk20m, reset, clk10msig)
  begin
    if reset = '0' then
      clk10msig <= '0';
    elsif RISING_EDGE(clk20m) then
      clk10msig <= not clk10msig;
    end if;
  end process;
  clkout <= clk10msig;
end behavior;

library IEEE;
use IEEE.STD_LOGIC_1164.all;
use IEEE.std_logic_arith.all;
```

Appendix C. Code Developed for the FPGA

```
entity ec is
  port(clk_40m      : in    std_logic; -- clock input
        epp_init   : in    std_logic; -- epp reset line, active low
        epp_data   : inout std_logic_vector (7 downto 0);-- epp data bus
        epp_write  : in    std_logic; -- low:write access
        epp_wait   : out   std_logic; -- max 10 us
        epp_data_strobe : in  std_logic; -- low data transfer
        epp_addr_strobe : in  std_logic; -- low address transfer
        epp_user1  : out   std_logic; --
        epp_user2  : out   std_logic; --
        epp_user3  : out   std_logic; --
        epp_intr   : out   std_logic; -- rising egde triggers PC interrupt
        epp_write_enable: out  std_logic; -- '1' indicates fpga writes data
        ccd_trigger : out   std_logic; -- trigger pulse for ccd camera
        fhet      : in    std_logic); -- input from comparator
end ec;

architecture behavioral of ec is
  type state_type is (state_0, state_1, state_2, state_3, state_4,
                     state_5, state_6, state_7, state_8, state_9,
                     state_10, state_11, state_12, state_9a, state_12a);
  type tstate_type is (tstate_0, tstate_1, tstate_2, tstate_3);

  signal state, next_state      : state_type;
  signal tstate, next_tstate    : tstate_type;
  signal pad_indata, pad_outdata : std_logic_vector(7 downto 0);
  signal comm_reg               : std_logic_vector(7 downto 0);
  signal write_enable           : std_logic;
  signal fsm_en                 : std_logic;
  signal clk                    : std_logic;
  signal delay_reg              : unsigned(15 downto 0);
  signal trigger_reg            : unsigned(15 downto 0);
  signal trigger_counter        : unsigned(15 downto 0);
  signal fhet_sync              : std_logic;
  signal fhet_last              : std_logic;
  signal fhet_rising            : std_logic;
  signal ccd_trigger_sig        : std_logic;
  signal counter_en             : std_logic;

  component bidir
    port( pad      : inout std_logic_vector(7 downto 0);
          a        : in    std_logic_vector(7 downto 0);
          enable   : in    std_logic;
          y        : out   std_logic_vector(7 downto 0));
  end component;

  component clockdivider
    port(clkin : in  std_logic;
          reset : in  std_logic;
          clkout : out std_logic);
  end component;

begin

  epp_user2 <= '0';
  epp_user3 <= '0';
  epp_intr  <= '0';
```

```

bidir_1 : bidir
port map(pad => epp_data,a => pad_outdata,y => pad_indata,enable => write_enable);

div4 : clockdivider
port map (
    clkkin => clk_40m,
    reset => epp_init,
    clkout => clk);

process(clk, next_state, epp_init) -- epp state machine: next state flip-flops
begin
    if (epp_init = '0') then
        state <= state_0;
    elsif (RISING_EDGE(clk)) then
        state <= next_state;
    end if;
end process;

process(clk,next_tstate,epp_init)--trigger state machine: next state flip-flops
begin
    if (epp_init = '0') then
        tstate <= tstate_0;
    elsif (RISING_EDGE(clk)) then
        tstate <= next_tstate;
    end if;
end process;

-- epp state machine: next state logic
process (state, epp_write, epp_data_strobe, epp_addr_strobe)
begin

-- pc writes data to fpga cycle
    if (state = state_0 and epp_data_strobe = '0' and epp_write = '0') then
        next_state <= state_1;
    elsif (state = state_1 and epp_data_strobe = '0' and epp_write = '0') then
        next_state <= state_2;
    elsif (state = state_2 and epp_data_strobe = '0' and epp_write = '0') then
        next_state <= state_3;
    elsif (state = state_3 and epp_data_strobe = '0' and epp_write = '0') then
        next_state <= state_3;
    elsif (state = state_3 and epp_data_strobe = '1') then
        next_state <= state_0;

-- pc writes command to fpga cycle
    elsif (state = state_0 and epp_addr_strobe = '0' and epp_write = '0') then
        next_state <= state_4;
    elsif (state = state_4 and epp_addr_strobe = '0' and epp_write = '0') then
        next_state <= state_5;
    elsif (state = state_5 and epp_addr_strobe = '0' and epp_write = '0') then
        next_state <= state_6;
    elsif (state = state_6 and epp_addr_strobe = '0' and epp_write = '0') then
        next_state <= state_6;
    elsif (state = state_6 and epp_addr_strobe = '1') then
        next_state <= state_0;

-- pc reads data from fpga cycle

```

Appendix C. Code Developed for the FPGA

```
    elsif (state = state_0 and epp_data_strobe = '0' and epp_write = '1') then
        next_state <= state_7;
    elsif (state = state_7 and epp_data_strobe = '0' and epp_write = '1') then
        next_state <= state_8;
    elsif (state = state_8 and epp_data_strobe = '0' and epp_write = '1') then
        next_state <= state_9;
    elsif (state = state_9 and epp_data_strobe = '0' and epp_write = '1') then
        next_state <= state_9;
    elsif (state = state_9 and epp_data_strobe = '1') then
        next_state <= state_9a;
    elsif (state = state_9a) then
        next_state <= state_0;

-- pc reads command from fpga cycle
    elsif (state = state_0 and epp_addr_strobe = '0' and epp_write = '1') then
        next_state <= state_10;
    elsif (state = state_10 and epp_addr_strobe = '0' and epp_write = '1') then
        next_state <= state_11;
    elsif (state = state_11 and epp_addr_strobe = '0' and epp_write = '1') then
        next_state <= state_12;
    elsif (state = state_12 and epp_addr_strobe = '0' and epp_write = '1') then
        next_state <= state_12;
    elsif (state = state_12 and epp_addr_strobe = '1') then
        next_state <= state_12a;
    elsif (state = state_12a) then
        next_state <= state_0;
    else
        next_state <= state_0;
    end if;
end process;

-- trigger state machine: next state logic
process(state,tstate,fhet_rising,delay_reg,trigger_counter,comm_reg,pad_indata)
begin
if(tstate=tstate_0 and state=state_1 and comm_reg=X"10" and pad_indata(0)='1')then
    next_tstate <= tstate_1;
elsif (tstate = tstate_1 and fhet_rising = '0') then
    next_tstate <= tstate_1;
elsif (tstate = tstate_1 and fhet_rising = '1') then
    next_tstate <= tstate_2;
elsif(tstate=tstate_2 and delay_reg(15 downto 0)/= conv_unsigned(0, 16)) then
    next_tstate <= tstate_2;
elsif(tstate=tstate_2 and delay_reg(15 downto 0) = conv_unsigned(0, 16)) then
    next_tstate <= tstate_3;
elsif(tstate=tstate_3 and trigger_counter(15 downto 0)/=conv_unsigned(0, 16))then
    next_tstate <= tstate_3;
elsif (tstate=tstate_3 and trigger_counter(15 downto 0)=conv_unsigned(0, 16))then
    next_tstate <= tstate_0;
else
    next_tstate <= tstate_0;
end if;
end process;

process (clk, state)
begin
    if (RISING_EDGE(clk)) then
        -- copy incoming command
```

```

        if (state = state_4) then
            comm_reg(7 downto 0) <= pad_indata(7 downto 0);
        end if;
    end if;
end process;

inst_delay_reg : process (clk, state, comm_reg, tstate) -- delay register
begin
    if (RISING_EDGE(clk)) then
        if (state = state_1 and comm_reg = x"00") then
            delay_reg(7 downto 0) <= unsigned(pad_indata(7 downto 0));
            delay_reg(15 downto 8) <= delay_reg(15 downto 8);
        elsif (state = state_1 and comm_reg = x"01") then
            delay_reg(7 downto 0) <= delay_reg(7 downto 0);
            delay_reg(15 downto 8) <= unsigned(pad_indata(7 downto 0));
        elsif (tstate = tstate_2) then
            delay_reg <= delay_reg-1;
        end if;
    end if;
end process;

inst_trigger_reg : process (clk, state, comm_reg) -- trigger register
begin
    if (RISING_EDGE(clk)) then
        if (state = state_1 and comm_reg = x"02") then
            trigger_reg(7 downto 0) <= unsigned(pad_indata(7 downto 0));
            trigger_reg(15 downto 8) <= trigger_reg(15 downto 8);
        elsif (state = state_1 and comm_reg = x"03") then
            trigger_reg(7 downto 0) <= trigger_reg(7 downto 0);
            trigger_reg(15 downto 8) <= unsigned(pad_indata(7 downto 0));
        end if;
    end if;
end process;

inst_trigger_counter : process (clk, tstate) -- trigger counter
begin
    if (RISING_EDGE(clk)) then
        if (tstate = tstate_1) then
            trigger_counter <= trigger_reg;
        elsif (tstate = tstate_3) then
            trigger_counter <= trigger_counter-1;
        end if;
    end if;
end process;

process (clk, state) -- generate tristate control
begin
    if (RISING_EDGE(clk)) then
        if (state = state_7 or state = state_8 or state = state_9
            or state = state_10 or state = state_11 or state = state_12) then
            fsm_en <= '1';
        else
            fsm_en <= '0';
        end if;
    end if;
end process;

```

```

process (clk, state) -- generate epp_wait signal
begin
  if (RISING_EDGE(clk)) then
    if (state = state_2 or state = state_3 or
        state = state_5 or state = state_6 or
        state = state_8 or state = state_9 or state = state_9a or
        state = state_11 or state = state_12 or state = state_12a) then
      epp_wait <= '1';
    else
      epp_wait <= '0';
    end if;
  end if;
end process;

process (delay_reg, trigger_reg, comm_reg) -- put data on data bus
begin
  case comm_reg is
    when x"00" =>
      pad_outdata(7 downto 0) <= std_logic_vector(delay_reg(7 downto 0));
    when x"01" =>
      pad_outdata(7 downto 0) <= std_logic_vector(delay_reg(15 downto 8));
    when x"02" =>
      pad_outdata(7 downto 0) <= std_logic_vector(trigger_reg(7 downto 0));
    when x"03" =>
      pad_outdata(7 downto 0) <= std_logic_vector(trigger_reg(15 downto 8));
    when others =>
      pad_outdata(7 downto 0) <= (others => 'X');
  end case;
end process;

process (fsm_en, epp_write)
begin
  if (fsm_en = '1' and epp_write = '1') then
    write_enable <= '1';
  else write_enable <= '0';
  end if;
end process;

epp_write_enable <= write_enable;

process (clk, fhet) -- synchronize fhet
begin
  if (RISING_EDGE(clk)) then
    fhet_sync <= fhet;
  end if;
end process;

process (clk, fhet_sync) -- previous fhet
begin
  if (RISING_EDGE(clk)) then
    fhet_last <= fhet_sync;
  end if;
end process;

process (clk, fhet_sync, fhet_last) -- detect fhet rising edge
begin
  if (RISING_EDGE(clk)) then

```



```

        fhet_rising <= fhet_sync and (not fhet_last);
    end if;
end process;

inst_ccd_trigger : process (clk, tstate) -- ccd_trigger
begin
    if (RISING_EDGE(clk)) then
        if (tstate = tstate_3) then
            ccd_trigger_sig <= '1';
        else
            ccd_trigger_sig <= '0';
        end if;
    end if;
end process;

ccd_trigger <= ccd_trigger_sig;

process (tstate)
begin
    if (tstate = tstate_0) then
        epp_user1 <= '0';
    else
        epp_user1 <= '1';
    end if;
end process;

end behavioral;

```


Bibliography

- [1] Karsten Danzmann and the LISA Study Team. LISA-An ESA cornerstone mission for the detection and observation of gravitational waves. *Adv. Space Res.*, 32(7):1233–1242, 2003.
- [2] Andrzej Królak *et al.* The LISA Sensitivity. *7th Gravitational Wave Data Analysis Workshop, Kyoto, Japan*, December 2002.
- [3] Gerhard Heinzel *et al.* Interferometry for the LISA technology package (LTP) aboard SMART-2. *Classical and Quantum Gravity*, 20, April 2003.
- [4] Gerhard Heinzel. *Advanced optical techniques for laser-interferometric gravitational-wave detectors*. PhD thesis, Max Planck Institute for Quantum Optics and University of Hanover, February, 1999. MPQ Report 243.
- [5] Anthony E. Siegman. *Lasers*. University Science Books, 1986.
- [6] Vinzenz Wand. Interferometrie und Phasenauslesung für die wissenschaftliche Weltraummission SMART2. Diploma thesis (in German), University of Hanover, 2003.
- [7] David Robertson *et al.* LTP Interferometer-Noise Sources and Performance. In *5th International LISA Symposium*, July 2004. To appear in *Classical and Quantum Gravity*. submitted.
- [8] Yves Sirel. Fringe Analysis. *P.K. Rastogi (Ed.):Photomechanics, Topics App. Phys. 77,55-102*, 2000.
- [9] Klaus Freischlad and Chris L. Koliopoulos. Fourier description of digital phase-measuring interferometry. *J. Opt. Soc. Am. A. 7,542-551*, 1990.
- [10] Dave Litwiller. CCD vs. CMOS: Facts and Fiction. *Photonics Spectra*, January 2001.
- [11] Wojciech Dulinski. Monolithic CMOS Pixel Sensors for High Resolution Particle Particle Tracking. Brookhaven National Laboratory, April 2003.
- [12] Paul Horowitz and Winfield Hill. *The Art of Electronics*. Cambridge University Press, 2nd edition, 1989.
- [13] Datasheet OP27. Low-noise high-speed precision operational-amplifier. Datasheet, Texas Instruments, Revised September 2000.
- [14] Gerhard Heinzel *et al.* The LTP interferometer and phasemeter. *Classical and Quantum Gravity*, 21, February 2004.

- [15] Gerhard Heinzel. Resonant Sideband Extraction-Neuartige Interferometrie für Gravitationswellendetektoren. Diploma thesis (in German), University of Hanover, November 1995.
- [16] Amnon Yariv. *Quantum Electronics*. John Wiley & Sons, 2nd edition, 1975.
- [17] Peter R. Saulson. *Fundamentals of Interferometric Gravitational Wave Detectors*. World Scientific Publishing, 1994.
- [18] Frank Steier. Methoden zur thermo-optischen Charakterisierung optischer Komponenten. Diploma thesis (in German), University of Hanover, May 2004.
- [19] Jun Mizuno. *Comparison of optical configurations for laser-interferometric gravitational-wave detectors*. PhD thesis, Max Planck Institute for Quantum Optics and University of Hanover, July 1995. MPQ Report 203.

Acknowledgment

I would like to thank Prof. Dr. Karsten Danzmann for his support and giving me the opportunity to conduct this thesis in his incredible working group.

To all the people at the AEI Hanover for creating such a pleasant working and social atmosphere.

To Dr. Gerhard Heinzl, I would like to express my special thanks for his excellent support and guidance. All the results achieved in this thesis are product of this unique collaboration, which gave me the opportunity to learn a lot from him in many different fields.

For the amazing experience in the LISA Group, I would like to thank Antonio Garía Marín, Vinzenz Wand, Frank Steier, Johanna Bogenstahl, and Sascha Skorupka. Thanks for the unconditional and fantastic support. It is great to work with you!

To Dr. Oliver Jennrich for the motivating discussions and his useful contributions to the results achieved by this thesis. The time in the laboratory was always very productive.

For taking always a couple of minutes to check diverse software and programming problems, I would like to thank Gerrit Kühn for his unconditional cooperation.

My gratitude To Dr. Gerhard Heinzl, Antonio García, James DiGuglielmo, Dr. Siong Heng, and Frank Steier for reading and improving various parts of this manuscript. Naturally, all remaining errors are my own responsibility.

To my dear girlfriend Zlatka for her patience, comprehension and continuous support: muchas gracias mi amor.

I want to dedicate this thesis to my parents. Ustedes han sido siempre mi motivación para continuar.

Verwendete Hilfsmittel

Zusätzlich zu den in der Arbeit erwähnten Hilfsmitteln, wurden die folgenden Werkzeuge bei der Erstellung dieser Arbeit benutzt.

Berechneten Funktionen und Messdaten wurden mit Gnuplot gezeichnet.

Diagramme sind mit Xfig und Eagle hergestellt. Für die Datenauswertung wurde selbstgeschriebenen C-Programmen verwendet und mit dem Gnu C Compiler kompiliert.

Diese Arbeit wurde mit pdfTeX (Web2C 7.4.5) verfasst.

Selbstständigkeitserklärung

Hiermit versichere ich, dass ich diese Arbeit selbständig verfasst und keine anderen als die angegebenen Hilfsmittel und Quellen benutzt habe.

(Felipe Guzmán Cervantes)